A Light Direction Sensor for Integrated 3D Vision

Robin Buijs

16 January, 2015

CONFIDENTIAL
until 16 January 2016

Abstract

Light field sensors based on three-dimensionally structured pixels were designed, realised and characterised. These micrometre-scale sensors are predicted to be able to fully quantify the two-dimensional direction and intensity of the local light field, equivalent to the electromagnetic Poynting vector. Anisotropic etching is successfully employed to produce the desired three-dimensional structures on silicon-on-insulator wafers. Pixels show an angular sensitivity of around 7% of the theoretical prediction, with unexpected response in non-sensitive directions. Further improvements in the fabrication process are suggested that are predicted to improve sensitivity by orders of magnitude.

About this work

The work described in this document is part of the Dutch NWO/STW VENI project "Controlled three-dimensional self-assembly of silicon nanoparticles using hydrogen bonds" led by Dr. Léon A. Woldering. It is embedded within the Transducers Science & Technology group within the MESA+ Institute for Nanotechnology of the University of Twente, led by Prof. Dr. Gijs J.M. Krijnen. The work was performed in partial fulfilment of the MSc programmes in Applied Physics and Electrical Engineering at the University of Twente, and jointly supervised Prof. Krijnen and Prof. Dr. Willem L. Vos of the Complex Photonic Systems chair, also part of the MESA+ Institute. Independent supervision was done by Prof. Dr. J. Schmitz of the Semiconductor Components group in the same institute.

This work builds on years of experience within the TST group, as well as valuable input from the COPS group and several others. All four supervisors have contributed a wealth of expertise. Several members of the TST group have provided help in topics ranging from measurement engineering to wirebonding. The COPS group members have contributed in regular discussions and spectrometry. The MESA+ Cleanroom staff have played a large role in fabrication process engineering and optimisation. Prof. Dr. J.J.W. Van der Vegt of the Numerical Analysis & Computational Mechanics group has provided advice on Green's function theory.

I owe my thanks to all these people for having provided me the opportunity to do high-level science and engineering in a highly professional and ambitious environment. In addition, I thank my direct colleagues in the TST and COPS groups for a social environment that helps make science even more enjoyable.

STW is gratefully acknowledged for funding.

Transducers Science & Technology group
MESA+ Institute for Nanotechnology
University of Twente
P.O. Box 217 , 7500 AE
Enschede , the Netherlands

Complex Photonic Systems chair
MESA+ Institute for Nanotechnology
University of Twente
P.O. Box 217 , 7500 AE
Enschede , the Netherlands

Contents

Chapter 1

Introduction

Visual depictions of reality form a staple of human culture. In modern times, photography and video have found major roles in communication, from personal interaction to scientific research.

Most cameras are built according to one particular layout. A set of optics, also referred to as the objective, maps the incoming light rays to a sensor plane. There the spatial intensity distribution is recorded, either photochemically or in discrete electronic pixels. The optical system directs light coming from a point on the subject plane to a single point at the sensor. Points farther away from this plane are increasingly blurred.

The rate of blurring with distance is inversely measured by the depth of field. The depth of field increases with smaller apertures, but this also limits the amount of light reaching the sensor. Taking a photograph thus requires compromising on what parts of the scene will be imaged well.

In addition to the basic optics-sensor system, a complete camera features several components to help in the creative process. A simplified schematic of the sophisticated single lens reflex camera is shown in figure 1.1. Here, a set of movable mirrors is used for user feedback and possibly to direct some light to a separate sensor for an auto-focusing system. The detector housing contains additional optics to introduce colour vision and refocus for optimal detection. [1]

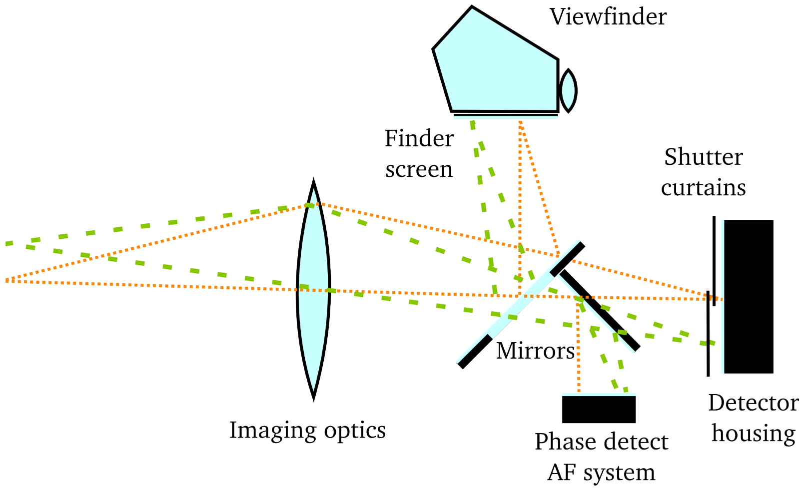

Figure 1.1: Schematic internal layout of a modern digital single lens reflex camera with phase-detect autofocus. The user looks at an image projected onto the finder screen, while some light is directed into the phase-detect autofocus sensor. When taking a photograph, the mirrors and shutter move aside. The image is then projected onto the sensor, which records the light intensity at each sensor element, or pixel. Not shown are filters for unwanted wavelengths and additional optics directly on the sensor, including colour filters and microlenses. Image based on [1]

Interestingly, conventional cameras record only a fraction of the information in the light incident upon their sensors. Each pixel integrates the light it receives to a local light intensity. The light direction distribution is irretrievably lost. How this affects photography is better understood in terms of the light field.

1.1 The light field

In the limit of geometrical optics, light may be taken to travel in rays.[34] A ray originates from a light source and travels along a fixed direction until encountering an obstacle, where secondary rays may originate. Each such ray is fully described by a position along its length x, y, z, its directions θ, ϕ and its radiance L. We can express radiance as a function of the other variables. This is the full five-dimensional light field $L(x, y, z, \theta, \phi)$.[1] [2]

A camera sensor pixel has a fixed position in space. The information such a pixel can conceivably extract from the light field is then the light intensity in each possible direction, or $L_{x,y,z}(\theta, \phi)$. Ordinary camera pixels integrate this function over all angles to find a single radiance for each pixel, $L_{\text{eff}} = \iint L(\theta, \phi)\, d\theta d\phi$.

Finding the complete reciprocal space spectrum of the light source is conceptually interesting, as it allows full lensless imaging through Fourier analysis. However, this would require the recording of a huge amount of information per pixel. A simpler approach is to define a single overall, effective light direction for each pixel.

We can express the radiance with its effective direction either in three variables, or in a single vector $\mathbf{L}_{x,y,z}$. This vector describes the net energy flux through some point in space and is identical to the Poynting vector in electromagnetism.[10] If, as per usual, there is a well-defined sensor plane ($z = 0$), we can combine the information in the individual pixels into the effective light field at the sensor $\mathbf{L}(x, y)$.

The power of this approach is visible in figure 1.2. We consider a pixel that can resolve radiance and light direction. Two objects are positioned along the same line through the centre of the optical system and as such in principle mapped to the same pixel - although of course at least one is out-of-focus.

For the out-of-focus light source, only a specific subset of reciprocal space vectors arrives at the sensor: in case of fore-focus, the most oblique rays miss the pixel, while in case of rear-focus the least oblique ones miss. The effective light direction thus varies smoothly and monotonously with distance to the light source. This means that the light direction sensor directly measures distance to the light source.

The implications for photography are enormous. Knowledge of the third dimension allows manipulation of both focal length and depth of focus. The direct recording of depth information enables the reconstruction of the three-dimensional scene in any desirable format in a single sensor.

1.2 Light direction sensing

A device capable of exploiting these properties of the light field is called a light field, or plenoptic, camera. The principle by which commercially available light field cameras operate was proposed in the early 20th century. [3] It is illustrated in figure 1.3.

The camera may use an ordinary light intensity sensor array, but between it and the objective, a microlens array is placed so that each microlens covers a number of pixels. The light incident on the microlens is refocused and passes on to the sensor. The local intensity pattern on the sensor is a measure for the focal error, so that 3D-information on the scene can be retrieved for the region corresponding to each microlens. For large focal error the pattern tends to uniformity, so that in practice, multiple microlenses with different focal lengths may be used to obtain a good resolvable depth range. [4]

---

[1] In empty space, one of the dimensions is redundant, because the entire field can be reconstructed from a single four-dimensional slice. Many authors use the phrase 'four-dimensional light field' for this reason.

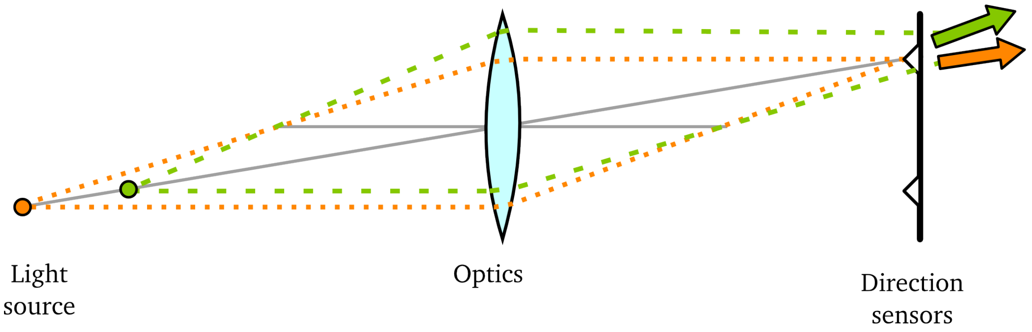

Figure 1.2: Two light sources, positioned such that they are mapped to the same pixel, give different readings on the direction sensor. Since the effective direction of the light field on the pixel is a smooth, monotonous function of focal error, the distance to the light source is measured directly.

This technique has an obvious drawback in that spatial resolution is limited to one effective pixel per microlens. The two major commercial camera manufacturers report a minimum resolution loss of a factor of 4 and 10 compared to the native resolution of the sensor. [4][5] A low number of pixels per microlens however limits the range of focal error that can be resolved. Note also that this technique can only resolve the focal error of the incident light; it does not actually detect light direction, limiting its possible uses.

Several means of detecting light direction have been proposed. One example with classical roots is shown in figure 1.4. Here, use is made of the fact that the radiant flux through a surface depends on its angle with the incoming radiation. If two surfaces under different angles are compared, radiance and one dimension of incoming light direction can be resolved. Another surface under a yet different angle fixes the second direction.

This principle is used on the microscale in phase-type autofocus systems. Here, photodiodes are mechanically mounted under alternating angles. Each angle looks towards one aperture. If the image is in focus, light through each aperture will reach the centre of the sensor. If it is out-of-focus, the two beams will move apart. The direction sensors can tell which beam is on which side and thus both the sign and magnitude of focal error. This technique is however limited to applications where the relatively high price per pixel is not an issue, because the requirement of mounting separate diodes makes for a complicated assembly process. [1]

Another example with a long history is the sundial, where the position of the shadow of an

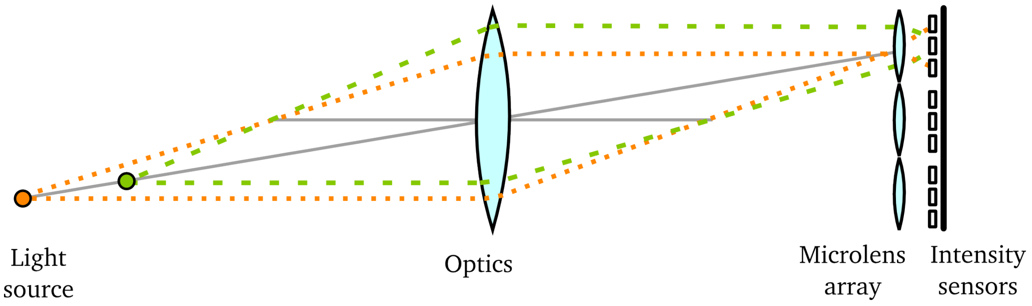

Figure 1.3: The internal layout generally used for light field cameras. A microlens array refocuses the light incident upon a group of pixels. The resulting intensity distribution after the microlens peaks strongly on the axis of the microlens if the sensor is now in focus; otherwise, a different distribution is seen. The pixels thus measure the focal error after the microlens, from which the subject distance may be found.

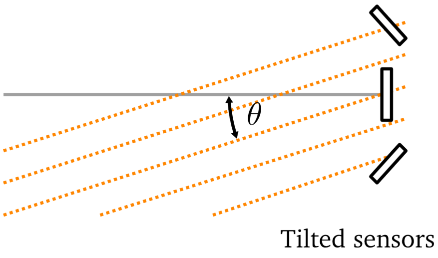

Figure 1.4: Tilting a sensor with respect to the local radiance vector will change the radiant flux it perceives. This effect can be used to find light direction from two sensors under different angles. In this image, the middle sensor receives less light than it would at normal incidence, and the lower sensor receives less yet. The upper sensor, however, receives more light than at normal incidence, because from its perspective the light is moving towards normal.

object measures the incoming light direction. Microscale variations have been proposed, but suffer either from very low resolution or lack of radiance sensitivity despite a complex fabrication process. [6] [7]

A more advanced recent proposal uses the Talbot effect of near-field diffraction to obtain a light direction dependent light intensity in the sensing region behind a pair of gratings. Combining the information of several of these sensors allows one to resolve the full radiance vector. Its prime disadvantage is the need to combine several sensors, all of which need to be many wavelengths in dimension, leading to aliasing in the measured signal. In addition, no more than half the light ever reaches the sensing region. [8]

1.3 3D structured detector

In this work we investigate the possibility of integrating multiple light-sensitive surfaces under different angles on the same microstructure. Such a structured detector would have all the advantages of the tilted sensor-approach, but not the drawback of complicated assembly.

We investigate two types of structures, indicated in figure 1.5. In the pit-based detector the tilted surfaces are the sloping regions of a depression in the detector surface. The tetrahedron-based detector uses a monolithic protrusion from the surface, where each surface is a separate sensing plane.

We will first discuss the conceptual elements required to design such detectors. With the qualitative designs in mind, we shall endeavour to find a theoretical model of detector properties. We will briefly discuss the work done to verify the feasibility of the designs given the available materials. The fabrication process of the detectors will be developed and discussed before moving on to experimental methods. Finally, the light direction sensing results will be discussed.

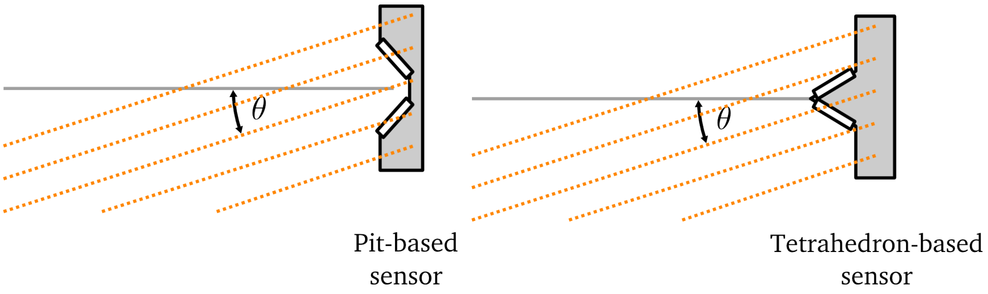

(a) (b)

Figure 1.5: The concept of detector surface structuring can be used to design light field sensors with photosensitive surfaces on the slopes of a pit, as in (a), or on the slopes of a protrusion like the tetrahedron in (b).

Chapter 2

Detector design

From the principle of three-dimensional detector structuring a qualitative design for a detector can be made. Three further technological feats are required to define a detector outline in appreciable detail.

We will discuss the technique of anisotropic etching, with which three-dimensionally structured surfaces can be produced, the different methods of light detection in semiconductors and the theory of metal-semiconductor contacting, before moving on to the detector designs.

2.1 Anisotropic etching

The different planes in a crystal, when exposed to the environment, will undergo different reconstructions to fix the dangling bonds. Each such reconstruction is chemically distinct. For this reason, certain chemicals show very different etch rates on different surface planes. This can be exploited for a process known as anisotropic etching.[9]

Silicon natively forms an FCC diamond lattice with a two-atomic basis. The <100> plane is most commonly used as substrate surface. Tetramethyl ammonium hydroxide (TMAH) is one of several etchants that etch the <100> plane selectively with respect to the <111> plane. The selectivity of <100> over silicon dioxide and silicon nitrides is higher still, meaning these can be used as masks.[9] The result is that a square window in an oxide layer on <100> silicon, oriented along the <100> direction, can be etched down to an inverted square pyramid. On wafers with a buried oxide, known as SoI wafers, larger pits may be capped of by the oxide.

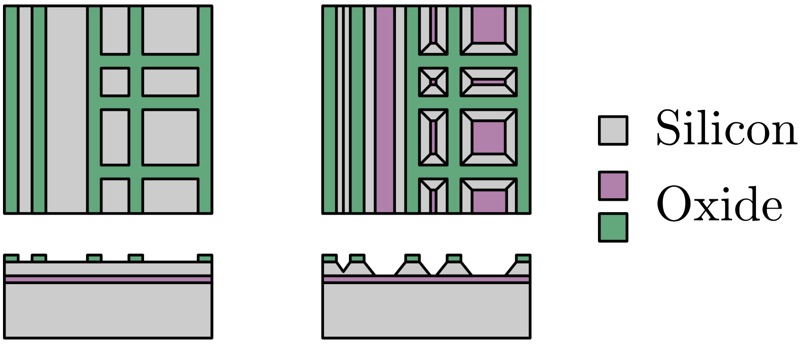

Figure 2.1: Anisotropic etching using TMAH or other etchants can be used to fabricate a range of rectangular pits with sloping sidewalls. Here, a SoI wafer with <100> device layer is masked by a patterned oxide. When this wafer is etched down with TMAH, the pits will retain reliably sloped sidewalls.

The process is to a large degree self-limiting. After all the available <100> silicon has been etched down, leaving only <111> faces exposed, etching of these planes still goes very slowly. This technique can thus be used to create a range of three-dimensional surface structures with a relatively simple, robust process. This is illustrated in figure 2.1.

The angles involved can be found directly from the symmetry of the diamond lattice. The eight planes with Miller indices $(\pm 1, \pm 1, \pm 1)$ are identical by symmetry. Planes differing by two signs form part of the same regular tetrahedron. The geometry of a tetrahedron is shown in figures 2.2 and 2.3. It can be seen that the angle between a plane and an edge, which is the angle between the <100> and <111> planes, is $\theta = 54.74°$.

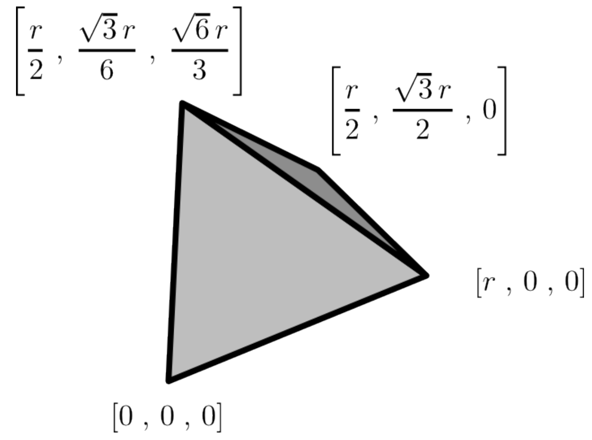

Figure 2.2: The locations of the vertices of a tetrahedron in a straightforward coordinate system.

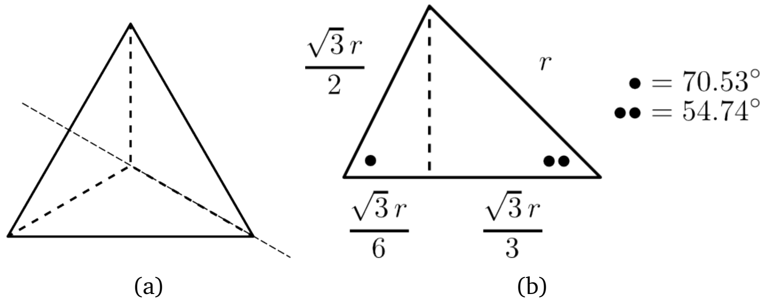

Figure 2.3: (a) top view of a tetrahedron. (b) cross-section of a tetrahedron along the line drawn in (a). Note that the faces make an angle of $\theta = 70.53°$ with one another. The angle of $\theta = 54.74°$ is between an edge and the plane at either end.

On SoI wafers, the etch can also be used to make electrical islands in the device layer. However, corners of the silicon pointing outwards do not simply etch down to the <111> plane. This can be seen in figure 2.4. Without going into detail we note that this etch rate is about three times as large as the <100> rate, so that any outer corners will need significant leeway to not be destroyed during etching.

2.2 Light detection

Two mechanisms are fit for light detection in semiconductor devices: the photovoltaic and the photoconductive effect. Both revolve around electron-hole pair generation.

Figure 2.4: An anisotropically etched channel in silicon making a straight corner. The outer corner of the remaining silicon is visibly etched more quickly than the rest of the structure.

Semiconductors are materials with electronic states both somewhat above and somewhat below the Fermi energy, but none close to it. As empty states are required for conduction, the only carriers that contribute to conduction are those excited over this gap, known as the bandgap, by thermal effects or other energy in the system. In addition, the introduction of impurities known as dopants can introduce extra electrons to the higher-energy band, or remove them from the lower-energy band, leaving electron holes.

Absorption of incident light in a semiconductor will generally cause some combination of heating and excitation of electrons, leaving an electron-hole pair. The balance between the two depends on photon energy.

The band gap of silicon is $E_g = 1.1\,\mathrm{eV}$[13]. This means that visible light has plenty of energy to overcome the band gap, and light more energetic than $\lambda = 564\,\mathrm{nm}$ has enough energy to excite two photons.

At one excitation per absorbed photon[1] we can calculate the excess carrier generation rate as a function of incident light intensity.

The difference between photovoltaic detection and photoconductive detection is in the way the carriers are separated.

A photodiode has a depletion layer where few free carriers remain in the face of a built-in voltage. Excess carriers generated here will naturally drift off, and given their opposite signs, drift off in opposed directions. These extra carriers will then contribute to building up an external potential difference. This is the photovoltaic effect.

In practice, the photodiode is shorted through a current meter. The current then directly measures the carrier generation rate.

The photoconductive method lacks the built-in voltage and thus needs to apply an external voltage to separate the generated carriers.

Semiconductor conductivity depends on carrier concentrations through

$$\sigma = e\,(\mu_e\, n + \mu_h\, p) \tag{2.1}$$

where e is the elementary charge, n and p are carrier densities and μ the corresponding mobilities.

These non-equilibrium carriers have a fixed lifetime τ, which together with the generation rate G leads to a fixed increase in their concentrations. They contribute to conductivity as any other in

---

[1] This is suggested to be the normal behaviour.[13]

equation 2.1, giving rise to a conductivity change

$$\Delta\sigma = e\,G\,(\mu_e\,\tau_e + \mu_h\,\tau_h) \tag{2.2}$$

At a fixed external voltage, the current measures the generation rate here too.

Although photovoltaic detection is industry standard and more interesting for commercial devices, photoconductive detection makes for an easier fabrication process, negating the need for active doping, and preserves the symmetry of the system.

In addition, given the close relation between the two, it is entirely to be expected that insight gained from photoconductively operated devices is directly applicable to photovoltaically operated devices.

We thus decide to use the photoconductive effect as the mode of operation of the detectors under design.

2.3 Metal-semiconductor contacts

Metal-semiconductor junctions can behave as either Schottky diodes or Ohmic contacts depending on the specific materials properties.[13]

	$\phi_m < \phi_s$	$\phi_m > \phi_s$
n	Ω	D
i	Ω?	Ω?
p	D	Ω

A basic theoretical description can be phrased in terms of work functions and doping. On contact, electrons will flow from the semiconductor's conduction band into the metal, while the metal's electrons will fill up the electron holes in the semiconductor's valence band. If the numbers of these charge carriers are not in balance due to doping, a space charge will develop around the interface to prevent further depletion. The band structure will curve to reflect the inhospitality to one type of charge carrier, with a barrier height determined by the difference in work functions. If majority carrier depletion would occur in the semiconductor, a barrier is formed. Carrier depletion in the metal does not significantly alter the net concentration or conductivity, leaving an Ohmic contact.

The same statement can be phrased in terms of band diagrams. The difference in work functions represents a difference in Fermi energies before contact. When contact is made, the bulk band levels shift with the Fermi level, but near the interface they retain their old value to accommodate the space charge. If this curvature provides a barrier for the majority carrier in the semiconductor, no current will flow from the semiconductor into the metal.

The theory suggests that contacts with intrinsic semiconductors would be Ohmic no matter what, because only one type of carrier can be obstructed at the same time. However, very light doping - including interface effects - could already make the junction rectifying. Tables of work functions by metal and electron affinity χ plus band gap E_{G} by semiconductor are known from literature.[13] For silicon, the work function can be calculated to be $\phi = 4.61 + d\phi$ eV, with $d\phi$ a small correction for the shift in Fermi level due to doping.

Considering experimental artefacts, the best metals would be those with a large safe margin $\Delta\phi$ in the work function. For n-doped silicon, the best common metals for contacting would be thorium ($\Delta\phi < 1.0\,\mathrm{eV}$), aluminium ($\Delta\phi < 0.5\,\mathrm{eV}$) and copper ($\Delta\phi < 0.3\,\mathrm{eV}$). For p-doped silicon, the best options would be platinum ($\Delta\phi < 1.5\,\mathrm{eV}$), gold ($\Delta\phi < 0.2\,\mathrm{eV}$) and silver ($\Delta\phi < 0.1\,\mathrm{eV}$).

In real systems, junction behaviour is very different. Highly doped contacts are Ohmic no matter what, because the small depletion length is easily traversed by tunnelling with disregard for junction details.

In addition, interface effects tend to near-completely drown out the above theory.[23] This is theorised to be caused by electronic gap states caused by the dopants. Contacts are also very much affected by local doping from the contact material.

One additional consideration is that highly reactive[2] metals, such as aluminium, will chemically react with a native oxide, improving adhesion and leading to a much better contact. As such,

---

[2] In effect, having low electronegativity; being a good chemical reducer.

Table 2.1: The bandgap E_G and electron affinity χ of selected semiconductors, and the work function ϕ of selected metals. Data reproduced from [13]

	E_G (eV)	χ (eV)
GaAs	1.43	4.07
AlAs	2.16	2.62
GaP	2.21	4.30
InAs	0.36	4.90
InP	1.35	4.35
Si	1.12	4.05
Ge	0.66	4.00

	ϕ (eV)		ϕ (eV)
Al	4.1	Fe	4.6
Cs	1.9	Pt	6.3
C	4.8	Ag	4.7
Cu	4.3	Th	3.5
Au	4.8	W	4.5

aluminium is claimed to make acceptable contacts on both n- and p-doped silicon.[24][25] In its pure form, aluminium is known to disturb the silicon lattice and form spikes into it, possibly leading to a device failure mode known as as junction spiking. To counter this, 1% silicon is sputtered along with the aluminium. Expert advice from MESA+ cleanroom staff supports this technique for aluminium-silicon contacts without any annealing steps.

Commercially, heavy use is made of contact layers to improve contact. This normally has the obvious drawback of introducing extra process steps.

Considering the difficulties in contacting semiconductor material with metal directly, it may be more practical to construct the leads to the detector from highly doped semiconductor. When both materials have the same majority carrier this should produce very nice contacts. The problem of metal-semiconductor contacting is then moved to a point further from the detector, where space is not an issue - allowing for larger contact area - and very high doping can be employed to make good contact with any type of metal.

One possible fabrication method involves depositing polycrystalline silicon on the whole wafer and implanting abundant dopants at a certain depth. The excess poly-silicon can the be etched away with a Wright etch.

A perk of this method is that the poly-silicon can also act as a getter for impurities in the detector material. One drawback is that the Wright etch is rather toxic.

For an initial design, silicon-infused aluminium appears the best choice.

2.4 Pit-based detector

With the previously discussed considerations, we aim to design a photoconductive light direction sensor based on an anisotropically etched pit in <100> silicon.

The detector is to function by comparing the resistance changes due to light caught in the silicon behind different <111> surfaces. To minimise detector size, it makes sense to use the inside surfaces of a pit. A single square pit has two pairs of opposing faces and the radiant flux pattern directly measures the full $L_{x,y}$ vector.

If we consider one such a pit on a large, otherwise mirrored island, with contact leads to the corners of the pit, we have a detector, albeit not a very good one. This design is shown in figure 2.5. Already, a few tradeoffs have been made; the mirroring, for example, contains faults, to prevent shortage between the contacts.

We can model the pit-based sensor as a four-resistor ring as n figure 2.6. Each measurement between two contacts is affected by all resistance values, but most strongly by the resistor directly between the contacts.

For the large-island detector, we would expect small dark resistance values, because the whole island contributes to conduction. This means that the more or less fixed excess conduction paths introduced by the light are much less noticeable.

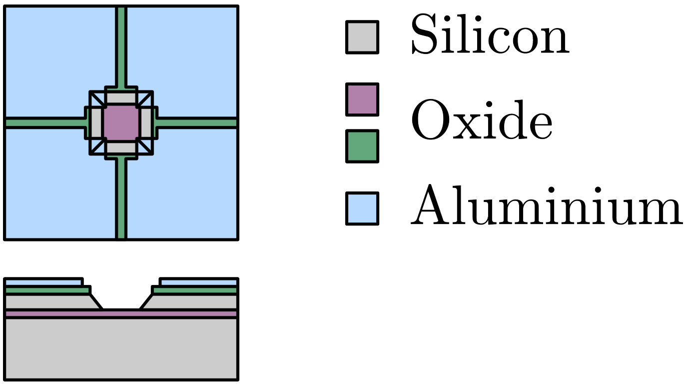

Figure 2.5: Schematic top view and cross-section of a very basic pit-based detector design. The central pit has four tilted surfaces that catch light. Light entering from other sides is precluded by the large aluminium mirrors. The resulting resistances are read out through the aluminium contacts in the corners of the pit.

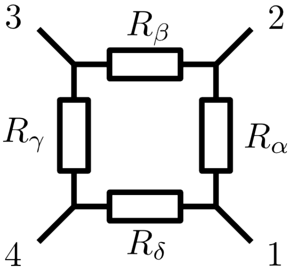

Figure 2.6: The four-resistor equivalent model of the pit-based detector. Contact resistances are not shown.

A more advanced general design is shown in figure 2.7. The resistors behind the light-sensitive surfaces are now of limited and well-defined dimension, so that the relative conductance change due to lighting is as large as possible.

Additionally separate current contacts have been added, so that four-point measurements may be used.

The mirroring is imperfect, but insulated overlapping mirrors would require a much more complicated design.

2.5 Tetrahedron-based detector

An anisotropic etching process to fabricate regular tetrahedra in the <111> device layer of a SoI wafer was designed in earlier work.[3] It leaves silicon tetrahedra regularly spaced on the buried oxide layer of a SoI wafer.

Contacting these tetrahedra is relatively straightforward, as seen in figure 2.8. Given the small desired dimensions of the system however there is no clear way to introduce separate sense contacts. This approach thus depends on the viability of two-point measurements.

The tetrahedron too can be represented as a resistor ring. As all considered effects are linear, there must be some way to express it as a linear electronic circuit. In the steady state, when only the base vertices are considered, a three-resistor model, as in figure 2.9, can describe all the

---

[3] Unpublished work of L.A. Woldering and J.W. Berenschot.

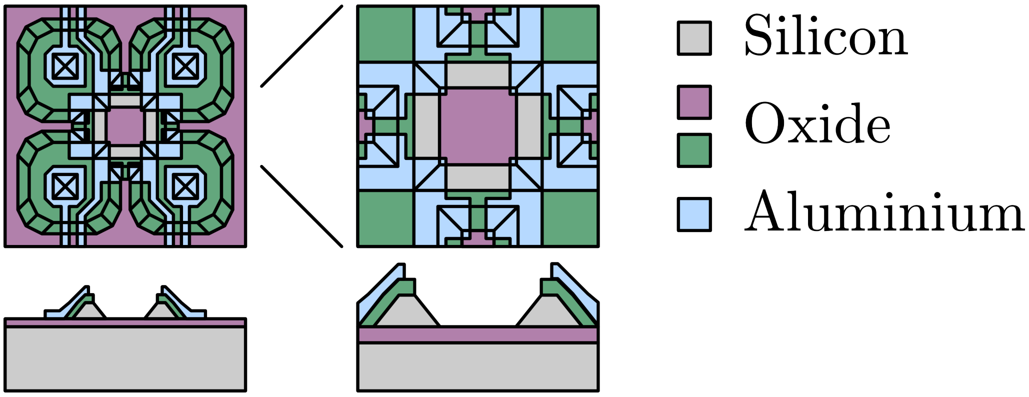

Figure 2.7: A more advanced pit-based detector. The measurement channels are narrower to maximise the relative effect of incident light. Separate source and sense contacts are implemented to allow characterisation of only the channel properties.

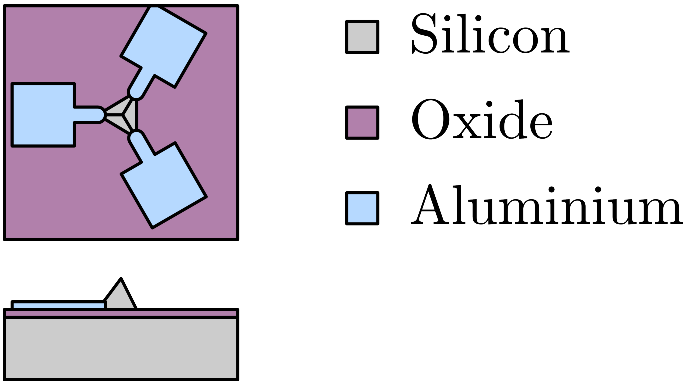

Figure 2.8: A basic contact layout for the tetrahedron-based detector. The tetrahedron fabrication process is documented elsewhere. Four-point contacting of the tetrahedron is likely to be infeasible due to the small size.

electronics involved.

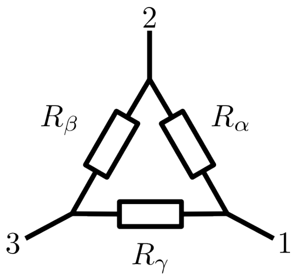

Figure 2.9: The three-resistor model of the tetrahedron-based detector. Contact resistances are not shown.

Chapter 3

Detector modelling

We aim to quantify the expected behaviour of the detectors designed in chapter 2 as a function of the remaining design parameters. The design can be fine-tuned based on such a model. The model can also help interpret measurement data.

One major theoretical challenge is the behaviour of excess carriers within the devices. When the conductivity profile is clear, we need a way to translate this to a resistance. Then, we would like to relate this resistance to the resistances we measure. The lessons learnt here will result in a set of requirements on the substrates to be acquired for device fabrication.

3.1 Excess carrier dynamics

As discussed in chapter 2, the photoconductive effect leads to a conductivity change of

$$\Delta\sigma = e\,G\,\left(\mu_{\mathrm{e}}\,\tau_{\mathrm{e}} + \mu_{\mathrm{h}}\,\tau_{\mathrm{h}}\right) \tag{3.1}$$

with e the elementary charge, G the carrier generation rate, μ electronic mobilities and τ excess carrier lifetimes.

The carrier generation rate is determined by the incident radiant flux and the quantum efficiency η of the photoelectric effect. This has been studied in detail by others.[14] For us it suffices to note that this value varies between $\eta = 0.5$ and $\eta = 0.8$, staying close to $\eta = 0.7$ for much of the visible spectrum.

In a wafer of any detectable doping, the majority carriers fully determine conductivity. The mobility for holes in a lightly doped p-type semiconductor near room temperature is [15]

$$\begin{aligned}\mu_{\mathrm{h}} &= \mu_{\mathrm{min}} + \frac{\mu_0}{1 + (N/N_{ref})^{\alpha}} \\ &= 4.612 \times 10^{-2}\,\frac{\mathrm{m}^2}{\mathrm{V\,s}}\end{aligned}$$

The lifetime of excess carriers is set by the availability of minority carriers to recombine with. Although the lifetime of majority carriers is much longer, because their chances of meeting a minority carrier are quite small, the excess concentration will decrease as quickly as the minority excess.

Effective minority carrier lifetime is mostly determined by the presence of crystal defects, including both dopant atoms and the crystal edge. Aside from this qualitative observation its value is hard to predict and hard to modify. [17]

For the bulk lifetime of silicon wafers, literature estimates range between $\tau = 10{-}1000\,\mu\mathrm{s}$.[19][16] A value of $\tau = 100\,\mu\mathrm{s}$ will be considered reasonable for this type of sample. However, in most systems steady-state concentrations are strongly affected by surface effects. For macroscale systems, an effective lifetime can be defined to describe the overall statistics of the carriers,

$$\frac{1}{\tau_{\mathrm{eff}}} = \frac{1}{\tau} + \frac{1}{\tau_{\mathrm{s}}}$$

Surface lifetime is determined by the diffusion current reaching the surface and the recombination rate on the surface, normally expressed in a recombination velocity S in $\frac{\mathrm{m}^3}{\mathrm{m}^2\,\mathrm{s}}$. On untreated silicon the recombination velocity is tiny. This limits effective lifetimes in wafers of thickness $l_\mathrm{w} = 300\,\mu\mathrm{m}$ to about $\tau = 2.5\,\mu\mathrm{s}$. However, surface lifetime can be vastly increased by passivation, for example through growth of a thermal oxide. Note that silicon will readily grow a native oxide, so that recombination velocity may decrease significantly without active processing.

The floating zone (FZ) crystal growth process is an alternative for the standard Czochralski (CZ) process. The FZ process leads to significantly lower impurity concentrations and is known to produce much higher bulk lifetimes and thus efficiencies in photovoltaic devices; practically obtainable efficiencies currently go up to about $\eta = 25\%$ for FZ-grown silicon versus $\eta = 20\%$ for CZ-growth. [17] [18]

3.1.1 One-dimensional systems

We will analyse the behaviour of excess carriers in one-dimensional resistors. Consider light of monochrome $\lambda = 500\,\mathrm{nm}$ at an intensity of $I = 1\,\frac{\mathrm{W}}{\mathrm{m}^2}$ [1] that is fully absorbed at quantum efficiency $\eta = 0.5$ over $z = 1.0\,\mu\mathrm{m}$ into some area A. Writing generation rates r, we would see an excess generation of

$$\begin{aligned} G &= \frac{r_\text{photons}}{V}\frac{r_\text{electrons}}{r_\text{photons}} = \frac{\frac{P}{E_\text{photon}}}{Az}\eta = \frac{IA}{hf}\,\frac{\eta}{Az} \\ &= \frac{1}{hf}\,\frac{\eta I}{z} = 1.26\times 10^{24}\,\frac{1}{\mathrm{m}^3\,\mathrm{s}} = 1.26\times 10^{18}\,\frac{1}{\mathrm{cm}^3\,\mathrm{s}} \end{aligned}$$

with, using $\tau_\mathrm{h} = 100\,\mu\mathrm{s}$, a predicted change in conductivity of

$$\begin{aligned} \Delta\sigma &= e\,G\,\mu_\mathrm{h}\,\tau_\mathrm{h} \\ &= 9.2\times 10^{-1}\,\frac{1}{\Omega\,\mathrm{m}} \end{aligned}$$

on an unperturbed conductivity of about

$$\begin{aligned} \Delta\sigma &= e\,\mu_\mathrm{h}\,p \\ &= 8.3\times 10^{-3}\,\frac{1}{\Omega\,\mathrm{m}} \end{aligned}$$

for $p = 1\times 10^{12}\,\frac{1}{\mathrm{cm}^3}$ leading to a net resistivity change from $\sigma^{-1} = 120\,\Omega\,\mathrm{m}$ to $\sigma^{-1} = 1.1\,\Omega\,\mathrm{m}$.

The conductivity change scales linearly in carrier lifetime and generation rate. This means that as long as this equation did not overestimate their product by more than four orders of magnitude, the change in resistivity will be more than 1%.

A more realistic approach treats the generation rate as a function of depth. Absorption in the material leads to the skin depth l_s, a length scale for the reduction in wave energy, as discussed in appendix B. Since $I \propto \mathrm{e}^{-\frac{z}{l_\mathrm{s}}}$ we have

$$\begin{aligned} G(z) &= \frac{r_\text{photons}}{V}\frac{r_\text{electrons}}{r_\text{photons}} \\ &= \frac{dN_\text{photons}}{A\,dz}\eta = \frac{\eta}{hf}\frac{dI}{dz} \\ &= \frac{\eta}{hf}\frac{I(z)}{l_\mathrm{s}} \end{aligned}$$

An additional effect is that carriers on the surface will recombine exceedingly rapidly due to the huge crystal defect the surface represents. Carriers from the bulk will tend to diffuse towards this region where no excess carriers exist.

---

[1] Bright light; a normal light bulb at $70\,\mathrm{cm}$, three orders less than sunlight.

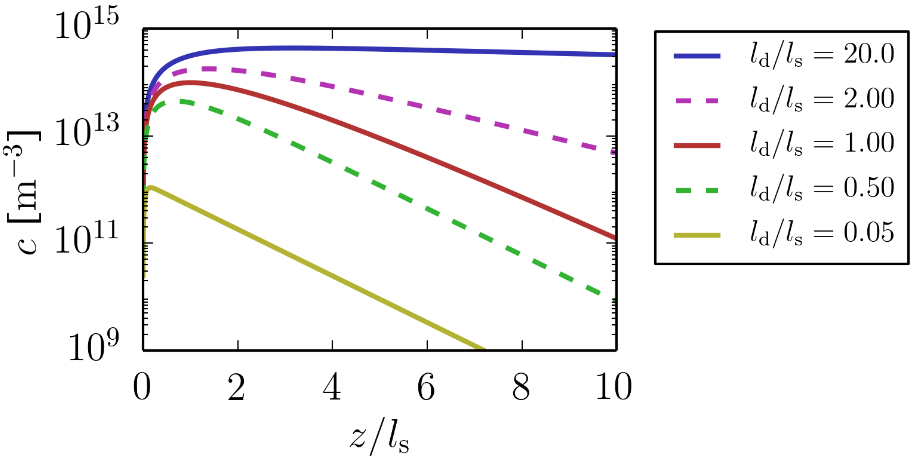

Figure 3.1: Excess carrier concentration profiles in a semi-infinitely thick wafer. Concentration is shown versus depth in the material. The skin depth and the diffusion length provide two relevant length scales. At low carrier lifetimes diffusion has a small effect, but concentrations are small anyway due to the same small lifetimes.

Considering photogeneration, recombination and diffusion we then have two equations for carrier concentration. The first is simply $c = 0$ at the surface. The second is

$$\frac{dc}{dt} = \frac{\eta}{hf}\frac{I(z)}{l_\mathrm{s}} - \frac{c}{\tau} + D\,\frac{d^2c}{dz^2} \tag{3.2}$$

This can be solved in the steady state, where $\frac{dc}{dt} = 0$. Using a minority carrier diffusion length $l_\mathrm{d} = \sqrt{D\,\tau}$, [2]

$$c(z) = \frac{\eta}{hf}\frac{\tau\,I_0}{l_\mathrm{s}(1 - \frac{l_\mathrm{d}^2}{l_\mathrm{s}^2})}(\,\mathrm{e}^{-\frac{z}{l_\mathrm{s}}} - \mathrm{e}^{-\frac{z}{l_\mathrm{d}}}\,) \tag{3.3}$$

Note that for vanishing diffusion length, this reduces to the generation rate. Differentiation shows that the concentration peaks at $z = \frac{l_\mathrm{d}l_\mathrm{s}}{l_\mathrm{d}-l_\mathrm{s}}\log\left(\frac{l_\mathrm{d}}{l_\mathrm{s}}\right)$. The peak value increases with diffusion length.

This solution does not work for $l_\mathrm{s} = l_\mathrm{d}$; there, $c(z) = \frac{\eta\,\tau\,I_0}{hf}\frac{\frac{z}{l_\mathrm{s}}\,\mathrm{e}^{-\frac{z}{l_\mathrm{s}}}}{2l_\mathrm{s}}$ which neatly peaks at $z = l_\mathrm{s}$.

The curves for a set of $l_\mathrm{d}/l_\mathrm{s}$ ratios are shown in figure 3.1.

Equation 3.3 is not the only mathematical solution to the diffusion equations, as multiples of $\mathrm{e}^{-\frac{z}{l_\mathrm{d}}} - \mathrm{e}^{\frac{z}{l_\mathrm{d}}}$ can be added at will. In the present system however any such addition leads to a non-physical solution, as the positive exponential implies ever-increasing carrier concentrations at large z.

In a system of finite thickness, the situation is different. Neglecting reflection at the back plane, we have the same diffusion equation 3.2. For boundary conditions we have at the front plane still $c(0) = 0$, but now also $c(l_\mathrm{w}) = 0$.

We can now use the free parameter in the previous solution to settle the second boundary condition, resulting in

$$c(z) = \frac{\eta}{hf}\frac{\tau\,I_0}{l_\mathrm{s}(1 - \frac{l_\mathrm{d}^2}{l_\mathrm{s}^2})}\left(\mathrm{e}^{-\frac{z}{l_\mathrm{s}}} - \mathrm{e}^{-\frac{z}{l_\mathrm{d}}} + \frac{\mathrm{e}^{-\frac{l_\mathrm{w}}{l_\mathrm{d}}} - \mathrm{e}^{-\frac{l_\mathrm{w}}{l_\mathrm{s}}}}{\mathrm{e}^{\frac{l_\mathrm{w}}{l_\mathrm{d}}} - \mathrm{e}^{-\frac{l_\mathrm{w}}{l_\mathrm{d}}}}(\,\mathrm{e}^{\frac{z}{l_\mathrm{d}}} - \mathrm{e}^{-\frac{z}{l_\mathrm{d}}}\,)\right) \tag{3.4}$$

From this equation, we can predict concentration profiles as a function of excess carrier lifetime (figure 3.2) and incident light wavelength (figure 3.3).

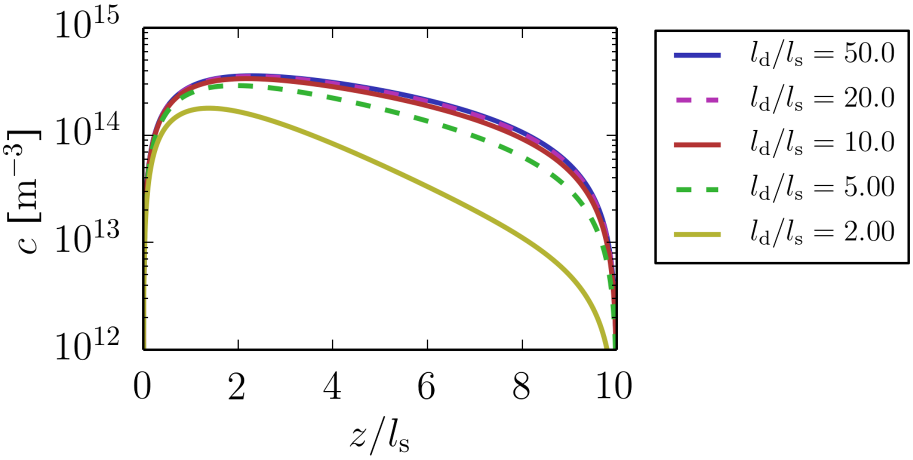

Figure 3.2: Excess carrier concentration profiles in a wafer of finite thickness. Concentration is shown versus depth in the material. There are three relevant length scales here. Skin depth and sample thickness are fixed at $l_\mathrm{w}/l_\mathrm{s} = 10.0$. This image may describe an $l_\mathrm{w} = 5\,\mu\mathrm{m}$ sample at green light, where $l_\mathrm{s} \approx 500\,\mathrm{nm}$.

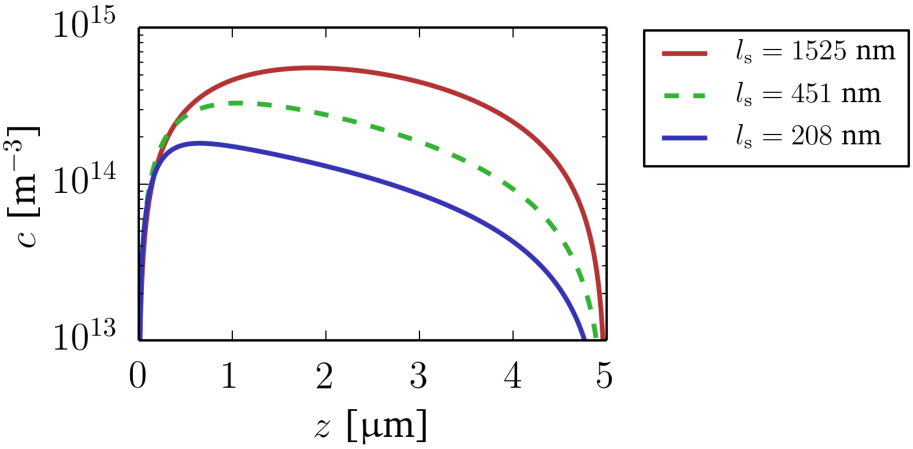

Figure 3.3: The effect of light colour on excess carrier concentration profiles, otherwise like figure 3.2. The curves represent red ($\lambda = 630\,\mathrm{nm}$), green ($\lambda = 500\,\mathrm{nm}$) and blue ($\lambda = 450\,\mathrm{nm}$) light respectively. Diffusion length is kept constant at $l_\mathrm{d} = 10\,\mu\mathrm{m}$ while wafer thickness is fixed at $l_\mathrm{w} = 5\,\mu\mathrm{m}$. Illumination at different frequencies simultaneously will produce the sum of each colour's separate effect.

A more systematic approach to solving these types of problems uses Green's functions, a type of function that characterises the differential operator. We are interested in a function $G(\mathbf{r})$ that satisfies

$$L\,G(\mathbf{r}) = -\delta(\mathbf{r})$$

using Dirac delta function δ.

From the Green's function, the steady state charge carrier distribution can be calculated through

$$c(\mathbf{r}) = \chi(\mathbf{r}) + \iiint G(\mathbf{r}-\mathbf{r}')\,f(\mathbf{r}')\,d^3\mathbf{r}'$$

where the rightmost term is called the source term and represents the external perturbation on c. χ is a solution to

$$L\,\chi(\mathbf{r}) = 0$$

and generally allows some freedom to satisfy boundary conditions.

We try to reproduce the above result using the Green's functions technique. The equation to be solved is

$$\frac{dc}{dt} = \frac{\eta}{hf}\frac{I_0}{l_\mathrm{s}}\,\mathrm{e}^{-\frac{z}{l_\mathrm{s}}} - \frac{c}{\tau} + D\,\frac{d^2c}{dz^2} \tag{3.5}$$

or, in the steady state,

$$\begin{aligned} L\,c + f(z) &= 0 \\ \text{with}\quad L &= \frac{d^2}{dz^2} - \frac{1}{l_\mathrm{d}^2} \\ f(z) &= \frac{\eta}{hf}\frac{\tau}{l_\mathrm{d}^2}\frac{I_0}{l_\mathrm{s}}\,\mathrm{e}^{-\frac{z}{l_\mathrm{s}}} \end{aligned}$$

This equation can be transformed to momentum space as

$$\begin{aligned} \mathcal{F}\left(\frac{d^2}{dz^2}G(z) - \frac{1}{l_\mathrm{d}^2}G(z)\right) &= \mathcal{F}(-\delta(z)) \\ (-k^2 - \frac{1}{l_\mathrm{d}^2})G(k) &= -1 \\ G(k) &= \frac{1}{k^2 + \frac{1}{l_\mathrm{d}^2}} \end{aligned}$$

Direct inverse Fourier transformation then gives[3]

$$G(z) = \mathcal{F}^{-1}\left(\frac{1}{k^2 + \frac{1}{l_\mathrm{d}^2}}\right) = \frac{l_\mathrm{d}}{2}\,\mathrm{e}^{-|\frac{z}{l_\mathrm{d}}|}$$

---

[2] The diffusion constant D for a particle of charge e can be found from electrical mobility μ using the Stokes-Einstein relation $D = \mu\,k_\mathrm{B}T/e$.

[3] This is evident as

$$\mathcal{F}\left(\mathrm{e}^{-|\frac{z}{l_\mathrm{d}}|}\right) = \int \mathrm{e}^{-|\frac{z}{l_\mathrm{d}}|}\,\mathrm{e}^{ikz}dz = \int_{-\infty}^{0} \mathrm{e}^{\frac{z}{l_\mathrm{d}}+ikz}dz + \int_{0}^{\infty} \mathrm{e}^{-\frac{z}{l_\mathrm{d}}+ikz}dz = \frac{1}{\frac{1}{l_\mathrm{d}}+ik} + \frac{1}{\frac{1}{l_\mathrm{d}}-ik} = \frac{2}{l_\mathrm{d}}\frac{1}{k^2+l_\mathrm{d}^2}$$

We can also solve

$$L\,\chi(\mathbf{r}) = 0$$
$$\chi(z) = c_1\,\mathrm{e}^{\frac{z}{l_\mathrm{d}}} + c_2\,\mathrm{e}^{-\frac{z}{l_\mathrm{d}}}$$

We first calculate the source term,

$$\begin{aligned}
c(z) - \chi(z) &= \int_0^{l_\mathrm{w}} G(z-z')f(z')dz' \qquad | \qquad f(z) = \frac{\eta}{hf}\frac{\tau}{l_\mathrm{d}^2}\frac{I_0}{l_\mathrm{s}}\,\mathrm{e}^{-\frac{z}{l_\mathrm{s}}} \\
&= \frac{\eta}{hf}\frac{\tau}{l_\mathrm{d}^2}\frac{I_0}{l_\mathrm{s}}\frac{l_\mathrm{d}}{2}\int_0^{l_\mathrm{w}} \mathrm{e}^{-\frac{|z-z'|}{l_\mathrm{d}}}\,\mathrm{e}^{-\frac{z'}{l_\mathrm{s}}}dz' \\
&= \frac{1}{2}\frac{\eta}{hf}\frac{\tau}{l_\mathrm{d}}\frac{I_0}{l_\mathrm{s}}\left[\int_0^{l} \mathrm{e}^{-\frac{z}{l_\mathrm{d}}+\frac{z'}{l_\mathrm{d}}-\frac{z'}{l_\mathrm{s}}}dz' \;+\; \int_l^{l_\mathrm{w}} \mathrm{e}^{\frac{z}{l_\mathrm{d}}-\frac{z'}{l_\mathrm{d}}-\frac{z'}{l_\mathrm{s}}}dz'\right] \\
&= \frac{1}{2}\frac{\eta}{hf}\tau I_0\frac{1}{l_\mathrm{s}}\frac{1}{1-\frac{l_\mathrm{d}^2}{l_\mathrm{s}^2}}\left[2\,\mathrm{e}^{-\frac{z}{l_\mathrm{s}}} - [1+\frac{l_\mathrm{d}}{l_\mathrm{s}}]\,\mathrm{e}^{-\frac{z}{l_\mathrm{d}}} - [1-\frac{l_\mathrm{d}}{l_\mathrm{s}}]\,\mathrm{e}^{-\frac{l_\mathrm{w}}{l_\mathrm{d}}}\,\mathrm{e}^{-\frac{l_\mathrm{w}}{l_\mathrm{s}}}\,\mathrm{e}^{\frac{z}{l_\mathrm{d}}}\right]
\end{aligned}$$

and using the known form of χ explicitly write the excess carrier concentration

$$\begin{aligned}
c(z) &= c_1\,\mathrm{e}^{\frac{z}{l_\mathrm{d}}} + c_2\,\mathrm{e}^{-\frac{z}{l_\mathrm{d}}} + \frac{1}{2}\frac{\eta\,\tau I_0}{hf}\frac{1}{l_\mathrm{s}}\frac{1}{1-\frac{l_\mathrm{d}^2}{l_\mathrm{s}^2}}\left[2\,\mathrm{e}^{-\frac{z}{l_\mathrm{s}}} - [1+\frac{l_\mathrm{d}}{l_\mathrm{s}}]\,\mathrm{e}^{-\frac{z}{l_\mathrm{d}}} - [1-\frac{l_\mathrm{d}}{l_\mathrm{s}}]\,\mathrm{e}^{-\frac{l_\mathrm{w}}{l_\mathrm{d}}}\,\mathrm{e}^{-\frac{l_\mathrm{w}}{l_\mathrm{s}}}\,\mathrm{e}^{\frac{z}{l_\mathrm{d}}}\right] \\
\tilde{c}(z) &= \tilde{c}_1\,\mathrm{e}^{\frac{z}{l_\mathrm{d}}} + \tilde{c}_2\,\mathrm{e}^{-\frac{z}{l_\mathrm{d}}} + \mathrm{e}^{-\frac{z}{l_\mathrm{s}}} - \frac{1+\frac{l_\mathrm{d}}{l_\mathrm{s}}}{2}\,\mathrm{e}^{-\frac{z}{l_\mathrm{d}}} - \frac{1-\frac{l_\mathrm{d}}{l_\mathrm{s}}}{2}\,\mathrm{e}^{-\frac{l_\mathrm{w}}{l_\mathrm{d}}}\,\mathrm{e}^{-\frac{l_\mathrm{w}}{l_\mathrm{s}}}\,\mathrm{e}^{\frac{z}{l_\mathrm{d}}}
\end{aligned}$$

Where the tilde indicates normalisation as $c = \tilde{c}\;\frac{\eta\tau I_0}{hf}\,\frac{l_\mathrm{s}}{l_\mathrm{s}^2-l_\mathrm{d}^2}$, for readability. Applying the original differential operator to this function will return the inhomogeneity f.

Now, our first boundary equation reads $c(z=0)=0$. If this is to be true, then

$$\begin{aligned}
\tilde{c}(z=0) = 0 &= \tilde{c}_1 + \tilde{c}_2 + \mathrm{e}^{-\frac{z}{l_\mathrm{s}}} - \frac{1+\frac{l_\mathrm{d}}{l_\mathrm{s}}}{2}\,\mathrm{e}^{-\frac{z}{l_\mathrm{d}}} - \frac{1-\frac{l_\mathrm{d}}{l_\mathrm{s}}}{2}\,\mathrm{e}^{-\frac{l_\mathrm{w}}{l_\mathrm{d}}}\,\mathrm{e}^{-\frac{l_\mathrm{w}}{l_\mathrm{s}}}\,\mathrm{e}^{\frac{z}{l_\mathrm{d}}} \\
&= \tilde{c}_1 + \tilde{c}_2 + \frac{1}{2}[1-\frac{l_\mathrm{d}}{l_\mathrm{s}}]\left[1-\mathrm{e}^{-\frac{l_\mathrm{w}}{l_\mathrm{d}}}\,\mathrm{e}^{-\frac{l_\mathrm{w}}{l_\mathrm{s}}}\right] \\
\tilde{c}_1 + \tilde{c}_2 &= \frac{1}{2}[1-\frac{l_\mathrm{d}}{l_\mathrm{s}}]\left[\mathrm{e}^{-\frac{l_\mathrm{w}}{l_\mathrm{d}}}\,\mathrm{e}^{-\frac{l_\mathrm{w}}{l_\mathrm{s}}} - 1\right]
\end{aligned}$$

The second boundary condition requires $c(z=l_\mathrm{w})=0$, implying that

$$\begin{aligned}
\tilde{c}(z=l_\mathrm{w}) = 0 &= \tilde{c}_1\,\mathrm{e}^{\frac{l_\mathrm{w}}{l_\mathrm{d}}} + \tilde{c}_2\,\mathrm{e}^{-\frac{l_\mathrm{w}}{l_\mathrm{d}}} + \mathrm{e}^{-\frac{z}{l_\mathrm{s}}} - \frac{1+\frac{l_\mathrm{d}}{l_\mathrm{s}}}{2}\,\mathrm{e}^{-\frac{z}{l_\mathrm{d}}} - \frac{1-\frac{l_\mathrm{d}}{l_\mathrm{s}}}{2}\,\mathrm{e}^{-\frac{l_\mathrm{w}}{l_\mathrm{d}}}\,\mathrm{e}^{-\frac{l_\mathrm{w}}{l_\mathrm{s}}}\,\mathrm{e}^{\frac{z}{l_\mathrm{d}}} \\
&= \tilde{c}_1\,\mathrm{e}^{\frac{l_\mathrm{w}}{l_\mathrm{d}}} + \tilde{c}_2\,\mathrm{e}^{-\frac{l_\mathrm{w}}{l_\mathrm{d}}} + \frac{1+\frac{l_\mathrm{d}}{l_\mathrm{s}}}{2}\left[\mathrm{e}^{-\frac{l_\mathrm{w}}{l_\mathrm{s}}} - \mathrm{e}^{-\frac{l_\mathrm{w}}{l_\mathrm{d}}}\right]
\end{aligned}$$

Rewriting the second equation and inserting the first, we find

$$\begin{aligned}
\tilde{c}_1\left[\mathrm{e}^{\frac{l_\mathrm{w}}{l_\mathrm{d}}} - \mathrm{e}^{-\frac{l_\mathrm{w}}{l_\mathrm{d}}}\right] &= -\left[\tilde{c}_1+\tilde{c}_2\right]\mathrm{e}^{-\frac{l_\mathrm{w}}{l_\mathrm{d}}} - \frac{1+\frac{l_\mathrm{d}}{l_\mathrm{s}}}{2}\left[\mathrm{e}^{-\frac{l_\mathrm{w}}{l_\mathrm{s}}} - \mathrm{e}^{-\frac{l_\mathrm{w}}{l_\mathrm{d}}}\right] \\
&= \frac{1-\frac{l_\mathrm{d}}{l_\mathrm{s}}}{2}\left[1-\mathrm{e}^{-\frac{l_\mathrm{w}}{l_\mathrm{d}}}\,\mathrm{e}^{-\frac{l_\mathrm{w}}{l_\mathrm{s}}}\right]\mathrm{e}^{-\frac{l_\mathrm{w}}{l_\mathrm{d}}} - \frac{1+\frac{l_\mathrm{d}}{l_\mathrm{s}}}{2}\left[\mathrm{e}^{-\frac{l_\mathrm{w}}{l_\mathrm{s}}} - \mathrm{e}^{-\frac{l_\mathrm{w}}{l_\mathrm{d}}}\right] \\
&= \frac{1-\frac{l_\mathrm{d}}{l_\mathrm{s}}}{2}\,\mathrm{e}^{-\frac{l_\mathrm{w}}{l_\mathrm{d}}} - \frac{1-\frac{l_\mathrm{d}}{l_\mathrm{s}}}{2}\,\mathrm{e}^{-\frac{2l_\mathrm{w}}{l_\mathrm{d}}}\,\mathrm{e}^{-\frac{l_\mathrm{w}}{l_\mathrm{s}}} - \frac{1+\frac{l_\mathrm{d}}{l_\mathrm{s}}}{2}\,\mathrm{e}^{-\frac{l_\mathrm{w}}{l_\mathrm{s}}} + \frac{1+\frac{l_\mathrm{d}}{l_\mathrm{s}}}{2}\,\mathrm{e}^{-\frac{l_\mathrm{w}}{l_\mathrm{d}}} \\
&= \mathrm{e}^{-\frac{l_\mathrm{w}}{l_\mathrm{d}}} - \mathrm{e}^{-\frac{l_\mathrm{w}}{l_\mathrm{s}}} - \frac{1-\frac{l_\mathrm{d}}{l_\mathrm{s}}}{2}\,\mathrm{e}^{-\frac{2l_\mathrm{w}}{l_\mathrm{d}}}\,\mathrm{e}^{-\frac{l_\mathrm{w}}{l_\mathrm{s}}} + \frac{1-\frac{l_\mathrm{d}}{l_\mathrm{s}}}{2}\,\mathrm{e}^{-\frac{l_\mathrm{w}}{l_\mathrm{s}}} \\
\tilde{c}_1 &= \frac{1-\frac{l_\mathrm{d}}{l_\mathrm{s}}}{2}\,\mathrm{e}^{-\frac{l_\mathrm{w}}{l_\mathrm{d}}}\,\mathrm{e}^{-\frac{l_\mathrm{w}}{l_\mathrm{s}}} + \frac{\mathrm{e}^{-\frac{l_\mathrm{w}}{l_\mathrm{d}}} - \mathrm{e}^{-\frac{l_\mathrm{w}}{l_\mathrm{s}}}}{\mathrm{e}^{\frac{l_\mathrm{w}}{l_\mathrm{d}}} - \mathrm{e}^{-\frac{l_\mathrm{w}}{l_\mathrm{d}}}}
\end{aligned}$$

implying that

$$\begin{aligned}
\tilde{c}_2 &= \frac{1-\frac{l_\mathrm{d}}{l_\mathrm{s}}}{2}\left[\mathrm{e}^{-\frac{l_\mathrm{w}}{l_\mathrm{d}}}\,\mathrm{e}^{-\frac{l_\mathrm{w}}{l_\mathrm{s}}}-1\right]-\tilde{c}_1 \\
&= -\frac{1-\frac{l_\mathrm{d}}{l_\mathrm{s}}}{2}-\frac{\mathrm{e}^{-\frac{l_\mathrm{w}}{l_\mathrm{d}}}-\mathrm{e}^{-\frac{l_\mathrm{w}}{l_\mathrm{s}}}}{\mathrm{e}^{\frac{l_\mathrm{w}}{l_\mathrm{d}}}-\mathrm{e}^{-\frac{l_\mathrm{w}}{l_\mathrm{d}}}}
\end{aligned}$$

We can now fully describe excess carrier concentration. We write

$$\begin{aligned}
\tilde{c}(z) &= \tilde{c}_1\,\mathrm{e}^{\frac{z}{l_\mathrm{d}}}+\tilde{c}_2\,\mathrm{e}^{-\frac{z}{l_\mathrm{d}}}+\mathrm{e}^{-\frac{z}{l_\mathrm{s}}}-\frac{1+\frac{l_\mathrm{d}}{l_\mathrm{s}}}{2}\,\mathrm{e}^{-\frac{z}{l_\mathrm{d}}}-\frac{1-\frac{l_\mathrm{d}}{l_\mathrm{s}}}{2}\,\mathrm{e}^{-\frac{l_\mathrm{w}}{l_\mathrm{d}}}\,\mathrm{e}^{-\frac{l_\mathrm{w}}{l_\mathrm{s}}}\,\mathrm{e}^{\frac{z}{l_\mathrm{d}}} \\
&= \frac{1-\frac{l_\mathrm{d}}{l_\mathrm{s}}}{2}\,\mathrm{e}^{-\frac{l_\mathrm{w}}{l_\mathrm{d}}}\,\mathrm{e}^{-\frac{l_\mathrm{w}}{l_\mathrm{s}}}\,\mathrm{e}^{\frac{z}{l_\mathrm{d}}}+\frac{\mathrm{e}^{-\frac{l_\mathrm{w}}{l_\mathrm{d}}}-\mathrm{e}^{-\frac{l_\mathrm{w}}{l_\mathrm{s}}}}{\mathrm{e}^{\frac{l_\mathrm{w}}{l_\mathrm{d}}}-\mathrm{e}^{-\frac{l_\mathrm{w}}{l_\mathrm{d}}}}\,\mathrm{e}^{\frac{z}{l_\mathrm{d}}}-\frac{1-\frac{l_\mathrm{d}}{l_\mathrm{s}}}{2}\,\mathrm{e}^{-\frac{z}{l_\mathrm{d}}}-\frac{\mathrm{e}^{-\frac{l_\mathrm{w}}{l_\mathrm{d}}}-\mathrm{e}^{-\frac{l_\mathrm{w}}{l_\mathrm{s}}}}{\mathrm{e}^{\frac{l_\mathrm{w}}{l_\mathrm{d}}}-\mathrm{e}^{-\frac{l_\mathrm{w}}{l_\mathrm{d}}}}\,\mathrm{e}^{-\frac{z}{l_\mathrm{d}}} \\
&\quad+\mathrm{e}^{-\frac{z}{l_\mathrm{s}}}-\frac{1+\frac{l_\mathrm{d}}{l_\mathrm{s}}}{2}\,\mathrm{e}^{-\frac{z}{l_\mathrm{d}}}-\frac{1-\frac{l_\mathrm{d}}{l_\mathrm{s}}}{2}\,\mathrm{e}^{-\frac{l_\mathrm{w}}{l_\mathrm{d}}}\,\mathrm{e}^{-\frac{l_\mathrm{w}}{l_\mathrm{s}}}\,\mathrm{e}^{\frac{z}{l_\mathrm{d}}} \\
&= \mathrm{e}^{-\frac{z}{l_\mathrm{s}}}-\mathrm{e}^{-\frac{z}{l_\mathrm{d}}}+\frac{\mathrm{e}^{-\frac{l_\mathrm{w}}{l_\mathrm{d}}}-\mathrm{e}^{-\frac{l_\mathrm{w}}{l_\mathrm{s}}}}{\mathrm{e}^{\frac{l_\mathrm{w}}{l_\mathrm{d}}}-\mathrm{e}^{-\frac{l_\mathrm{w}}{l_\mathrm{d}}}}\left[\mathrm{e}^{\frac{z}{l_\mathrm{d}}}-\mathrm{e}^{-\frac{z}{l_\mathrm{d}}}\right] \\
c(z) &= \frac{\eta}{hf}\frac{\tau I_0}{l_\mathrm{s}(1-\frac{l_\mathrm{d}^2}{l_\mathrm{s}^2})}\left[\mathrm{e}^{-\frac{z}{l_\mathrm{s}}}-\mathrm{e}^{-\frac{z}{l_\mathrm{d}}}+\frac{\mathrm{e}^{-\frac{l_\mathrm{w}}{l_\mathrm{d}}}-\mathrm{e}^{-\frac{l_\mathrm{w}}{l_\mathrm{s}}}}{\mathrm{e}^{\frac{l_\mathrm{w}}{l_\mathrm{d}}}-\mathrm{e}^{-\frac{l_\mathrm{w}}{l_\mathrm{d}}}}\left[\mathrm{e}^{\frac{z}{l_\mathrm{d}}}-\mathrm{e}^{-\frac{z}{l_\mathrm{d}}}\right]\right]
\end{aligned}$$

which is the same as equation 3.4, previously shown to be the correct solution. This proves the applicability of the Green's function method to this type of problem.

3.1.2 Three-dimensional systems

Solving the same diffusion equation in three dimensions with four (or even two) surfaces directly is impracticable. Intuitive separation of variables does not provide the desired result.

The Green's function for the full three-dimensional problem may be found by use of Fourier transformation, contour integration and some further complex analysis. The full derivation is given in appendix C, leading to the Green's function

$$G(\mathbf{r}) = \frac{\mathrm{e}^{-\frac{r}{l_\mathrm{d}}}}{4\pi r} \tag{3.6}$$

For now neglecting boundary conditions, we can write

$$\begin{aligned}
c(\mathbf{r})-\chi(\mathbf{r}) &= \int G(\mathbf{r}-\mathbf{r}')\,f(\mathbf{r}')\,d\mathbf{r}' \\
&\propto \int \frac{\mathrm{e}^{-|\mathbf{r}-\mathbf{r}'|}}{|\mathbf{r}-\mathbf{r}'|}\,\mathrm{e}^{-z'}\,d\mathbf{r}'
\end{aligned}$$

The symmetry of this problem is cylindric. In free space, using a cylindrical coordinate system leaves the angular integration trivial. However, the remaining integral is insurmountably troublesome.

The interdependence of $\mathbf{r}'$ and z' means that there is no convenient way to rewrite the integral. We may at best hope to isolate a term $\int \frac{\mathrm{e}^u}{u}du$, which evaluates to the exponential integral special function. As this function can only be evaluated numerically, the model would require numerical evaluation whether or not the remaining integral could be solved.

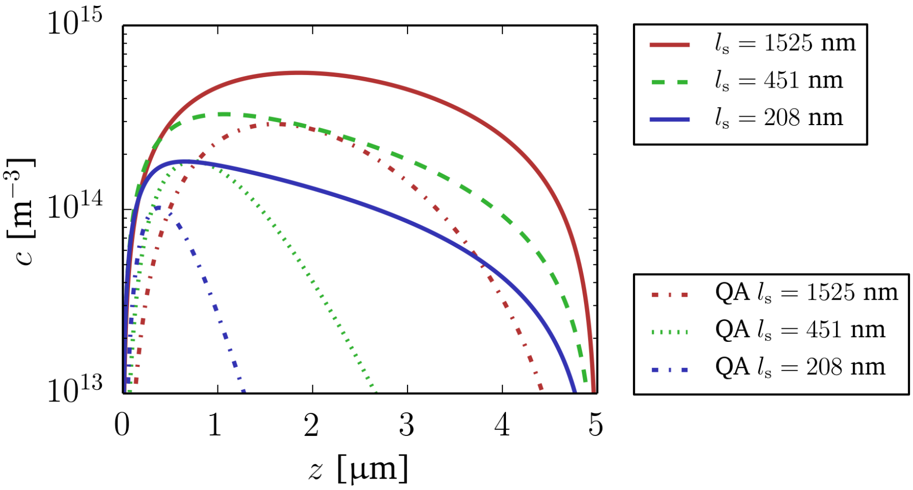

Figure 3.4: The quasi-analytic model compared with the full diffusion results for a wafer of $l_\mathrm{w} = 5\,\mu\mathrm{m}$ illuminated by red, green and blue light.

3.1.3 Quasi-analytic model

As the full three-dimensional system dynamics are too complex, it is interesting to consider a simplified model.

We have so far considered bulk recombination and surface recombination as separate effects. Instead, we may define a spatially variable effective lifetime, that takes into account the lifetime reduction due to the proximity of surfaces, as

$$\frac{1}{\tau_\mathrm{eff}} = \frac{1}{\tau} + \sum_\mathrm{faces} \frac{1}{\tau_\mathrm{s}}$$

With effective lifetime τ_eff, bulk lifetime τ and surface lifetime τ_s. Each term in this equation represents a separate loss path.

Assuming for now that all surfaces have high recombination velocities, loss is limited by diffusion. We can already see that the loss rate depends on the carrier diffusion constant, the distance from source to surface and some factor g to account for the geometry of the problem, suggesting a dependence of the form

$$\frac{1}{\tau_\mathrm{s}} = \frac{g\,D}{r^2}$$

Extensive theoretical analysis produces similar equations, involving geometric factors slightly below unity. [20]

We then require that this effective loss rate, which includes both bulk and surface recombination, balances the generation rate,

$$\frac{1}{\tau_\mathrm{s}} c(\mathbf{r}) = \frac{\eta}{hf} \frac{I_0}{l_\mathrm{s}} \mathrm{e}^{-\frac{\mathbf{r}\cdot\hat{\mathbf{z}}}{l_\mathrm{s}}}$$

This model can be compared with the full analytic diffusion solution for a one-dimensional wafer. For the present model, we find

$$c(z) = \frac{\eta}{hf} \frac{e}{k_\mathrm{B}T} \frac{1}{\mu} \frac{1}{g} \frac{I_0}{l_\mathrm{s}} \mathrm{e}^{-\frac{z}{l_\mathrm{s}}} \left(\frac{1}{z} + \frac{1}{l_\mathrm{w} + z}\right)^{-2}$$

which is shown versus the full solution in figure 3.4. The peak values are within a factor of two of the analytic results and the peak positions less than 5% off. These results are promising, especially given the simplicity of the model, and the ease of continuation to higher dimension. For an example of this continuation, consider the tetrahedron, using the same setup and coordinate system introduced in the previous section. The thick native oxide on the bottom plane vastly reduces surface lifetime, leaving the left and right back planes to be accounted for. We may then write

$$\begin{aligned} \frac{dc}{dt} = 0 &= D\,\frac{d^2}{dl^2}c - \frac{c}{\tau_{\text{eff}}} + A\ \mathrm{e}^{-\frac{z}{l_\mathrm{d}}} \\ &= D\,\frac{d^2}{dl^2}c - \frac{c}{\tau} - \frac{D}{g}\frac{c}{r_1^2} - \frac{D}{g}\frac{c}{r_2^2} + A\ \mathrm{e}^{-\frac{z}{l_\mathrm{d}}} \end{aligned}$$

This method clearly results in much simpler equations than the full diffusion analysis. However, its results are off by several orders of magnitude deeper in the material and the model requires further adjustments.

3.2 Resistor modelling

We set out to characterise the voltage-current relation between the vertices of a tetrahedron and elongated channels as seen in the pit-based detector as a function of their conductivity distributions.

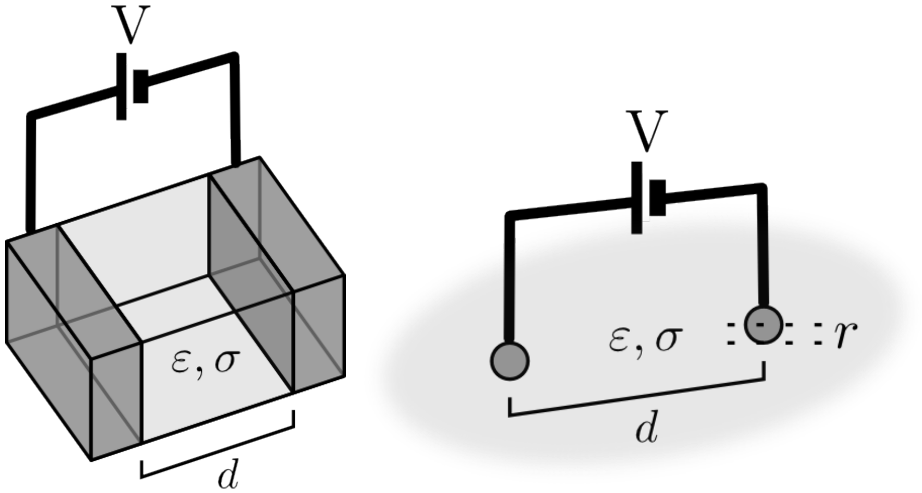

(a)

(b)

Figure 3.5: Two resistors that demonstrate the different types of measurement schemes. (a) A simple parallel-plate resistor. (b) Two conducting spheres in an infinite continuum of poorly conducting material. Either will also work as a leaky capacitor of time constant $RC = \frac{\varepsilon}{\sigma}$.

3.2.1 Standard resistor

The most common model for resistors consists of a rectangular slab of poorly conducting[4] material sandwiched between two flat and perfectly conducting contacts, as in figure 3.5a. This causes an electric field that, in the limit of large contact radius per contact separation, is uniform within the

---

[4] Unless otherwise specified, materials will also be taken as linearly polarisable, homogeneous, isotropic, and non-magnetic.

material. From the equivalent of Gauss' law, equation A.1, in matter and symmetry arguments we can write

$$\oint D\,dA = Q_f$$

$$D = 2\,\frac{Q_f}{2\,A}$$

$$E = \frac{1}{\varepsilon}\frac{Q_f}{A}$$

with Q_f whatever charge the voltage may induce on either plate. For the potential difference and current, this means

$$V = -\int \mathbf{E}\cdot d\mathbf{l} = -\frac{d}{\varepsilon}\frac{Q_f}{A}$$

$$I = \int J\,dA = \sigma E A = \sigma\frac{1}{\varepsilon}Q_f$$

which leads to a resistance value

$$R = \frac{V}{I} = \frac{d}{A}\frac{1}{\sigma}$$

confirming the interpretation of $\Omega\mathrm{m}$ as $\Omega\mathrm{m}^2/\mathrm{m}$.

3.2.2 Infinite bulk resistor

Another type of electrical system is illustrated in figure 3.5b, where two distant, perfectly conducting spheres are connected by an extradimensional voltage source in an infinite continuum of poorly conducting material.

The charge on these spheres will distribute itself on the surface and outside the sphere produce the same field as a point charge. Linearity implies that the total electric field is just the sum of the field of each sphere. Again using Gauss' law we may find that outside the spheres

$$\mathbf{E} = \frac{1}{\varepsilon}\left(\frac{Q_f}{4\pi R_+^2} + \frac{-Q_f}{4\pi R_-^2}\right)\hat{\mathbf{r}}$$

with R distance from each sphere center. Voltage is easily found along the shortest path between the spheres as

$$\begin{aligned} V = -\int \mathbf{E}\cdot d\mathbf{l} &= -\int_r^{d-r} \frac{Q_f}{4\pi\varepsilon}\left(\frac{1}{R^2} - \frac{1}{(d-R)^2}\right) dR \\ &= -\frac{Q_f}{4\pi\varepsilon}\,2\int_r^{d-r} \frac{1}{R^2}\,dR = \frac{Q_f}{2\pi\varepsilon}\left(\frac{1}{d-r} - \frac{1}{r}\right) \end{aligned}$$

while current is found through

$$I = \oint \mathbf{J}\cdot d\mathbf{A} = \oint \sigma\mathbf{E}\cdot d\mathbf{A} = \frac{\sigma Q_f}{\varepsilon}$$

so all in all

$$R = \frac{V}{I} = \frac{1}{2\pi\sigma}\left(\frac{1}{r} - \frac{1}{d-r}\right) \approx \frac{1}{2\pi r}\frac{1}{\sigma}$$

which is remarkable. As long as the spheres are far apart, the precise distance hardly matters for the resistance between them.

This must be explained from the idea that the high current densities close to the sphere limit current. Most energy is dissipated in this region, instead of in the bulk, where tiny currents flow due to the huge area over which they are distributed.

Note also that if in this picture only half the universe is conductive, with the spheres on the interface, resistance will exactly double. For symmetry reasons no current crosses the interface in any case, so half the current paths disappear without changing the potential, thus doubling resistance. This model might also work to describe probe resistance measurements on bulk material.

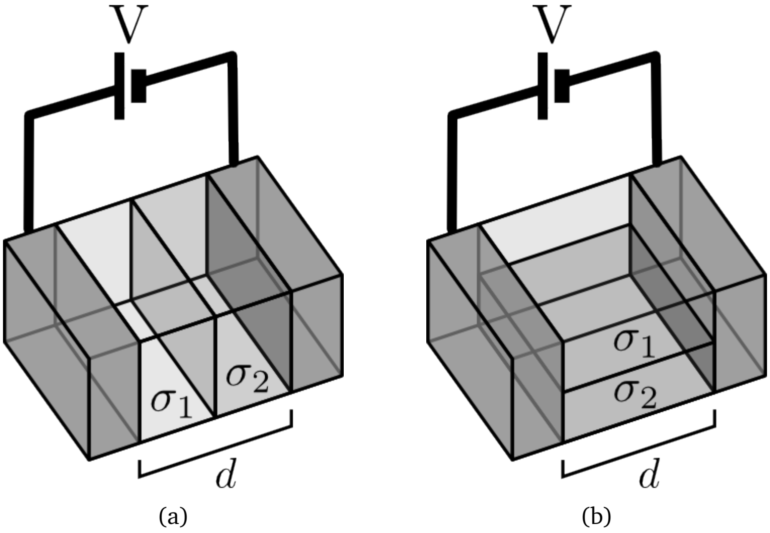

(a) (b)

Figure 3.6: Two resistors of inhomogeneous conductivity.

3.2.3 Variable conductivity resistors

Figure 3.6 shows two elementary types of non-homogeneous resistors.

The system in figure 3.6a has a conductivity that varies along its axis. It can be analysed by using the result from the basic resistor described before.

Because cross-sections parallel to the contacts are equipotentials, the material on either side is a resistor in its own right. This bisection can be repeated, so that

$$R = \int dR = \int \frac{1}{\sigma} \frac{dz}{A} \tag{3.7}$$

with A and possibly σ variable along the resistor.

This simple argument hides some interesting physics. At each interface, surface charge will build up. The magnitude of this charge is determined by the ratio of conductivities on either side. In case of a conductivity gradient, space charge will exist.

Note that this equation can also be used to describe varying cross-section or more complex shapes. The one requirement is that the integration is done over equipotential planes.

Figure 3.6b shows a resistor with a conductivity varying perpendicular to the axis. Although conductivities are different, both slabs are linear and have the same potential drop over the same distance. This means that the equipotential planes are still parallel to the conductor surfaces and no current flows from either region into the other. This means that for arbitrary patterns

$$R = \int \frac{1}{\int \sigma \, dA} \, dz \tag{3.8}$$

with the first integration over the equipotential planes, and the second integration over each specific equipotential plane.

This also shows that for resistors such as discussed in section 3.1, we need only consider the average conductivity over an equipotential plane.

In systems of general conductivity distribution, finding the equipotential surfaces is hard if at all possible. [26]

In steady state conductivity, no further charge build-up occurs. This means that $\nabla \cdot \mathbf{J} = 0$. Since however $\mathbf{J} = \sigma \mathbf{E}$,

$$\begin{aligned} 0 = \nabla \cdot \mathbf{J} = \nabla \cdot (\sigma \mathbf{E}) = \sigma \, \nabla \cdot \mathbf{E} + \nabla \sigma \cdot \mathbf{E} \\ \nabla \cdot \mathbf{E} = -\frac{\nabla \sigma \cdot \mathbf{E}}{\sigma} \\ \rho = -\frac{\nabla \sigma}{\sigma} \cdot \epsilon \mathbf{E} \end{aligned}$$

This nicely confirms our previous results, in that charge build-up occurs in those locations where the local electric field points along a conductivity gradient. However, it also shows that the exact current distribution in a resistor of complicated conductance pattern must generally be found by solving a three-dimensional differential equation.

3.2.4 Wafers

The usual technique for determining material resistivity is the four-point current/voltage-measurement on the full wafer level. Typically, resistivity is found as the ratio between applied current and resulting voltage or vice versa times a predetermined correction factor. This factor depends on sample geometry as well as probe positioning and spacing. In past and more recent times significant effort has been made in numeric evaluation of these constants for different kinds of geometries.[27][28]

Evaluation simplifies somewhat if current injection is done near the far ends of a symmetric sample. The current profile around the middle part will then have evened out any effects from the localised injection and voltage will drop off linearly with distance as in the basic resistor (fig. 3.5a). Voltage probes placed near the middle of the sample can then be used with these simple equations to evaluate conductivity.

3.2.5 Tetrahedra

A tetrahedron resistor will realistically be contacted by covering two tips in highly conductive material. The precise current distribution resulting in a homogenous sample in such a setup will be complicated, with curved equipotential planes as illustrated in figure 3.7a.

Alternatively, we can try to express the resistivity of such a sample by equation 3.7. The problem simplifies appreciably if the equipotentials are approximated by a series of parallel planes as in figure 3.7b. This also implies that two such planes are contacted. Then,

$$R = \int_{\delta}^{r-\delta} \frac{dz}{\sigma A} = \frac{2}{\sigma} \int_{\delta}^{r/2} \frac{dz}{A} = \int_{\delta}^{r/2} \frac{\sqrt{2}}{4} \frac{dz}{z^2} = \frac{\sqrt{2}}{2\sigma} \left(\frac{1}{\delta} - \frac{2}{r} \right)$$

The contact produced by a focused ion beam path of width $w = 250\,\mathrm{nm}$ might result in a contact equivalent area of $w^2 = 0.24\,\mu\mathrm{m}^2$. This is the area of the tetrahedron after $\delta = 0.28\,\mu\mathrm{m}$. Together with a tetrahedron edge length of $r = 10\,\mu\mathrm{m}$ and a conductivity of $1/\sigma = 120\,\Omega\,\mathrm{m}$ we would get

$$R = 286\,\mathrm{M}\Omega$$

which means that at an input voltage in the order of volts, the resulting current will be in the order of nanoamperes.[5]

---

[5] This result may be found surprising. Note that a cubic basic resistor as described before has a resistance of $R = \frac{1}{\sigma r}$, which for a $5\,\mu\mathrm{m}$ cube means $R \approx 24\,\mathrm{M}\Omega$.

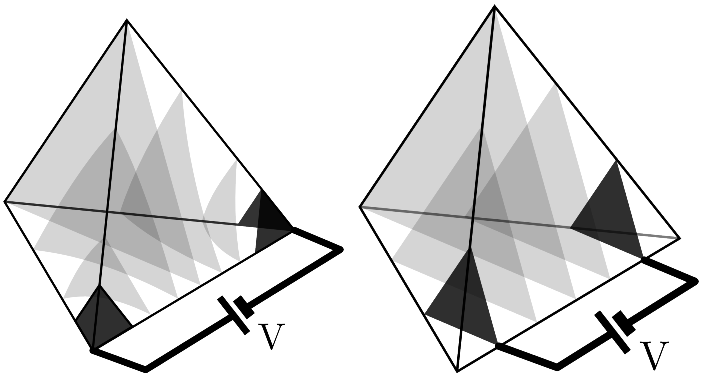

(a) (b)

Figure 3.7: Equipotential planes in an electrically contacted tetrahedron of uniform conductivity. For a tetrahedron contacted on the outside of its tips, we expect the equipotentials to be somewhat curved and have different overall directions moving from one contact to the other, as shown in (a). A simplified model takes all the equipotential planes to be parallel as shown in (b).

3.3 Pit-based detector

The dark case for the pit-based detector is quite understandable. Given a channel with two anisotropically etched walls and conductivity σ, device layer thickness h, channel top face width w and channel length L, we expect a resistance of

$$R = \frac{z}{\sigma}\frac{1}{A} = \frac{z}{\sigma}\left(\frac{h^2}{\tan(54.74°)} + h\,w\right)^{-1}$$

When light is incident on the detector surface however, several things happen. Part of the light reflects away from the sensor, as per the Fresnel equations discussed in appendix A. The transmitted light refracts strongly in the high index of silicon, propagating practically parallel to the surface. It gets absorbed along the way in as described in section 3.1 and undergoes total internal reflection on the oxide. In principle the light keeps reflecting about until absorbed or coupled back out of the material, but as skin depth does not go beyond a few micrometres in the visible regime this does not seem very relevant. This process is shown schematically in figure 3.8.

With the models available it seems most appropriate to try and model the channel as a resistor with a one-dimensional conductivity pattern along the direction of propagation of light. This is quite a simplification, as it ignores the buried oxide reflection, as well as shadowing effects from the channel top face, shown as the reflected and small arrows in figure 3.8. Still it is clearly better than approximations along the oxide plane, as those will be off several skin depths either at the top or the bottom of the surface. Another effect that helps justify the approximation is that the neglecting of the oxide reflection competes with the fact that there are more absorbing surfaces within reach where the detector surface meets the oxide. The shadowing competes with the slight retraction of the mirror. We may also note that the reflected light moves nearly parallel to the detector surface. Effective carrier lifetime is much low in this region than in the bulk of the channel.

From equation 3.8 we know that for an inhomogeneous but one-dimensional resistor,

$$R = \int \frac{1}{\int \sigma\, dA}\, dz$$

Now, we can divide the cross-section of the resistor in two parts: a parallellogram with the surface as one edge and the channel top face as another, and the remaining triangle, indicated by the dashed line in figure 3.8. Geometry shows that, seen from the incoming light, the triangle has a base of $s = \frac{h}{\tan(54.74°)}$ and a height of $\Delta z = 2h\cos(54.74°)$.

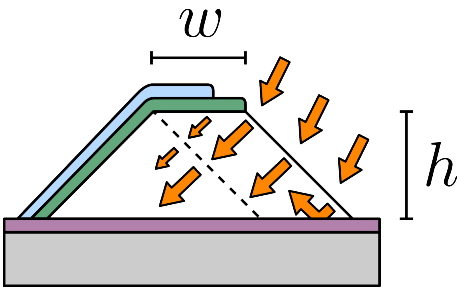

Figure 3.8: A schematic cross-section of a pit-based detector channel. Silicon is shown in grey with the buried oxide in violet. The thermal oxide is green and covered with the aluminium in blue. Light is incident from a point right of normal. The orange arrows indicate the direction of light rays.

Now, with conductivity $\sigma = \sigma_0 + e\mu_e c$, plugging equation 3.4 we can directly integrate over z to find the conductance. With $\psi = 54.74°$ for readability, we write

$$R = \int \frac{1}{\int \sigma \, dA} \, dz = \frac{z}{\sigma_0 A + \int \Delta\sigma \, dA}$$

$$\int \Delta\sigma \, dA = \int_0^{w \sin\psi} \sigma(z) \, \frac{h}{\tan\psi} \, dz \quad + \quad \int_0^{2h\cos\psi} \sigma(z + w\sin\psi) \, \frac{h}{\tan\psi} \left(1 - \frac{z}{2h\cos\psi}\right) dz$$

In this way, we can find a (horribly complicated) analytic expression for the conductivity of the channel. We are more interested however in its behaviour as a function of incident angle. We know that the $\Delta\sigma$ term is linear in radiance at the surface L. The conductivity change is then directly determined by the change in radiance of the light entering the material.

As discussed in appendix A, light polarised parallel to its plane of incidence on the surface has a different transmission coefficient $T^{\parallel}$ than the transmission coefficient $T^{\perp}$ for perpendicularly polarised light. With θ the zenith angle with respect to the detector surface normal, L the relevant radiant flux magnitudes and n the refractive index ratio between silicon and air, we can write

$$\begin{aligned} L_{\mathrm{Si}} &= \frac{1}{2}(T^{\perp} + T^{\parallel}) \cos(\theta) \, L_{\mathrm{Air}} \\ &= \left[1 - \frac{1}{2} \left| \frac{\cos\theta - n\sqrt{1 - \frac{1}{n^2}\sin^2\theta}}{\cos\theta + n\sqrt{1 - \frac{1}{n^2}\sin^2\theta}} \right|^2 - \frac{1}{2} \left| \frac{\sqrt{1 - \frac{1}{n^2}\sin^2\theta} - n\cos\theta}{\sqrt{1 - \frac{1}{n^2}\sin^2\theta} + n\cos\theta} \right|^2 \right] \cos(\theta) \, L_{\mathrm{Air}} \end{aligned}$$

This function is shown versus angle in figure 3.9. In a light detection situation, the detector will be oriented $\theta = 54.74°$ off-normal. In that coordinate system, the curve will thus be shifted by that amount, while the opposite detector shifts the other way.

When taking measurements, we do not find the resistor values in the four-resistor model. What we do get, using the terminology from figure 2.6, is

$$\begin{aligned} R_{12} &= \alpha \,//\, (\beta + \gamma + \delta) \\ R_{23} &= \beta \,//\, (\gamma + \delta + \alpha) \\ R_{34} &= \gamma \,//\, (\delta + \alpha + \beta) \\ R_{41} &= \delta \,//\, (\alpha + \beta + \gamma) \end{aligned}$$

These are four equations with four unknowns and since the resistor network itself is linear, a unique solution exist. Finding it is nevertheless very tricky.

We may start by solving the equations for R_{23} and R_{34} for α and equating them. α and δ are then eliminated, leaving

$$\frac{R_{23}\beta}{R_{23} - \beta} + \beta = \frac{R_{34}\gamma}{R_{34} - \gamma} + \gamma$$

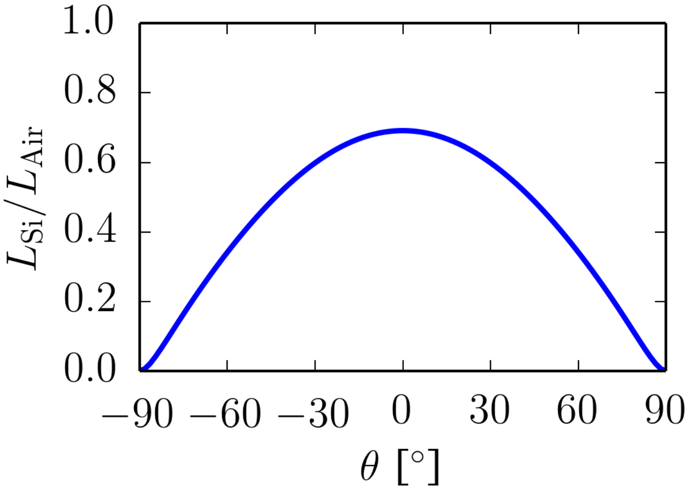

Figure 3.9: The radiant flux transmission from air to a silicon slab as a function of incident angle. Note that unlike an ordinary cosine, the curve flattens off towards the $\pm 90^\circ$ asymptotes.

This quadratic equation can be solved for either variable. Repeating this trick for all resistors we can find a convoluted implicit expression for any resistor in measurables. Squaring out the roots however gives an eighth-order equation. This can only be solved to first order, giving

$$\alpha = \frac{R_{12}(R_{23} + R_{34} + R_{41})}{R_{23} + R_{34} + R_{41} - \frac{1}{3}R_{12}}$$

This equation is however off by tens of percents for a ring of identical resistors. With the knowledge that the resistors are of comparable size, we can tune this solution to fit the trivial case where all resistors are the same. We then find that in good approximation,

$$\alpha = \frac{R_{12}(R_{23} + R_{34} + R_{41})}{R_{23} + R_{34} + R_{41} - \frac{3}{4}R_{12}}$$

and analogous equations for β, γ and δ. For resistor values within a factor two of one another, the approximation is good to within 3%.

3.4 Tetrahedron-based detector

If we apply the three-resistor model to the calculation of the resistance of a tetrahedron, we find an indication of the dark resistance values for a $r = 10\,\mu\mathrm{m}$ tetrahedron as

$$\alpha_{\text{dark}} = \beta_{\text{dark}} = \gamma_{\text{dark}} = \frac{3}{2}R_{\text{vertex-vertex}} \approx 450\,\mathrm{M\Omega}$$

This is something of a worst-case scenario, working with small tetrahedra and very small contacts.

We also note that this sort of value need not be problematic. Extensive information on high-impedance measurements is available.[29] In summary, surfaces need to be extremely clean and dry.[6] The HP/Agilent 3458A multimeter datasheet states that it measures resistances of $R = 1\,\mathrm{G\Omega}$ with a resolution of $\Delta R = 10\,\Omega$. At the large predicted relative conductivity change, this should be plenty.

The behaviour under illumination is not so clear. The carrier dynamics theory in section 3.1 does not give us more than a good indication of the order of magnitude of effects. This means

---

[6] It is encouraging that the same source discusses measuring currents of $I = 1\,\mathrm{fA}$.

that, barring further theoretical development or numerical simulation, the devices will have to be calibrated.

Even if the resistance values cannot be found quantitatively, some statements about observability can be made.

Two types of measurement could be considered for the tetrahedron. The first would be to apply a voltage over two contacts. This produces a current, and also sets the voltage for the unused contact. Using the three-resistor model and at first ignoring contact resistance, we can describe the result of a measurement. For an applied potential between pins 1 and 2,

$$\begin{aligned}\frac{U_{1,2}}{I} &= \alpha//(\beta+\gamma)\\ \frac{U_{3,2}}{U_{1,2}} &= \frac{\beta}{\beta+\gamma}\end{aligned}$$

From this, the ratio $\frac{\beta}{\gamma} = F_1$ can be found. However, the ratio between either and α is still unknown, as well as their absolute magnitudes.

Two successive measurements using different pairs of contacts provide more information. If in addition to the $U_{1,2}$ measurement above, a $U_{2,3}$ measurement is done, we know $\frac{\gamma}{\alpha} = F_2$, so that

$$\begin{aligned}\frac{U_{1,2}}{I} &= \alpha//(\beta+\gamma)\\ &= \alpha//(F_1F_2\alpha + F_2\alpha)\\ \gamma &= \frac{1}{1+\frac{1}{F_1+F_2}}\frac{U_{1,3}}{I}\end{aligned}$$

from which α and β can also be calculated. The third possible measurement can be used as a complementary extra data point. Thus, with a periodic sequence of measurements, the absolute resistance values for the three-contact tetrahedron can be determined.

Alternatively, we can use simple two-point measurements to find all resistor values. Using the resistor naming scheme from figure 2.9, we have

$$\begin{aligned}R_{12} &= \alpha//(\beta+\gamma)\\ R_{23} &= \beta//(\gamma+\alpha)\\ R_{31} &= \gamma//(\alpha+\beta)\end{aligned}$$

these equations are fully interdependent, but can be solved to express the internal resistors in the measurables,

$$\alpha = \frac{\frac{1}{2}R_{12}^2 + \frac{1}{2}R_{23}^2 + \frac{1}{2}R_{31}^2 - R_{12}R_{23} - R_{23}R_{31} - R_{31}R_{12}}{R_{23}+R_{31}-R_{12}}$$

and analogous equations for β and γ.

Consider a single light source illuminating a single tetrahedron. The azimuthal angle can be determined if two planes are more strongly illuminated than the third. The source must then be on the bright side. The ratio between the brightly lit plane resistances then reveals the azimuthal angle.

The requirement of two illuminated planes is satisfied only in certain orientations. Figure 3.10a shows that for a light source in the ground plane, sources in three regions, II, IV and VI, will have a quantifiable azimuthal position. Otherwise, in regions I, III and V, only the region can be determined. For remote light sources, each region will have an extension of $\theta = 60°$. At positive elevation, the blind regions decrease in size.

Zenith angle is best found at near-normal incidence. For a light source directly above the tetrahedron, a small change in zenith will change the balance between intensity on the planes on its side, and the planes on the far side. At some point, the far-side planes will be perpendicular

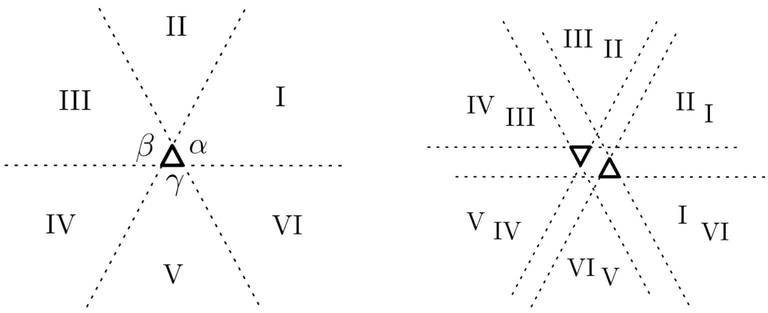

(a)

(b)

Figure 3.10: (a) For a light source far away on the ground plane, six regions can be defined. In regions II, IV and VI, a small change in azimuthal angle changes the irradiance ratio between two planes. In regions I, III and V, the only change is on a single plane. (b) Two tetrahedra facing one another cancel out all blind regions. However, no means of technological realisation is obvious.

to the light source direction and no longer receive light. Here, another blind region starts. The lowest blind point occurs when the source moves directly away from one plane, in that case at $\phi = 70.53°$. The highest is in exactly the opposite direction at $\phi = 54.74°$. The visible angle along this line would be $\Delta\phi = 54.74°$; if multiple sensors are combined optimally, this could increase to $\Delta\phi = 70.53°$.

3.5 Colour vision

Modern image sensors are able to distinguish light colour. Typically, the image sensor pixels are divided into subpixels particularly sensitive to either red, green or blue light.[7] Alternative approaches use different sets of colours; any linearly independent three-colour basis can be used to solve for light intensity around the red, green and blue peaks.

There are a few ways to introduce the colour sensitivity to the camera.

Industry standard is to put the subpixels side by side on a single sensor, covered with different miniature colour filters. Many possible layouts for the subpixels and sets of colours have been tried. By far the most common uses a repeating 2×2 grid with a red and a blue subpixel at opposing squares and two green subpixels in the other. [30][1]

The natural downside of this method is the loss of spatial resolution caused by the need to combine subpixels to find pixel colour. In addition, light absorbed by the colour filters does not contribute to the signal. Compared to the red-green-blue layout this effect can be halved by using a magenta-yellow-cyan layout and reduced further with a variation on magenta-cyan-white. Interestingly, analysis shows that the processing - that is, $G = Cy + Ye - Ma$ - actually produces a worse signal to noise ratio than wasting half the light does. Consider $R = G = B = \mathrm{N}(1, \sigma^2)$. Since $\mathrm{N}(1, \sigma^2) + \mathrm{N}(1, \sigma^2) = \mathrm{N}(2, 2\sigma^2)$, $Cy = Ye = Ma = \mathrm{N}(2, 2\sigma^2)$. Then, $G = Cy + Ye - Ma = \mathrm{N}(2, 6\sigma^2)$, reducing signal quality by $\sqrt{\frac{3}{2}}$ through the need for subtraction.[8] A few commercial cameras use such alternative schemes.[9] These have been reported to be more noisy and have lower colour fidelity.[1]

An alternative approach is to stack the subpixels behind one another in the sensor. The wavelength-dependence of skin depth in the detector bulk means that only long-wavelength light reaches the rear subpixel. With several such layers, the original spectrum can be reconstructed.

---

[7] The representation of colour is only visually perfect if the spectral sensitivity of the subpixels is exactly the same as that of the pigments in the human eye. This will not happen.

[8] This calculation assumes that all noise can be modelled as normally distributed in the red, green and blue channels.

[9] For example the Kodak 620x camera [31] from 2000 does.

This technique is in small-scale commercial exploitation. [32] For the devices considered in this work, multiple layers of subpixels will not have the desired effect.

Colour filters can be made using either pigments or dyes. Pigments are more popular due to higher heat resistance and slower bleaching. [1]

An interesting thought is the use of multilayer mirrors to filter out specific wavelength ranges. Using reflectivity peaks in the red, green and blue ranges naturally leads to cyan, magenta and yellow subpixels. Stacking multiple such filters can produce native red, green and blue subpixels.

Note that given a bandwidth of $\Delta\lambda = \frac{4\lambda_0}{\pi}\arcsin\left(\frac{n_2-n_1}{n_2+n_1}\right)$ and alternating layers of silicon dioxide ($n \approx 1.5$) and silicon nitride ($n \approx 2.0$) bandstop filters with a bandwidth of $\Delta\lambda \approx 100\,\mathrm{nm}$ can be constructed. These can be matched nicely to the $300\,\mathrm{nm}$ range of human vision (see also figure 6.2).

The dissimilarity of the shape of the reflectivity curve to the absorption curves of the human visual pigments means that good results may only be obtained for larger numbers of subpixel types. Another tricky aspect of this technique is a rather severe shift in centre wavelength at non-normal incidence.

As seen before in figure 3.3, different colours of light produce different excess carrier profiles in a semiconductor. However, the resistor ring measurement schemes only provides some weighted integral over the curve, meaning that spectral information is convoluted with intensity. There is thus no obvious way to exploit the wavelength dependence while remaining sensitive to light intensity and direction in a single detector pixel.

Combining multiple subpixels opens up new options. For the aforementioned reasons, detector pixels with different dimensions will respond differently to different wavelengths; wider channels will, as it were, make better use of light with a long skin depth, while very narrow channels will waste a lot of it. This idea will be implemented in the detector designs.

3.6 Materials requirements

Several materials properties affect detector performance. When selecting the substrate to be used for detector fabrication, these should be kept in mind.

Properties such as crystal orientation directly set the range of possible designs. A device thus simply requires some specific value. This section instead discusses quantitative parameters that gradually improve or degrade device operation.

3.6.1 Parameters affecting signal quality

As discussed in chapter 3.1 signal strength in a photoconductor or -diode is directly proportional to minority carrier lifetime. Carrier lifetime is normally limited by crystal defects. This includes impurities - both unwanted and dopant - and the edges of the crystal. In addition, conductivity change in the photoconductive effect is inversely proportional to unperturbed carrier concentrations.

Both these arguments say that signal-to-noise ratio benefits from using materials as lightly doped as possible. In the intrinsic limit, carrier concentrations are on the order of $n = p = 10^{-10}\frac{1}{\mathrm{cm}^3}$, corresponding to a conductivity close to $\sigma = 3 \times 10^5\,/\Omega/\mathrm{per}/\mathrm{cm}$. Given time, the best contrast between light and dark measurements can be obtained here; every order-of-magnitude increase in conductivity leads to a comparable decrease in contrast.

When using lightly doped materials, a further performance boost can be attained by using FZ-grown rather than CZ-grown substrates.

Quantum efficiency is limited by the match between incident photon energy and bandgap energy. Leftover energy will not contribute to signal and by heating the detector increase noise levels. However, appreciable bandgap engineering requires careful materials selection and modification and is beyond the scope of this discussion.

3.6.2 Parameters affecting readout

It should be noted that the above discussion assumes unlimited measurement time budget. Thermal noise in a resistor produces a voltage error of magnitude $i_\mathrm{n} = \sqrt{\frac{4\,k_\mathrm{B} T\,\Delta f}{R}}$. Long measurement times allow a small bandwidth and thus signal error. For shorter measurement times, relative error scales with $\frac{i_\mathrm{n}}{i} \propto \sqrt{\frac{1}{R}}$. This leads to the question of whether larger or smaller resistances are better for detecting small signals. If the uncertainty in detecting a change in signal grows with the ratio between the signal and the change, we have measurement error $\Delta \propto R$ with thermal fluctuation $\frac{i_\mathrm{n}}{i} \propto \sqrt{\frac{1}{R}}$. This suggests that the large-resistance regime is best.

Source measurement units can reliably measure resistances up to $R = 1\,\mathrm{G\Omega}$. Higher values are also impractical because of the difficulty in preventing leakage paths of comparable resistance. Resistors near this limit require integration times on the order of microseconds to find a reliable value.

Capacitances in the system may require significant hold times before the steady state is reached. As discussed in chapter 3.2 ideal resistors have an intrinsic time constant of $RC = \frac{\varepsilon}{\sigma}$. For intrinsic silicon $\varepsilon = 1 \times 10^{-10}\,\frac{\mathrm{F}}{\mathrm{m}}$ and $RC = 3 \times 10^{-16}\,\mathrm{s}$. Other components in the setup, including cables and bond pads, may have capacitances many orders higher. This means that high resistances require more careful setup design; however, tricks exist to limit the effects of the setup on measurements.

An upper limit on material resistivity is thus posed by desired sampling frequencies, because of thermal noise, and by practical limits on measurable resistances.

AC measurement techniques are largely insensitive to low-frequency changes in system properties, such as heating effects. On a silicon-on-insulator wafer, where the device substrate lies atop an insulating layer binding it to a handle wafer that provides mechanical support, AC operation has the drawback of inducing capacitive coupling between the device and handle wafer.

In the equivalent circuit, the resistor leads both get a capacitor to separate nodes, which are in turn connected to one another and ground with separate resistors. The capacitance values can be estimated as that of the contact pads and leads and their equivalent across the insulator, on the order of $C = 1 \times 10^{-11}\,\mathrm{F}$. In situations where leakage through the oxide is significant, the most relevant current path is from one contact to the other, rather than through the handle wafer bulk to its ground connections. Its resistance will about an order of magnitude lower than the resistor to be measured times the ratio of their conductivities. At a ratio of $\frac{\sigma_\mathrm{h}}{\sigma_\mathrm{d}} = 10^3$, the impedance of the leakage path is practically equal to that of the capacitances.

The full interfering impedance reaches a magnitude of $Z = 100\,\mathrm{M\Omega}$ around $f = 100\,\mathrm{Hz}$, in the lower range of usable AC frequencies. Increasing the thickness of the buried oxide will shift this frequency up proportionally, decreasing leakage effects and allowing faster repetition. Alternatively decreasing handle conductivity limits the leakage currents that will flow regardless of frequency, proportionally diminishing leakage at all frequencies.

Fabricating ohmic metal-semiconductor contacts is generally easier on highly doped samples. However, local high doping or other techniques can be used to fabricate good contacts in any type of silicon.

3.6.3 Overall preferences

For two sets of wafers, where one is to be used for fabricating tetrahedron-based and the other for pit-based sensors, we can summarise our preferences as follows.

Device layer

Critical

- <111> crystal face for tetrahedron-based sensors; <100> for pit-based
- High-ohmic; optimal doping range approx. $10^{12} - 10^{14}\,\mathrm{cm}^{-3}$.
- FZ-grown

Preferable

- Thickness $5 - 20\,\mu\mathrm{m}$
- Well-defined doping;
- Minimal thickness variation;
- (Light) p-doping;

Oxide layer

Preferable

- Thick; decreases interference in AC measurements
- Well-defined geometry (thickness, surface curvature..)

Handle wafer

Preferable

- High-ohmic; decreases interference in AC measurements.

General

Preferable

- <111> and <100> properties as similar as possible. Doping identical, <100> thickness similar or smaller,

3.6.4 Acquired wafers

A set of wafers has been acquired that should satisfy the requirements outlined here. Their listed properties are indicated here.

Device layer

- <111> crystal face for tetrahedron-based sensors; <100> for pit-based
- High-ohmic at $1/\sigma = 1000 - 6000\Omega\,\mathrm{m}$.
- FZ-grown
- Thickness $10\,\mu\mathrm{m}$
- p-doped;

Oxide layer

- Thickness $1\,\mu\mathrm{m}$

Handle wafer

- High-ohmic at $1/\sigma = 1000 - 6000\Omega\,\mathrm{m}$.

General

- <111> and <100> properties within identical ranges.

These properties satisfy the set requirements.

3.7 Discussion

The general behaviour of excess carriers in resistors was studied and applied to the designed devices. A quantitative model is found for the pit-based detector. This model does assume a one-dimensional excess carrier concentration distribution in the resistors. Based on the known high surface lifetime of thermal oxide on silicon, this approximation does seem reasonable.

For the behaviour of a three-dimensional resistor under illumination, Green's function analysis does not allow an analytic solution. A simplified model is designed and shows very interesting first results on a one-dimensional problem. It accurately estimates the position and gets the value of the peak concentration within a factor of two. Before it can be applied to tetrahedra, further improvement is needed on its behaviour away from the peak. The tetrahedron-based detectors thus need to be calibrated experimentally.

It would be interesting to modify the approximate model to a more accurate tool for three-dimensional diffusion analysis. The model currently shows concentration gradients that are too large to satisfy the diffusion equation in the bulk of the resistor. Correcting this would already improve the model significantly.

Colour sensitivity is predicted in combinations of devices of different dimensions. No quantitative model is found here. The qualitative arguments revolve around the differences between the curves in figure 3.3. These arguments do give credence to the idea that colour may be resolved.

The desired materials properties were analysed and the conclusions used in an order of new wafers. Some notes may be placed at the analysis of noise performance. Practical considerations, such as maximum allowable averaging times or fixed noise sources elsewhere in the system, may affect the balance between the measured signal and noise. This may challenge the conclusion that minimal doping is preferable.

Chapter 4

Materials properties validation

The detector designs and theoretical models make several assumptions about properties of used materials and process parameters. In order to verify these properties, a series of materials testing samples is designed.

From the wafer vendor, we expect a device layer of thickness $h = 10\,\mu\mathrm{m}$ and a conductivity of $1/\sigma = (35 \pm 25)\Omega\,\mathrm{m}$.

4.1 Sample design

To find the resistivity of the wafer device layers, resistors of well-defined geometry need to be fabricated. In order to quantify the photoconductive effect, some of these resistors need to be bare to an external light source. For the aluminium-silicon contact behaviour to be analysed, we need to be able to take both four- and two-point measurements on the same device.

The fabrication scheme is based on the available SoI wafers and needs to deposit aluminium where required and to remove silicon elsewhere. This two-mask process is shown schematically in figure 4.1, starting from the bare wafer in figure 4.1a. One micrometre of silicon-infused aluminium - as discussed in chapter 2 - is sputtered onto the silicon device layer. The aluminium is then patterned using standard negative resist lithography and an isotropic wet etchant, figure 4.1b. The silicon is then patterned using a deep reactive ion etch, using sulfur hexafluoride as etchant and perfluorocarbon as passivator, with again photoresist as etch mask. This results in electrical islands, figure 4.1c. The result is cleaned and annealed at $T = 450\,^{\circ}\mathrm{C}$ in water vapour to improve the silicon-aluminium contact.

Care is taken not to contaminate the high-ohmic silicon with unintended dopants. To this end, the process is run entirely within the CMOS-compatible ultraclean line that is not used for metals other than aluminium and tungsten.

Several types of resistors are designed, two of which are shown in figure 4.2. Each type is fully usable for two- and four-point resistance measurements with or without external light source. Large pads are available for contacting with external probes.

The resistors are not perfect rectangular resistors in that currents are supplied from the top. Near the contacts the currents are not expected to be nice and uniform along the resistor axis. For this reason the contacts are spaced a minimum of $d = 50\,\mu\mathrm{m}$ apart, which with a device silicon thickness of $h = 10\,\mu\mathrm{m}$ should mean that most of the resistor is relatively far away from the contacts.

For light-based measurements, it is important to note that the contact leads block light from entering the material. Since the smaller leads are of length comparable to the diffusion length of carriers in silicon, this leads to a somewhat non-uniform conductivity pattern. The magnitude of the photoconductive effect will thus be underestimated somewhat.

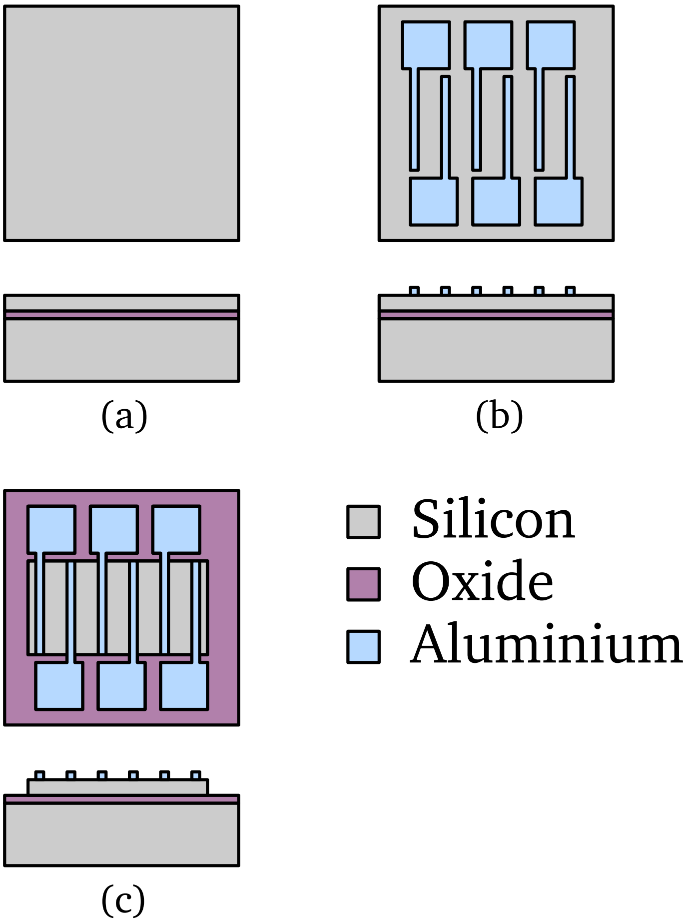

Figure 4.1: Fabrication process for the materials testing samples. Top views and cross-sections are shown. Silicon is shown in grey, oxide in violet and aluminium in blue.

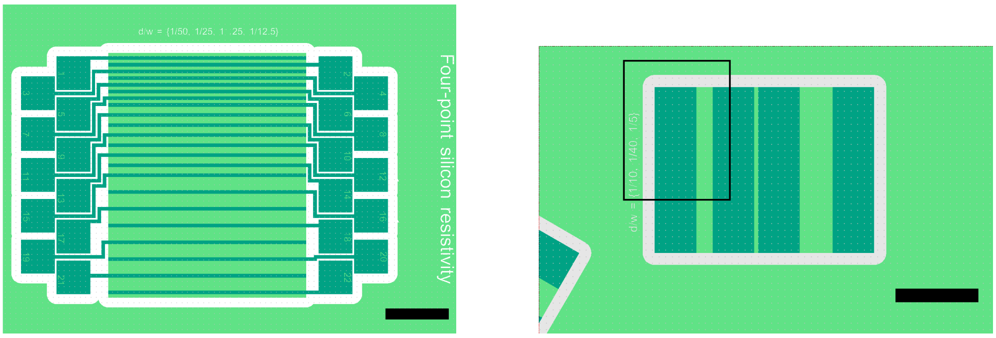

(a) (b)

Figure 4.2: Top view of two resistor designs featured on the materials testing wafers. Aluminium is deposited on the dark area; the white area is etched down to the buried oxide. The devices are quite large; both scalebars are of length $L = 1\,\mathrm{mm}$.

4.2 Fabrication

All wafers were processed in the MESA+ cleanroom. Optical inspection shows a good match between the designed and realised resistors. An example of the type of resistor from figure 4.2b is shown in figure 4.3. It is clear that the aluminium has been removed from all places where it was to be removed and that the silicon was etched down to the oxide. Other metrology techniques, including surface profiling, confirm the quality of the steps. The results appear quite uniform around the wafer.

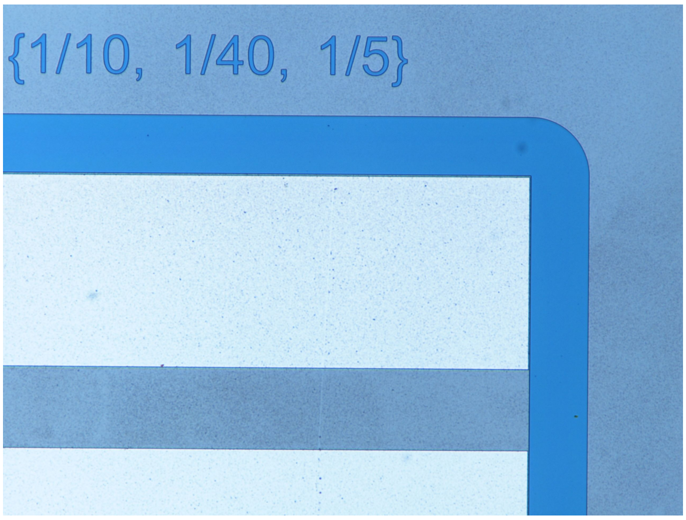

Figure 4.3: Optical overhead view of the area within the black rectangle on one of the resistors from figure 4.2b. The lightest material is aluminium, the darker blue buried oxide. The gray material is bare silicon.

Figure 4.4 shows one of the marks used for aligning the second mask to the results of the first. The alignment error in either direction is below $\Delta x = 1.3\,\mu\mathrm{m}$. Since this has been realised reliably over several iterations of the process, we conclude that a two micron margin in mask designs should be plenty to account for any alignment errors.

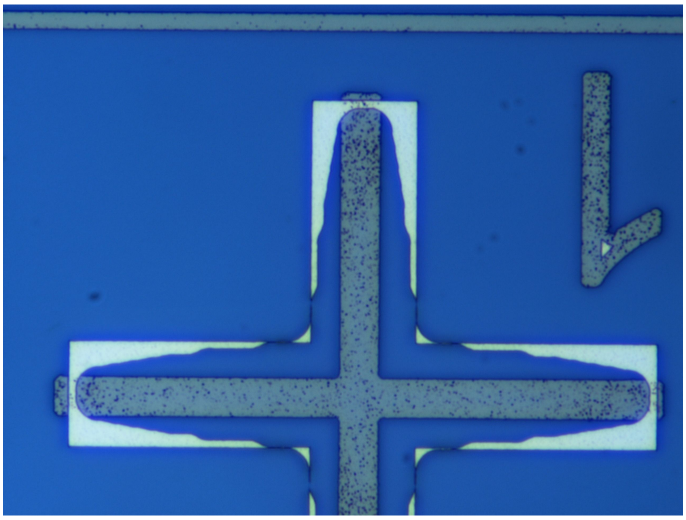

Figure 4.4: An alignment mark as seen optically on a fully processed wafer. The open cross is $200\,\mu\mathrm{m}$ wide. The horizontal alignment error can be read to be slightly less than $\Delta x = 1.3\,\mu\mathrm{m}$. The vertical error is a bit smaller still.

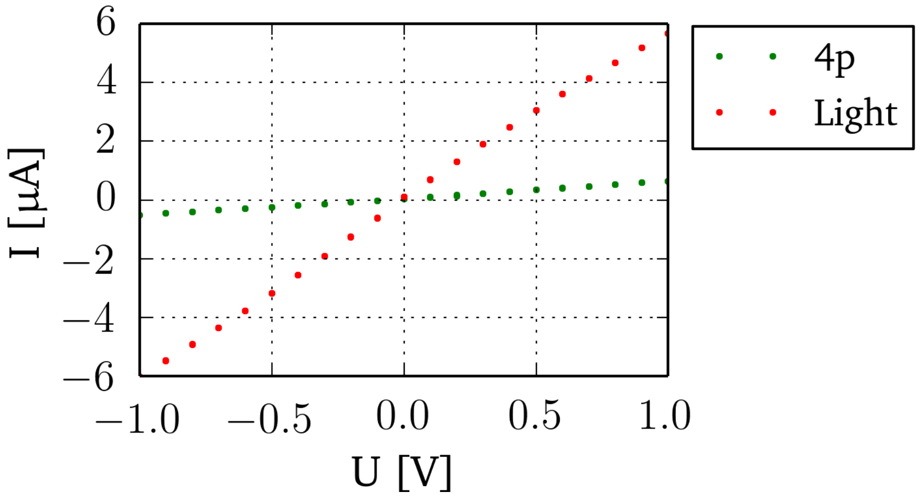

Figure 4.5: Sample IV curves for one of the fabricated resistors. The green points were taken in the dark; the red LED was switched on for the red points. We see nice linear behaviour and much higher currents when the light is on.

4.3 Experimental results

The resistors were connected with external probes to a Keithley 2602 Source Measurement Unit. The source and sense paths were connected to the aluminium with separate probes, eliminating the probe-aluminium contact from measurement results whether the measurements used two contact leads or four.

For the light-based measurements, a LEDENGIN LZC-83MC00 RGB LED die was mounted $r = 30\,\mathrm{cm}$ above the sample. Its red emitters were run at their design current of $I = 700\,\mathrm{mA}$. Using a Hagner universal photometer a radiant flux of $L = 110\,\frac{\mathrm{W}}{\mathrm{m}^2}$ was found at the sample position.

A series of resistors of the variety in figure 4.3 was studied. These resistors are located on one of several lines from the centre of the wafer out. IV curves are taken on each of these resistors with and without LED lighting. An example is shown in figure 4.5. It demonstrates very nicely linear behaviour.

Measurement results of a set of these resistors are shown in figure 4.6. We see that the light source strongly affects the observed resistance. From the lack of hysteresis in the individual IV-curves thermal explanations were excluded, so that we may conclude that the photoconductive effect is responsible for this huge change.

The strong increase in resistance near the wafer edge is yet unexplained. No comparable change in wafer thickness is found. As the anomaly is seen in four-point measurements of the dark resistance, it would appear that doping is much weaker near the edges of the wafer.

Otherwise, the resistors still show a variation of a factor of two in their dark resistance value. No clear explanation is available here either. It is unlikely that contacts have a sufficiently high resistance to contribute, especially given how nice and straight the individual lines are. Wafer thickness has been checked to vary by no more than a few percents. Inhomogeneity in the substrate or probe shadowing artefacts conductivity are the clearest candidates.

Considering the data from $r = 34\,\mathrm{mm}$ and closer to the wafer centre, we find a resistance average of $R = 0.47 \pm 0.09\,\mathrm{M\Omega}$. With the known dimensions of the resistor, this translates to $1/\sigma = 188 \pm 36\,\Omega\mathrm{m}$ or $\sigma = (5.5 \pm 1.0) \times 10^{-3}\frac{1}{\Omega\,\mathrm{m}}$. This compares with an expected $1/\sigma_\mathrm{e} = 35 \pm 25\,\Omega\mathrm{m}$.

The average conductivity shift is found to be $\Delta\sigma = (46.8 \pm 3.7) \times 10^{-3}\frac{1}{\Omega\,\mathrm{m}}$. From the theory in chapter 3 and the one dimensional resistor approximation, we find an excess carrier concentration of around $c = 6.3 \times 10^{18}\,\frac{1}{\mathrm{m}^3}$. This corresponds to a lifetime close to $\tau = 2.0\,\mathrm{\mu s}$, well within

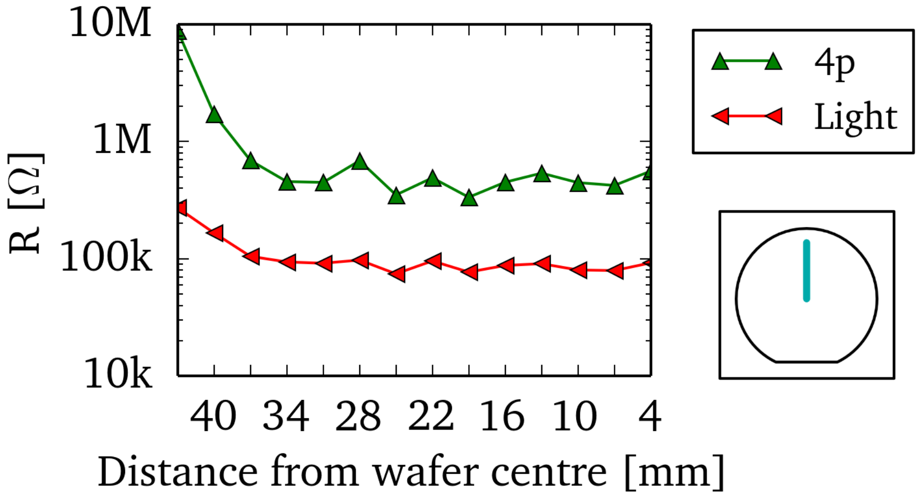

Figure 4.6: Resistance values for a series of nominally identical resistors of the type shown in figure 4.3 with and without red LED lighting. The photoconductive effect is clearly visible in the results. Interestingly, the resistance values themselves vary quite a bit.

reasonable range.

On a different wafer, all resistors of the same type were studied with two- and four-point measurements. Given the tiny resistance of the connecting wires, we expect that the only difference between these two measurements is given by the aluminium-silicon contact resistance.

The relative differences between each pair of two measurements are reflected in figure 4.7. The first bar represents a deviation of less than 2% in resistance and contains about 70% of resistors. These results imply that aluminium-silicon contact resistance will not be an issue in operating further devices.

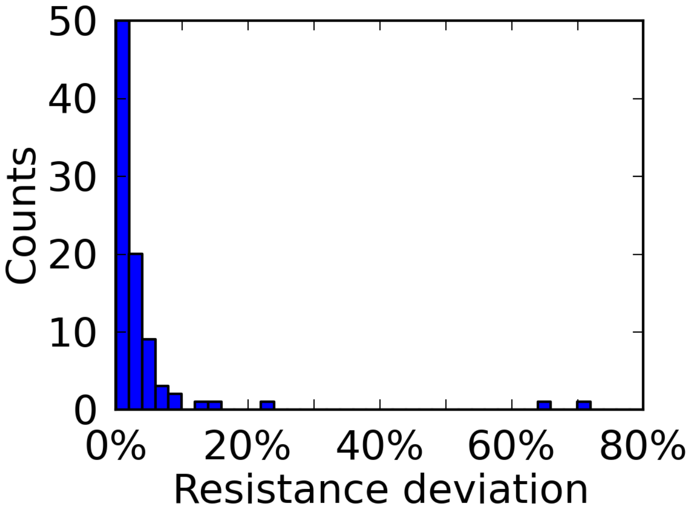

Figure 4.7: Histogram comparing two- and four-point measurements on all 70 resistors of one kind on a wafer. Each bar represents the number of resistors within a 2% relative deviation range.

4.4 Discussion

The fabrication process is seen to produce the desired structure to within a spatial error of $\Delta x = 2\,\mu\mathrm{m}$ in the in-plane features and with the expected profile in height.

The photoconductive effect is very strong

The measured IV curves are linear. The difference between two- and four-point measurements has a spread of less than 2%. This suggests that contacts show Ohmic behaviour. The employed aluminium deposition and annealing technique thus appears very effective for making good contacts on lightly doped silicon.

Different resistors on the wafer show very different resistances, up to a factor 30 apart, with outliers concentrated near the wafer edge. It is not clear what causes there variations. It may be that doping near the wafer edge is much lower than elsewhere. In addition, the observed resistance of $1/\sigma = 188 \pm 36\,\Omega\mathrm{m}$ deviates significantly from the expected $1/\sigma_\mathrm{e} = 35 \pm 25\,\Omega\mathrm{m}$. Nevertheless, the devices behave well and either value is suitable for photoconductive device characterisation.

Overall, these results confirm the viability of making photoconductive light direction sensors using silicon-infused aluminium on the newly acquired silicon.

Chapter 5

Detector realisation

The design for the pit-based detector outlined in chapter 2 were specified further and converted to process flows with ample support from the MESA+ cleanroom staff and lessons from several dummy runs. Designs were fabricated as per these flows.

5.1 Design specification

The general design in chapter 2 leaves several variables undefined, most notably the various relevant dimensions. As sketched in figure 5.1, four length scales are important for the functioning of the device, in addition to oxide thicknesses. The silicon device layer has a thickness h, the outside edges of the pit give length L and the channel has a width w at the top. In addition, the contacts reach into the pit over a certain distance c.

Silicon device layer thickness h is a fixed wafer property, although it may vary somewhat from spot to spot on one wafer. This means that all devices on a wafer will in principle have comparable h, although different wafers can be used to obtain different devices. Because the slope of a TMAH-etched <111> plane is fixed, the thickness h immediately sets a minimum size for the pit where opposing faces do not touch. The available wafers have $h = 10\,\mu\mathrm{m}$, which corresponds to a pit size $L > 14.1\,\mu\mathrm{m}$. This is comparable to commercial camera pixels. Apart from this limit, L may be set freely. In applications, smaller pixels lead to higher spatial resolution, but larger pixels are less sensitive to fabrication flaws. For this reason we design pixels of both $L = 16.0\,\mu\mathrm{m}$ and $L = 40.0\,\mu\mathrm{m}$.

As noted in chapter 3.5, channels of different width will respond differently to light of different wavelength. Any two differently sized channels may thus be used to distinguish two wavelengths, although a significant size difference with respect to skin depth will make the effect much more visible. For the $L = 16.0\,\mu\mathrm{m}$ pits we use $w = 0, 4$ and $8\,\mu\mathrm{m}$. For the $L = 40.0\,\mu\mathrm{m}$ pits, $w = 0, 2$ and $-2\,\mu\mathrm{m}$. The negative number means that the channel will actually be lower than h. The larger channels are expected to be more robust in fabrication and lithography, which may be especially relevant for the smaller devices, which are likely to be at the limits of available technology. Smaller channels are expected to be more sensitive to colour.

The contact overlap need be large enough to make good contact, but not so large that a large portion of the light reaching the pit is reflected. We select $c = 4.0\,\mu\mathrm{m}$ for the $L = 16.0\,\mu\mathrm{m}$ pits and $c = 7.0\,\mu\mathrm{m}$ for the $L = 40.0\,\mu\mathrm{m}$ pits. Overlap $c = 7.0\,\mu\mathrm{m}$ has the advantage that the entire slope is contacted and that overetch will be less noticeable, but $c = 7.0\,\mu\mathrm{m}$ would leave only $d = 2.0\,\mu\mathrm{m}$ of channel open to light on the $L = 16.0\,\mu\mathrm{m}$ devices, prompting smaller contacts in exchange for a larger signal.

Based on the materials testing samples we also define some tolerances for any mask designs. Alignment may be off by up to $\Delta x = 2.0\,\mu\mathrm{m}$, so insulated parts must be at least this far apart. The aluminium may overetch up to a micrometre, so aluminium strips should be at least $b = 2.0\,\mu\mathrm{m}$ wide.

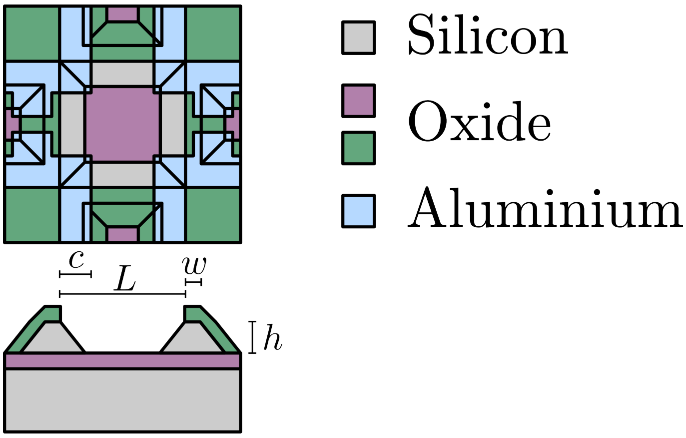

Figure 5.1: Schematic cross-section of the channel of a pit-based detector, showing the length scales important in its functioning. We have silicon thickness h, pit size L, channel top width w and contact-pit overlap c. Not considered here are oxide thicknesses.

Incorporating all these design choices and rules, we can now define the precise layout of the structures, as seen in 5.2. This also shows how the current contacts are implemented as arrays of small squares, to maximise contact area.

5.2 Process outline

An overview of the basic process for pit-based detector fabrication is shown in figure 5.3. The process is designed to produce detectors according to the original design as simply as possible, resulting in a process that requires three distinct patterning steps, implemented in three photomasks.

A thermal oxide is grown on one of the <100> SOI wafers. Lithography is used to pattern a photoresist that then acts as a mask for a BHF oxide etch. The photoresist is removed and the exposed silicon is etched down with TMAH. This step produces the electrical islands required for device operation and in addition already creates the outer walls of the current channels.

The oxide is removed and a new thermal oxide grown to cover all the exposed silicon. This oxide is patterned much like its predecessor and the silicon is etched down to produce the central pit and current contacts.

Care is taken to remove the native oxide on the exposed silicon before depositing a layer of aluminium on the wafer. Lithography is performed on the aluminium layer and the aluminium is patterned with a wet isotropic etch.

Finally, the wafer is annealed at $T = 450\,^{\circ}\mathrm{C}$ in water vapour. This serves to improve the silicon-aluminium contact interface and thus decrease electronic barriers.

High-ohmic silicon, particularly at high temperatures, is vulnerable to the introduction of contaminants as donors. To help prevent this, the process uses the CMOS-compatible ultraclean versions of steps wherever possible. For example, the standard step of hot nitric acid cleaning is replaced with an ozone and water steam cleaning. The ovens have not been in contact with metals other than aluminium and tungsten.

Several other steps cannot follow standard procedure directly and will be discussed here.

5.2.1 Thermal oxide

Thermal oxide growth is done in an oven using a dry growth process. Although slower, oxide growth without water vapour is claimed to give better results.

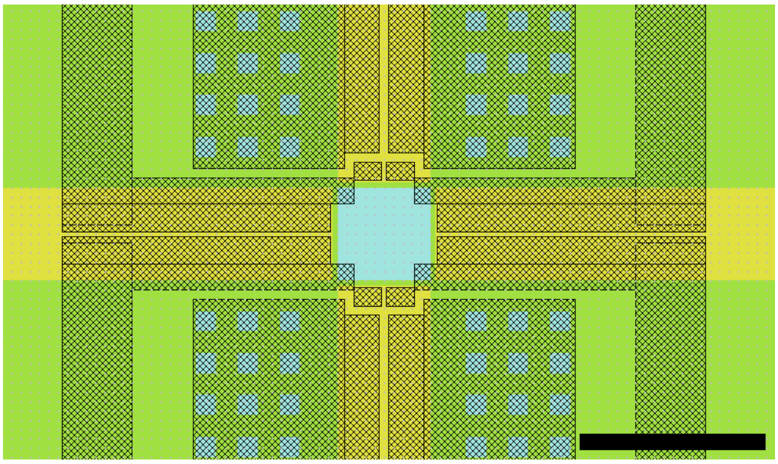

Figure 5.2: One pit-based detector adhering to the design rules. Yellow indicates formerly buried oxide, green thermal oxide on silicon, blue bare silicon and the netted structure shows the contact layout. Outside the pit mirroring on the outside faces of the detector can be seen as well as four arrays of current contacts. This particular device has $L = 40\,\mu\mathrm{m}$, $w = 2\,\mu\mathrm{m}$ and $c = 7\,\mu\mathrm{m}$; the bottom-right scalebar is $100\,\mu\mathrm{m}$ long.

In the oxide growth steps, oxygen is introduced to the $T = 950\,^\circ\mathrm{C}$ oven for six hours. The resulting layer has thickness $d = 108\,\mathrm{nm}$ and refractive index $n = 1.44$, as predicted from calibration measurements and checked on one of the wafers by ellipsometry.

This thickness is more than enough for electrical insulation and masking against the TMAH etch, without eating away too much of the silicon.

5.2.2 Lithography

The standard lithography process employed in the MESA+ cleanroom uses a positive photoresist that is spun to a layer of thickness $d = 1.7\,\mu\mathrm{m}$. This works well for the first lithography step, but after etching the silicon, the height differences are too large for this resist to overcome; a maximum step height of $h = 5.0\,\mu\mathrm{m}$ is quoted.

Resist may instead be sprayed onto the wafer. For this, the wafer is heated slightly to improve adhesion and a thicker resist is sprayed. A nominally uniform $d = 5.0\,\mu\mathrm{m}$ layer is thus deposited.

This method was tested. Although the resist layer itself appeared very nice and with appropriate exposure developed well, the results of the subsequent oxide etch were poor. As seen in figure 5.4, the etch has been washed out severely, exposing most of the silicon near the pits and disturbing the current contacts. From this result, it seems very likely that the resist is somewhat permeable to the fluoric acid-based etchant used, with the possibility of poor adhesion contributing to the washout.

Without an obvious way to solve this, we return to spin coating. The thickest resist available is made for layers of $d = 7.0\,\mu\mathrm{m}$. This produces very nice results, as seen in figure 5.5. Both the pit and the current contacts are well-defined.

Two other things may be noted. The alignment error is close to $\Delta x = 1.5\,\mu\mathrm{m}$, slightly larger values than with the materials testing sample. In addition, all corners are rounded with a radius of curvature around $r = 2.0\,\mu\mathrm{m}$. This is an artefact introduced by lithography, possibly related to the thickness of the resist layer to be exposed. The TMAH should still neatly etch a square hole, as it is solely limited by the underlying crystal. This will, however, result in some overhanging oxide, by up to $r = 0.5\,\mu\mathrm{m}$ in the corner. Given the tolerances in the system this should not be problematic.

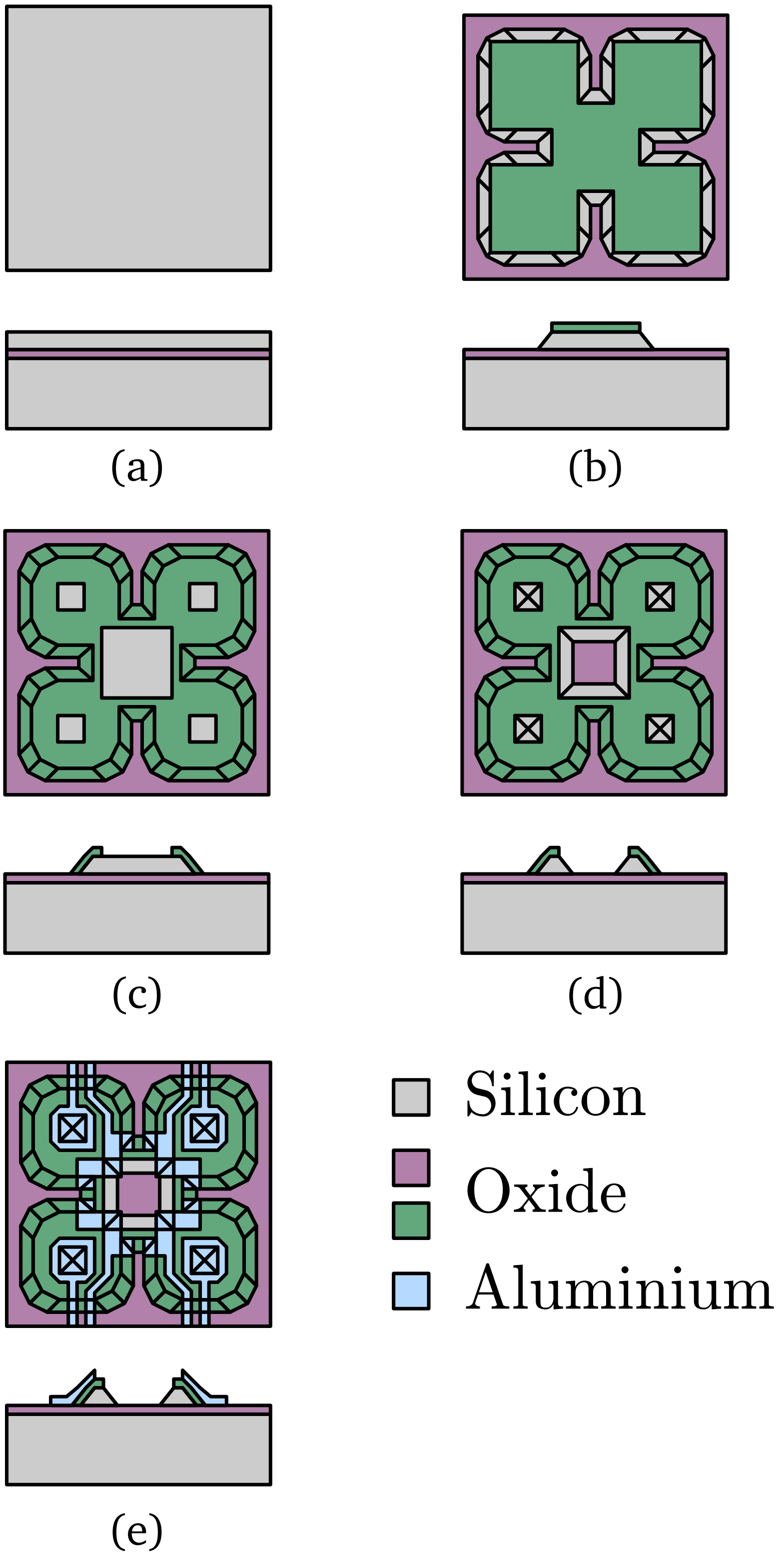

Figure 5.3: Schematic overview of the basic process for pit-based detector fabrication. A SOI wafer (top left) is subjected to a thermal oxide growth. This oxide is patterned and used as a mask for a TMAH etch (top right). The oxide is removed and a new oxide is grown. This oxide is patterned with a second mask (centre left). The subsequent TMAH etch opens up the central pit and the current contacts (centre right). Aluminium is then sputtered onto the sample and patterned, resulting in the desired structure (bottom left).

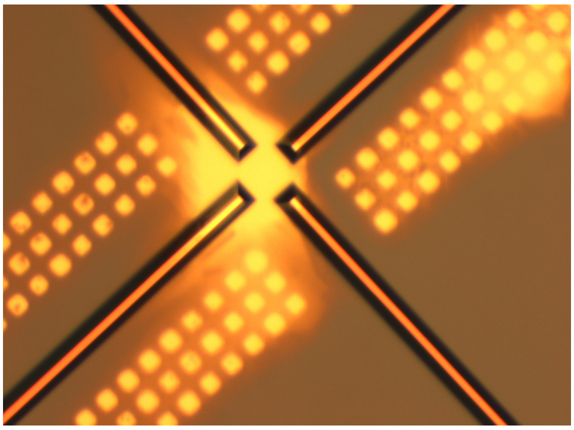

Figure 5.4: Spray coated resist did not perform well for oxide patterning. This image shows the result of the oxide etch that was to define the central pit and four regular arrays of current contacts. The thermal oxide far from the features (brown) looks fine, but especially around the central a severe washout is observed, exposing silicon (yellow) where oxide should remain. It is very likely that the sprayed resist is permeable to the fluorine-based etchant used.

5.2.3 Aluminium deposition

The preferred CMOS-compatible method of depositing silicon-infused aluminium is sputtering in a dedicated machine. However, the resident ultraclean sputterer went unavailable during device fabrication and an alternative had to be found.

A layer thickness of at least several hundred nanometres is desired to keep the relatively long contact leads of manageable resistance and to make sure the lead properly passes the step where the oxide meets the silicon slope. This leaves sputtering and evaporation as the most suited options. An electron beam evaporator was found to be usable.

Without the sputterer however, no silicon-infused aluminium could be acquired. Pure aluminium was selected as the next best thing. No sources have been able to quantify the length scales where junction spiking becomes relevant, but mention is made of ‘thin junctions’. [13] We opt to try the method, keeping in mind that if extensive damage to the exposed silicon is observed, the aluminium is likely to be to blame.

5.3 Results

Devices were fabricated according to the process flow, with optical checks at several points. The oxide growth and TMAH etching steps perform as expected, with the previously mentioned comments. The aluminium etch, however, consistently performs poorly. A scanning electron microscope (SEM) image of the resulting device is shown in figure 5.6.

Looking at this image, we directly recognise the pit in the centre and the trenches in four directions. We see the current contacts coming in from the top and the voltage contacts towards the left and right.

Several errors are clear in the aluminium pattern. No aluminium can be spotted within the pit. On none of the ridges mirrors can be seen. The voltage leads have retracted far away from the ridges and it is not clear that the two on the right are separated in the middle of the trench.

This leaves devices with much poorer directionality that can only be used in two-point measurement mode through the current contacts.

Figure 5.7 shows a close-up view of a better-looking device. Here, part of the mirrors on the left and right remains. It is also clear that no proper contact is made between the voltage contact leads and the exposed silicon on the slopes of the pit.

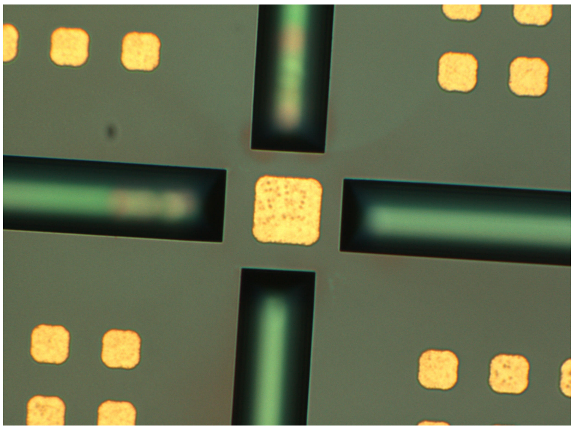

Figure 5.5: A successfully patterned oxide, using thick spun resist as a mask. The central pit is clearly outlined in silicon (yellow) on the oxide (grey). One may also note that alignment is off by about $\Delta x = 1.5\,\mu\mathrm{m}$ and that corners are rounded.

Several attempts with different aluminium etch times or photoresist exposure times have proven fruitless. It is not immediately clear why the etch does not perform as expected.

One may note however that most of the irregularities arise with aluminium on the slopes. It is possible that despite a standardised lithography process, the photoresist flows into the pit somewhat, leaving near the top of the ridges a thinner layer that may not make it through development intact. Likewise, the trouble in separating the voltage contacts down in the trench could be due to the thicker resist layer there.

However, testing these hypotheses, let alone solving them, is no longer feasible within the timeframe of this project.

In the light of these results, one wafer was salvaged for separate repair work. It was treated with a focussed ion beam installation by L.A. Woldering and H.A.G.M. van Wolferen. In this process, one pit sensor was selected for recovery. The poorly etched aluminium regions were milled down to ensure the removal of any conductive material. Subsequently thin strips of tungsten were deposited between the remainders of the voltage contact leads and the corners of the pit.

SEM and optical inspection suggest a very successful operation. Nevertheless, one of the contact pairs still shorts out under electrical testing. Both adjacent contact pairs act as diodes away from the short. It is unclear how this situation arose.

All in all, ten out of fifty-four pit-based devices on one successfully fabricated wafer have separated voltage contacts. None of these appear to have voltage leads running into the pits.

The tetrahedron fabrication process was performed elsewhere in the group. However, due to unforeseen processing issues and time constraints no tetrahedra were produced up to the contact deposition stage.

5.4 Discussion

The process flow developed here was successful in producing the three-dimensional structure of the pit-based pixels. The patterned contacts do not look as expected. The voltage contacts do not reach the pits. However, the subset of devices where voltage contacts have separated can still be used with two-point measurements through the current contacts. This subset of devices does not retain backside mirroring. Instead, distinguishing positive and negative angles will have to be done through the difference in optical behaviour between the bare silicon surface and the oxide-coated surface on each channel. This difference will be smaller than the ideal design. The devices are thus suited for proof-of-concept test measurements.

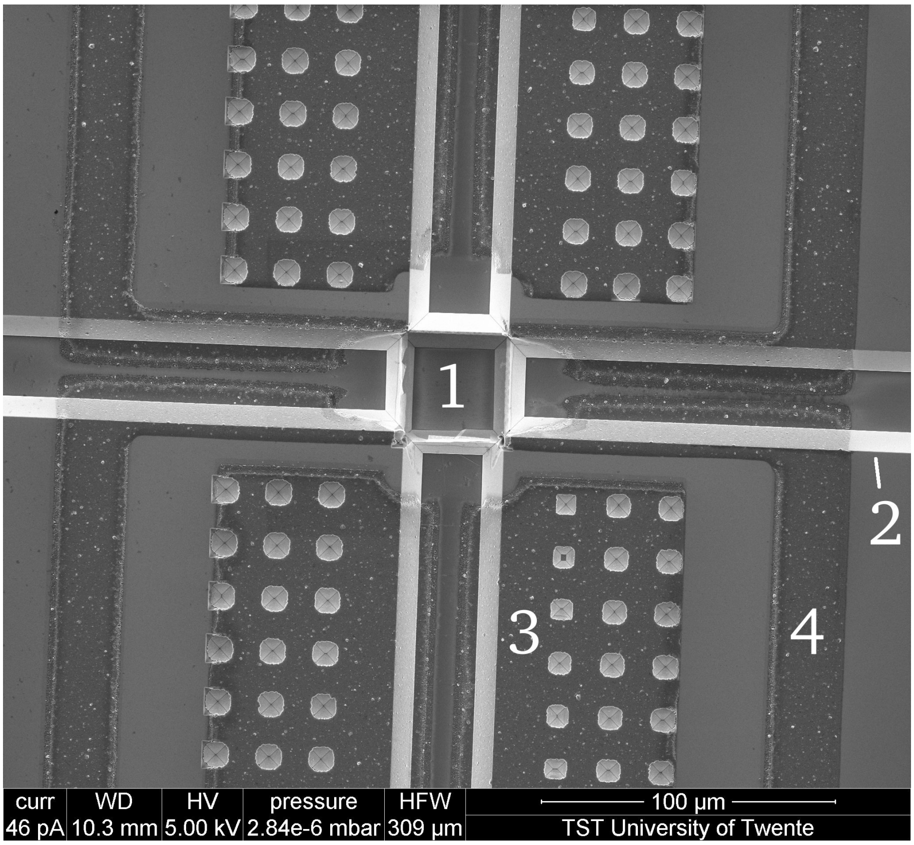

Figure 5.6: Scanning electron microscope image of a fully fabricated detector. This device has the same design dimensions as the one in figure 5.2. We see the pit in the centre (1), the TMAH planes away from it (2), arrays of current contacts on the top and bottom (3) and voltage contacts coming in from the left and right (4). We also see, however, that the mirroring on the slopes has disappeared entirely. It is not clear whether the right-side voltage leads are separated or not.

Before moving these detectors to applications, the contact patterning behaviour will have to be resolved. This will likely require a good bit of experimenation. If the hypothesis of lithography reflow is correct, one may consider using a different type of photoresist. It is conceivable that a spray resist may work well with the aluminium etch.

Alternatively, one may redesign the detector contact layout. There are also other reasons to do this. By designing a mask to move the boundaries of the aluminium-coated regions away from the slopes, they will be much less vulnerable to processing errors. This could also help move the mirror gaps towards places where they cannot possibly interfere with device function.

It is also interesting that the whole device may be realised with only one TMAH step. If the pit is etched together with the island at the very start of the process, a separate oxide etching step may be used to specifically open up the pit. Alternatively, the pit may be left coated in oxide entirely, moving the contacts towards spots slightly outside the pit, so that they, too, will be on a horizontal plane.

For applications the current contact layout is frustrating because pixels need to be very far away from their neighbours because of all the contact leads. This requirement can be negated by used silicon-through vias to locations below the detector, where plenty of space is available in three dimensions.

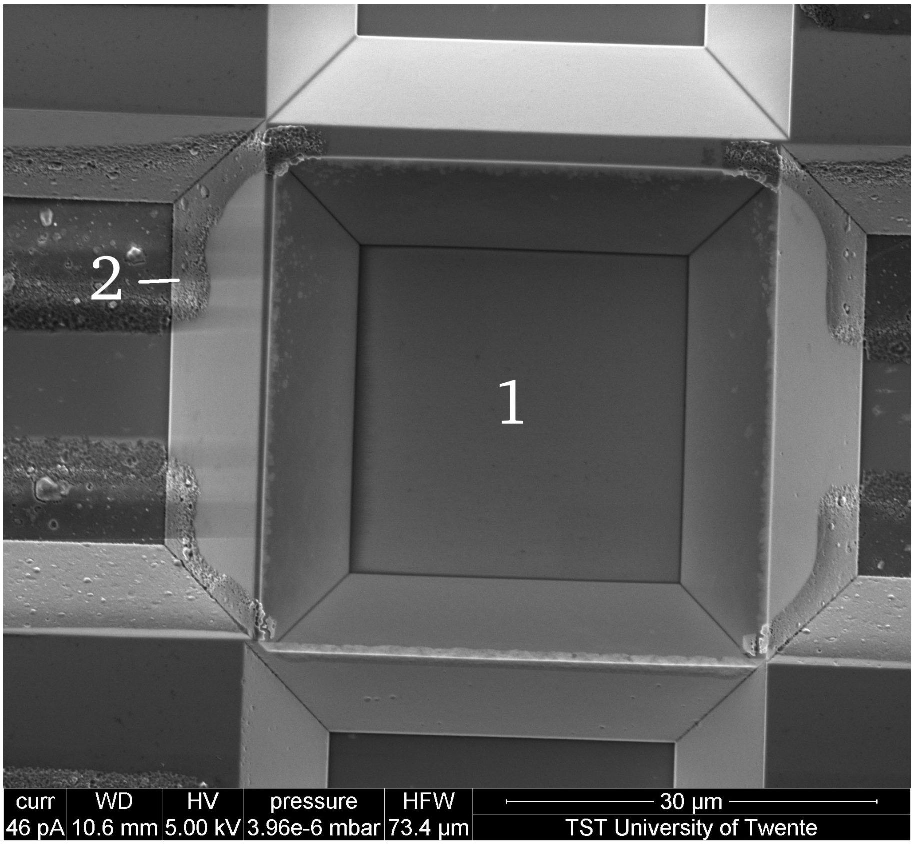

Figure 5.7: Close-up view of the pit (1) of another detector. Some of the mirroring on the left and right side remains (2), but the silicon of the slopes around the pit does not appear to be contacted by leads of any significance. This device has parameters $L = 40\,\mu\mathrm{m}$, $w = -2\,\mu\mathrm{m}$ and $c = 7\,\mu\mathrm{m}$.

Chapter 6

Light direction sensing setup

As we aim to characterise the full radiance vector $\mathbf{L}(x, y)$, including spectral information, we need to be able to apply a particular incident vector to the sample. We are then interested in characterising the full three- or four-resistor network.

6.1 Light source

An experimental setup is constructed to satisfy these needs. A schematic overview is shown in figure 6.1.

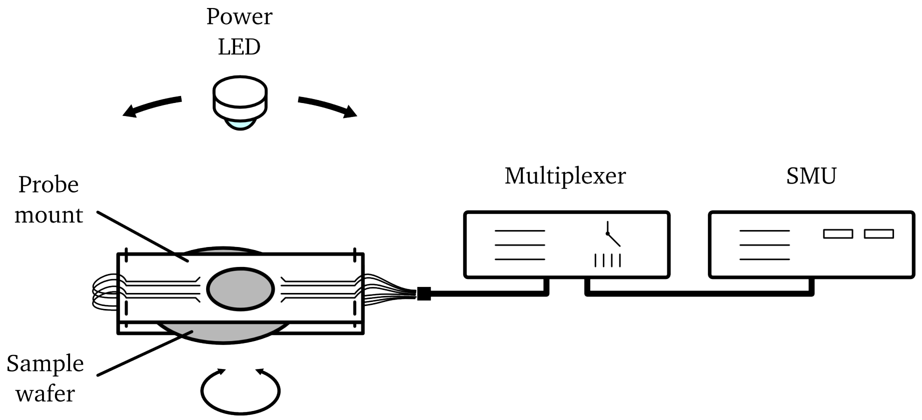

Figure 6.1: Schematic overview of the setup used for light direction sensing experiments. A full wafer with devices is put in the sample holder and one device is aligned with the probes mounted on the holder. The light source is installed directly over a large aperture in the sample holder and may rotate away from the normal around the sample holder centrepoint. The sample holder itself can rotate in plane. Eight wires connect four sets of probes to a multiplexer that allows the source measurement unit to measure the IV-curve on any pair of nodes.

A LEDENGIN LZC-83MC00 RGB LED die is used as a light source. It consists of three sets of four LEDs integrated on a single die, so that the die may emit any combination of red, green and blue light with appropriate modulation.

The spectral output of the light sources was measured and is shown in figure 6.2. Also shown is the skin depth of light in silicon, as discussed in appendix B. The spectra peak relatively sharply compared to both their separation and the rate of change of the skin depth. From the half maximum to the peak wavelengths variations of between 20% and 6% in skin depth are seen. From these data we may conclude that the peaks are sufficiently sharp to be modelled using a single skin depth.

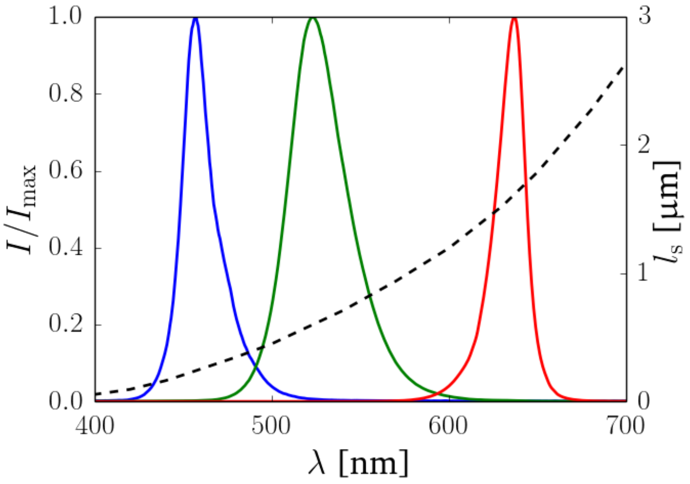

Figure 6.2: Measured emission spectra of blue, green and red LED light sources are shown against the skin depth of light in silicon as found in [12]. Each curve is normalised to its own maximum.

The LED is mounted on a large passive heat sink on an arm, close to $r = 30\,\mathrm{cm}$ away from its point of rotation. The arm allows a $\theta \approx 80°$ rotation away from normal in either direction. Positioning can be done by eye using the integrated goniometer. This position is accurate within $\Delta\theta = \pm 2°$.

The light source is used at its design operating current of $I = 700\,\mathrm{mA}$. The radiant flux at the sample position, as calculated from luminous flux measured with a Hagner universal photometer, is $L = 110\,\frac{\mathrm{W}}{\mathrm{m}^2}$ for red, $L = 61\,\frac{\mathrm{W}}{\mathrm{m}^2}$ for green and $L = 257\,\frac{\mathrm{W}}{\mathrm{m}^2}$ for blue.

6.2 Sample holder & probe mount

The sample wafer is clamped in a sample holder. Two sets of four probes are integrated into this holder. The sample holder and device contact layout are designed such that when the probes are properly aligned with the pads, the device under measurement is centred out under the light source.

An aperture in the sample holder allows light to reach the device. This aperture is intentionally large to prevent shadowing; the probes are $d = 25\,\mathrm{mm}$ apart and the aperture itself is about a millimetre smaller. Considering also the height of the probes, the maximum zenith angle with respect to normal is somewhere close to $\theta \approx 60°$.

The sample holder itself can rotate in-plane, around the device under test centrepoint. In this way, azimuthal angle ϕ can be arbitrarily set.

The probes themselves are spring-loaded golden beads that are pressed into the device contact pads. Although this method of contacting might be hindered by the native oxide that grows on the aluminium contact pads, no such effect was observed in a quick test. Nevertheless, separate source and sense paths into and out of the device aluminium were used in all cases to eliminate the gold-aluminium interface from measured results.

The fabricated devices lacked proper voltage contacts. In order to still be able to use the probe mount to exclude the gold-aluminium interface from measurement, a wire bonder was used to stitch the voltage and current contact pads together with aluminium wires for these devices. An example is shown in figure 6.3.

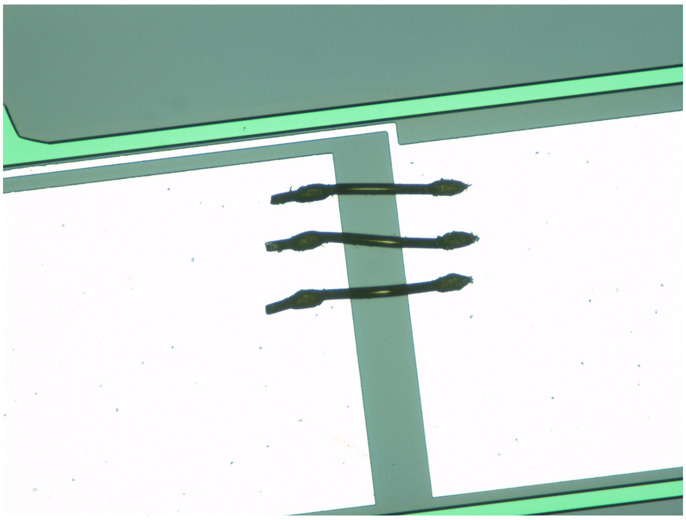

Figure 6.3: In order to use the probe mount with devices without functioning voltage contacts, the current and voltage contact pads may be connected using a wire bonder. The bright material is the contact pad aluminium, surrounded by oxide on silicon. The three dark horizontal lines are aluminium wires.

6.3 Measurement engineering

The probes are connected by shielded wires to an Agilent 34970a Switch Unit with Agilent 34901a 20-channel Multiplexer. This computer-controlled multiplexer switches two of four source/sense-pairs of probes to a Keithley 2602 Source Measurement Unit.

The source measurement unit (SMU) is also computer-controlled and performs four-point measurements on its connected probes. The source variable is voltage. In principle, current-controlled measurements should give the same result. However, as evidenced by figure 6.4, this is not the case for low-current measurements.

A possible explanation is in the higher stability of applied voltages; there is then only one feedback loop to keep the current steady, while in current-controlled systems the applied current has its control errors, which the voltage tries to follow in a second control loop.

The basic measurement scheme is shown in figure 6.5. For pit-based devices, four sets of probes are defined. These four sets correspond to the possible four-point measurements over two adjacent corners of the pit. For tetrahedron-based devices, there are three such sets. In measurements, the setup applies a voltage to one source probe pair. The system then start controlling the current such that no current flows through the voltage probes. After a settling time, normally $t = 500\,\mathrm{ms}$, the resulting current is recorded, along with the actual voltage. This is repeated for each probe set. The system then moves on to the next voltage and repeats the procedure. In this way, the voltage is ramped from zero up in steps, normally $\Delta V = 100\,\mathrm{mV}$, to a maximum voltage, commonly $V_{\mathrm{max}} = 1.0\,\mathrm{V}$. From there, the voltage is ramped down to $V = -V_{\mathrm{max}}$ and back up again to zero.

In this way, IV-curves on all contact pairs are drawn simultaneously. This approach was chosen over the alternative of characterising the contact pairs in series to minimise the time between analogous measurements on different contact pairs. Any change in device properties caused by the measurement process, such as contact oxidation or motion of trapped charges, will then affect all IV-curves in equal measure, preserving as much of the symmetry in the system as possible.

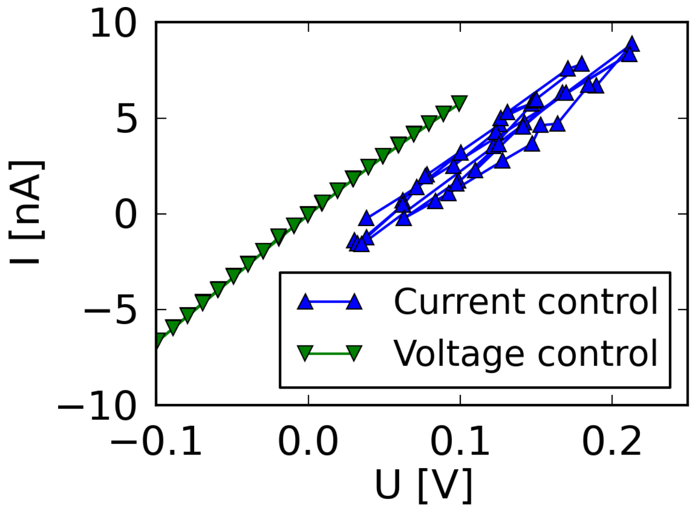

Figure 6.4: At low currents, voltage controlled measurements on the SMU show significantly better results than current controlled measurements.

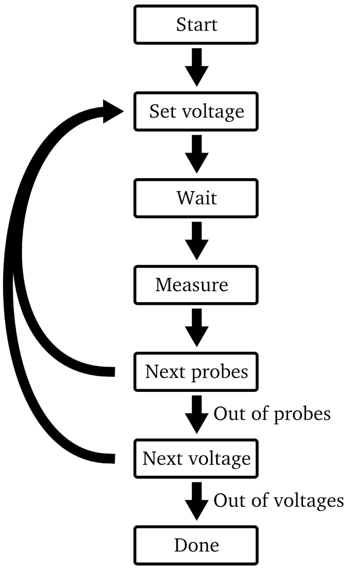

Figure 6.5: Measurements in the light direction sensing setup. For each voltage a measurement is made on each set of probes before moving on to the next set of probes.

6.4 High-ohmic measurements

High-ohmic measurements are sensitive to leakage currents. In particular considering the small distance between contacts in the devices considered here, it is a very real risk that contamination of the surface of the detector will result in relatively large parasitic currents. This can be resolved to some degree by taking care to keep the devices clean and possibly working under constant air (or nitrogen) flow. [29] Another option is priming the surface to make it hydrophobic, thus preventing the formation of a water film.

If problems persist, a solid insulating layer may be deposited on top of the system. In case of semiconductor leads, thermal growing of an oxide buffer layer can be used to isolate the detector environs. With metal contacts, it may be practical to deposit an unrelated insulator on all materials involved.

On the present setup, characterisation of fabricated devices placed them well short of the $R > 100\,\mathrm{M\Omega}$ high-resistance regime. As such, no explicit airflow was implemented on the setup.

6.5 AC vs DC operation

Direct current measurements are the simplest way to find IV curves. A steady voltage leads to a steady current and these pairs form an IV-point. In alternating current measurements the voltage and current are applied and analysed at some specific non-zero frequency.

The most obvious advantage of AC over DC measurement is that interfering signals at other frequencies are easily filtered out. In addition, signals can be sent over small gaps, provided their capacitance leads to a sufficiently small impedance at the signal frequency. This may allow measurements to be performed despite poor contacts.

However, there are also drawbacks. Signal attenuation is a common issue and the dissipation of power into the circuit may lead to other deviations.[29]

DC operation of the setup is the simplest method and will be used unless results suggest that different technique might improve performance.

6.6 Temperature management

Working with light and currents generates heat, possibly affecting measurements. In semiconductor materials, higher temperatures increase steady-state free carrier concentrations, leading to increased conductance.

The light sources used for testing have an output power of several watts and silicon has a specific heat capacity of about $c_p = 700\,\frac{\mathrm{J}}{\mathrm{K\,kg}}$. This means that in the absence of cooling, the light may heat the $d_d = 5\,\mathrm{\mu m}$ device layer of a $2r = 100\,\mathrm{mm}$ wafer by tens of kelvins per second.

The temperature dependence of semiconductor conductivity is commonly described using the Steinhart-Hart equation [33]

$$\frac{1}{T} = A + B\,\log(R) + C\,\log^3(R)$$

with parameters A, B and C depending on materials and geometry. The resulting curve for a typical thermistor is shown in figure 6.6. It shows that a twenty kelvin increase in temperature can reduce resistance to half its original value.

In case of a $d_{ox} = 1\,\mathrm{\mu m}$ oxide layer of thermal conductance $k = 1.4\,\frac{\mathrm{W}}{\mathrm{m\,K}}$, the steady-state temperature difference over the oxide will not exceed $\Delta T = d\frac{P/\pi r^2}{k} \ll 1\,\mathrm{K}$. The wafer will thus be at nearly uniform temperature and a heat sink at any point can be used to fix any heating issues.

The setup was designed such that all wafers be mounted on a large metal plate with plenty of heat sink compound. The metal plate should easily dissipate the generated heat.

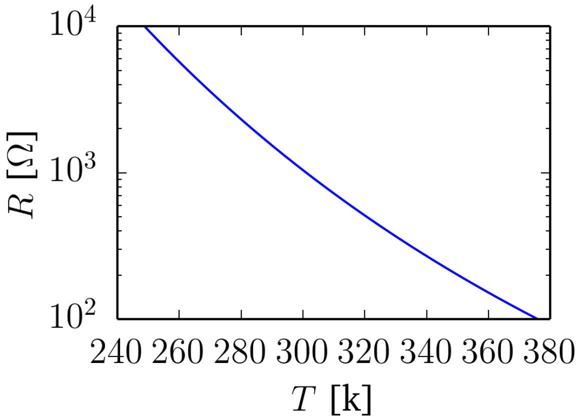

Figure 6.6: Resistance versus temperature for a typical thermistor, taken from [33]. The curve shows that a twenty kelvin temperature shift can change resistivity by as much as a factor of two.

To verify this, a SOI wafer was placed in the setup and an infrared thermometer calibrated for its emissivity. With room temperature at $T = 23\,°\mathrm{C}$, the light source was switched on to cyan, for maximum heat absorption. Although the LED light itself got uncomfortably hot, the sample did not register a temperature change over $\Delta T = 1.0\,°\mathrm{C}$. This would limit thermal drift in resistance values to $\frac{\Delta R}{R} = 3 \cdot 10^{-3}$.

6.7 Discussion

We have built a setup to apply an arbitrary radiance vector $\mathbf{L}(x, y)$ to a sample and characterise its electrical behaviour. The result applies a fixed radiant flux under a zenith angle up to $\theta = 60°$. From the theory in chapter 3 we expect the conductivity change to be linear in light intensity. A single intensity will thus be sufficient to study all aspects of the angular behaviour. The limited range of angles covers the full range where all detector surfaces are illuminated and where the detector is expected to be most sensitive. It is thus expected to provide all the data relevant to establishing light direction sensitivity.

The measurement scheme developed is expected to find the electrical behaviour of the resistor network in the samples. Measures can be taken to ensure good behaviour at high impedance, but this is not expected to be necessary. An analysis of temperature behaviour suggests that we will be able to keep this easily within the acceptable range.

Chapter 7

Light direction sensing results

Several of the devices fabricated in chapter 5 were characterised using two-point measurement within the setup through the technique described in chapter 6.2.

IV curve tracing showed shortage at $R = 1\,\mathrm{k}\Omega$ on several of the paths on these devices. This is likely due to residual traces of aluminium between a set of voltage leads.

Two devices were found entirely free of shortage. One, the device previously shown in 5.6, has dimensions $L = 40\,\mu\mathrm{m}$, $w = -2\,\mu\mathrm{m}$ and $c = 7\,\mu\mathrm{m}$. The other has dimensions $L = 40\,\mu\mathrm{m}$, $w = 0\,\mu\mathrm{m}$ and $c = 7\,\mu\mathrm{m}$. By comparing measurements on the two we may be able to distinguish colour to some degree. With these devices we cannot check the behaviour of small sensors.

We also note that neither device retains proper backside mirroring. Contrast between positive and negative angles for each resistor is thus expected to be very limited and entirely caused by the oxide. We can in fact quantify the predicted effect using the theory from chapter 3 and appendix A.

The oxide layer has a thickness $d = 108\,\mathrm{nm}$ and refractive index $n = 1.44$. It thus has an optical thickness of the same order as the (vacuum) wavelength of the light used, meaning that thin film interference must be taken into account. Depending on incident angle θ, a round trip through the film will produce a relative phase shift of

$$\Delta\phi = 2\pi \frac{n_{\mathrm{film}} d}{\lambda_{\mathrm{vac}}} \frac{1}{\cos\left(\sqrt{1 - \left(\frac{n_{\mathrm{air}}}{n_{\mathrm{film}}}\right)^2 \sin^2(\theta)}\right)}$$

It can then be shown [34] that

$$T = 1 - \frac{n_{\mathrm{film}}(n_{\mathrm{si}} - n_{\mathrm{air}})^2 \cos^2(2\Delta\phi) + (n_{\mathrm{si}} n_{\mathrm{air}} - n_{\mathrm{film}}^2)^2 \sin^2(2\Delta\phi)}{n_{\mathrm{film}}(n_{\mathrm{si}} + n_{\mathrm{air}})^2 \cos^2(2\Delta\phi) + (n_{\mathrm{si}} n_{\mathrm{air}} + n_{\mathrm{film}}^2)^2 \sin^2(2\Delta\phi)} \tag{7.1}$$

As the channel is symmetric but for the coating, we need only consider the total radiant flux entering the silicon. This results in the prediction of the angular behaviour shown in figure 7.1. We see that although the position of the peak shifts only slightly, the observed flux for positive and negative angles is very different, particularly at lower wavelengths. Note also the kinks in the curve where one of the faces no longer receives light.

The effects seen are clearly very different from the $\theta = 54.74°$ radiance peak expected for perfect resistors. Nevertheless, there are some obvious features. Although the peak does not shift farther than $\theta = 10°$ out of the centre, we see a strong asymmetry in the curve. Moving the light source towards the side with the oxide gives a much lower decrease than moving it the other way, particularly for lower wavelengths. This means that if we compare the readings from two opposite channels, we can still solve for the angle of incidence.

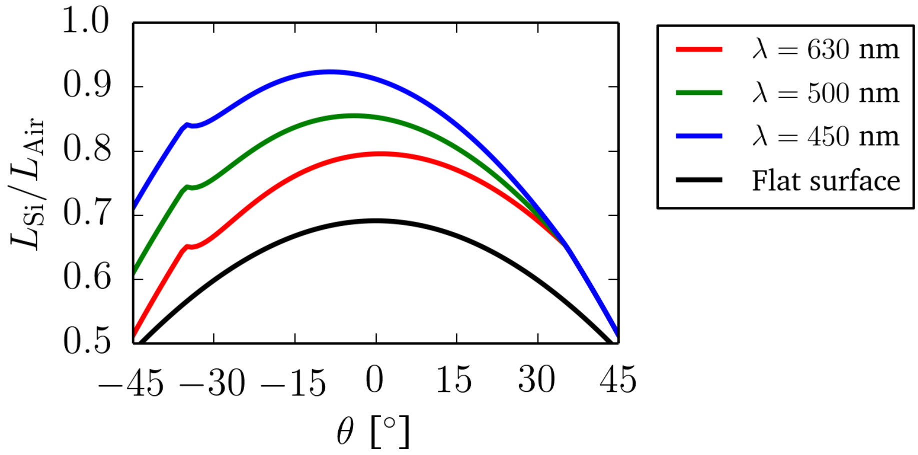

Figure 7.1: Radiant flux transmission as a function of incident angle as equation 7.1 predicts for the imperfect channels produced. In this image, we consider a channel with an oxide on the left side and rotate a light source from left to right. The curves represent red, green and blue light, as well as the behaviour of an unstructured flat surface for reference.

7.1 Results

With this in mind we measure the behaviour of one sample. Shown in figure 7.2 are the raw IV curves for two opposite channels. We note that the lowest resistance values are found at $\theta = -15°$ for both channels. However, the difference between the extreme angles $\theta = \pm 45°$ is much larger in one than in the other. This means that angular information can still be extracted from these data.

We also note that the linearity of the curves is very poor, particularly compared to the well-defined resistance values found for the materials testing samples in figure 4.5. Although those were four-point measurements, we have also established that the contacts had minimal effect on resistance. It is thus not clear why the curves have this shape. Importantly, all the curves within a series do have the same shape. If the magnitude of this curve still represents the underlying conductivity and if we are solely interested in their relative resistances, as we are, we can still use these curves freely.

The data from this measurement series were converted to observed resistances through least squares fitting of a straight line. Here one may define a cutoff value, so that only the points of voltage magnitude smaller than some set value are considered. Results with a cutoff at $V = 0.2\,\mathrm{V}$ and without cutoff are shown in figure 7.3. Comparing figures (a) and (b) we see that the absolute values of the resistors differ strongly. The relative positions of the resistors also move somewhat. This works out as a constant shift imposed upon each curve. The cutoff value thus does not appear to affect perceived light direction sensitivity.

The observed resistances with cutoff $V = 0.2\,\mathrm{V}$ were converted to parameters for the four-resistor model as discussed in chapter 3. These parameters are plotted in figure 7.4. We do, indeed, see an asymmetry in the β versus δ resistors. However, the behaviour is hard to spot, let alone quantify, inviting some further analysis.

Similar curves were taken under red, green and blue light under various angles. In addition, dark resistances were measured. These dark resistances were several orders of magnitude larger than those with light on, which means that the observed conductivity is entirely due to the photo-induced conductance change.

It was established in chapter 3 that the conductance change is purely linear in radiant flux. We can thus freely renormalise the curves without losing their angular information.

This was done in figure 7.5. Als shown here are the relevant error margins. The error in θ was determined in chapter 6 to be $\Delta\theta = \pm 2°$. The error in conductivity is the standard deviation

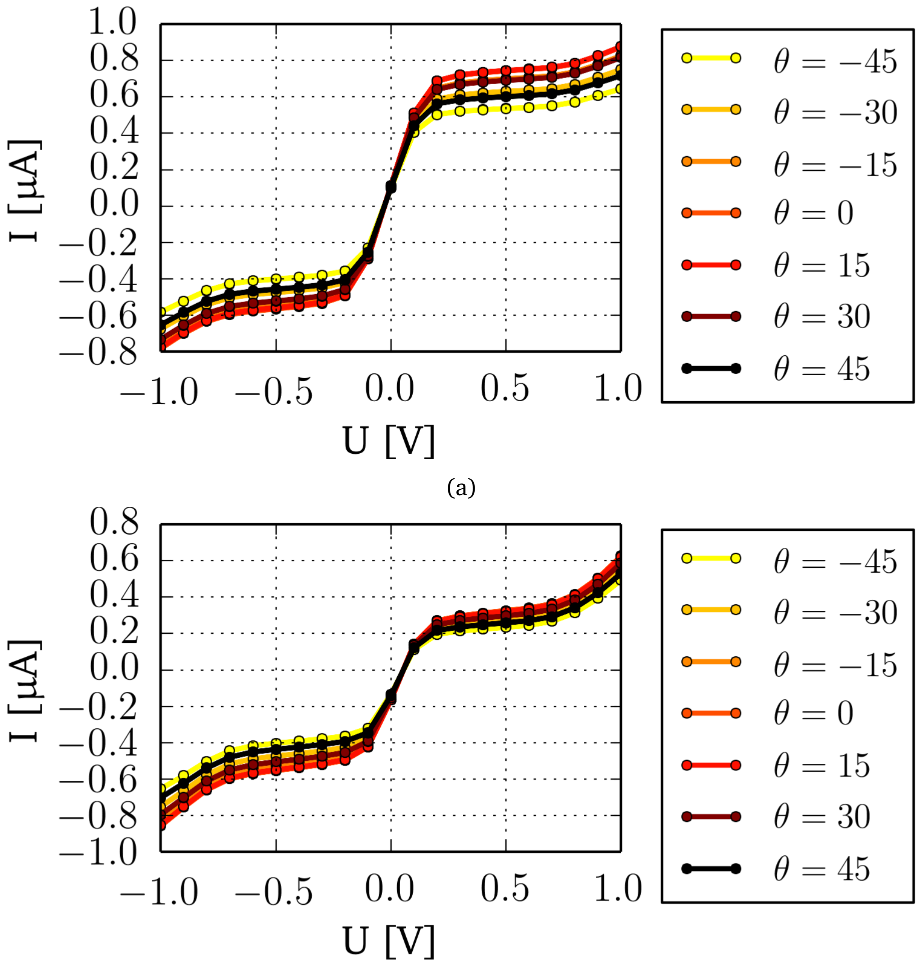

(a)

(b)

Figure 7.2: IV curves for two opposite channels on the $w = -2\,\mu\mathrm{m}$ device while moving the blue LED light source along their resolvable angle. Circles indicate measured points. The lowest resistances are found at $\theta = -15°$ in both cases. We do however see that the difference between the extreme lines at $\theta = \pm 45°$ are spaced much farther apart in (a) than in (b). This means that the angular response is still encoded in these curves. Note also that the curves are nowhere near linear.

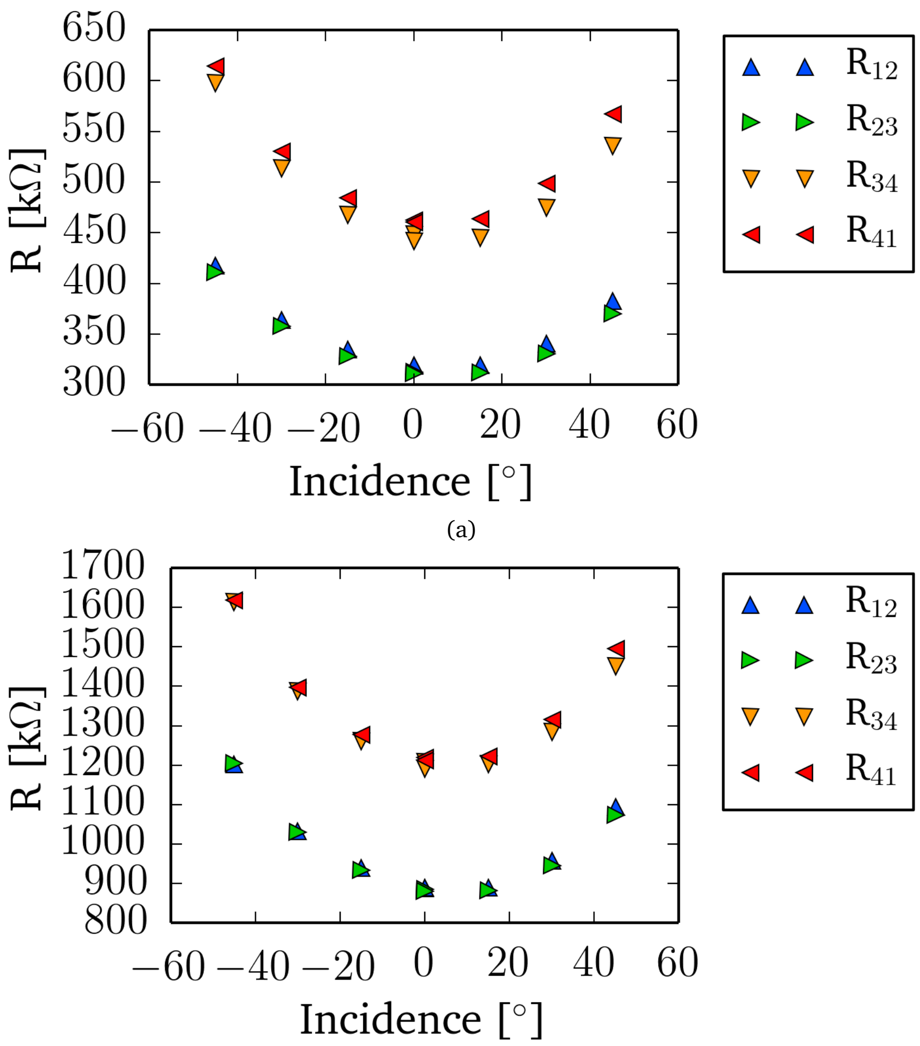

(a)

(b)

Figure 7.3: All four sets of IV curves from the measurement also discussed in figure 7.2 were translated to observed resistance values. (a) The IV points up to $V = 0.2\,\mathrm{V}$ were used in the fit. (b) all IV points were used in the fit.

in a set of points taken at different times with the same parameters and found to be around $\frac{d\sigma}{\sigma} = 1.5 \times 10^{-2}$. In this figure, we still expect the β and δ resistors to encode the incident angle. Indeed, their relative positions vary from one side to the other, from two standard deviations difference to nearly the same. However, the same goes for the α and γ resistors. This means that although incident angle is a statistically significant factor encoded in the measured data, this is not done in the predicted fashion.

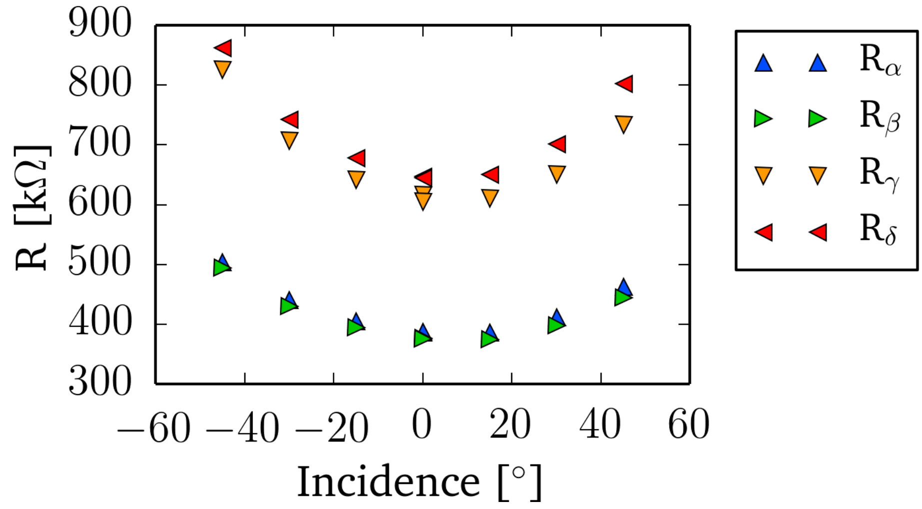

Figure 7.4: From the resistances in figure 7.3a, the parameters of the underlying four-resistance network were calculated and are shown here. Negative angles here imply a light source shining in from the 41 side; positive angles are from the 23 side.

Very similar results are found for different colours and directions and in repetitions of the same experiments. One further interesting result is shown in figure 7.6. Here, the light sources is moved diagonally, along the line between the nodes $\gamma\delta$ and $\alpha\beta$. This should result in identical behaviour for the α and β resistors, that should vary strongly relative to γ and δ. Changes of comparable magnitude as in figure 7.5 are observed in α and γ. β and δ however show a relative shift of less than one standard deviation.

7.2 Discussion

Interpreting the results by the previously developed theory, one could only explain the qualitative results in figure 7.5 by an error in azimuthal angle ϕ of several tens of degrees. It seems highly unlikely that this sort of error would have gone unnoticed in an experimental setting.

Quantitatively, the measured data are up to fifteen standard deviations off from the model. This may be explained partially from the resistances between the current contacts and the channel as seen in figure 5.6. The additional resistance is not as sensitive to incident angle as the channels because its resistance is set by light entering through one of a number of nearby surfaces. This will have the effect of keeping normalised resistance as in figure 7.5 closer to the average.

Note also the overall asymmetry around zero in all sets of curves. This asymmetry does not have a clear and set explanation. Although the model in figure 7.1 shows off-centre peaks, these should be reversed for opposite resistors. If the effect were caused by the different channel widths, the normalisation should have filtered it out.

The data presented here show a statistically significant effect of incident light direction. This means that they are proof of the concept of light direction sensing through three-dimensionally structured pixels. It is also clear that their performance is still suboptimal. In the current form, the effect is likely to be too small for applications.

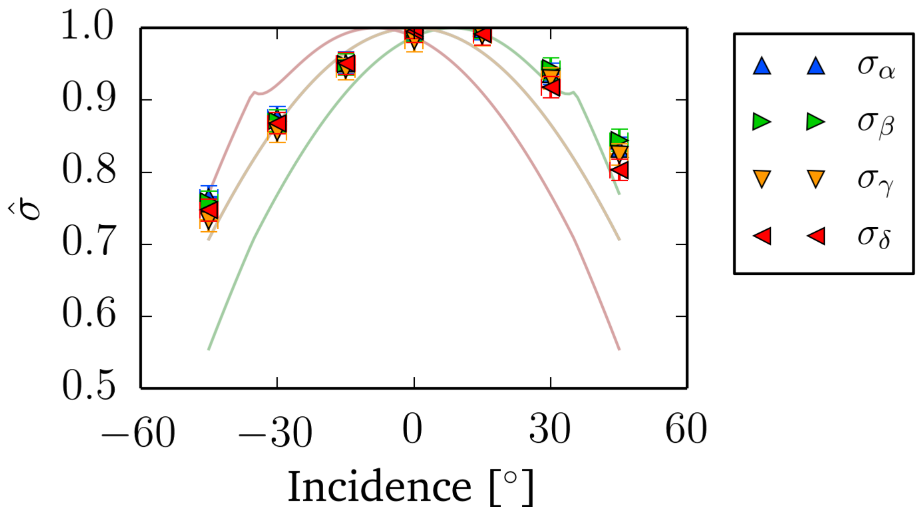

Figure 7.5: The normalised conductance of each measurement point in figure 7.3. The modelled behaviour is shown in the faded curves. In this plot, we expect the β and δ resistors to take on extreme values, while the α and γ resistors should not vary relative to one another. Although the variations in the β and δ resistors are indeed much larger, the α and γ resistors also vary in relation to one another.

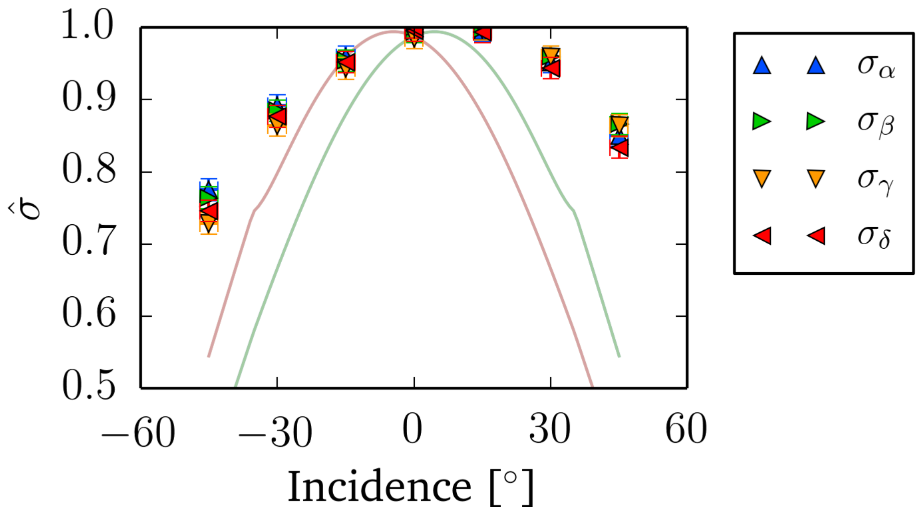

Figure 7.6: The normalised conductance values for a measurement conducted diagonally over the pit, from the node connecting γ and δ towards the node connecting α and β. We would expect both α and β to vary strongly relative to γ and δ, as indicated by the solid lines. However, one resistor, γ, varies most strongly. α and β do not change to comparable degree either.

Chapter 8

Conclusions & Outlook

The concept of detector surface structuring for light field detection was developed into conceptual detector designs. Qualitative analysis suggests that both pit-based and tetrahedron-based sensors would be able to quantify the full local light field vector $\mathbf{L}(x, y)$.

Anisotropic etching was discussed and found to be a convenient way to introduce sloped surfaces in silicon devices. The photoconductive effect was introduced as the method of choice to detect light in proof-of-concept semiconductor devices. Silicon-infused aluminium was found to be the best type of metal for contacting this sort of device.

The diffusion of excited carriers in semiconductor devices was studied in one- and three-dimensional systems. Explicit expressions for the steady-state carrier concentration profiles for semi-infinite and finite one-dimensional systems under realistic boundary conditions were found by qualitative and Green's functional analysis.

A Green's function for the three-dimensional general diffusion equation was found and used to show that no analytic solution for the diffusion equation on a tetrahedron can be found by this or a similar method. A quasi-analytic model was briefly studied and produced promising first results, suggesting a path towards good approximate expressions for the solution to arbitrary three-dimensional diffusion problems. A treatment of resistors with various conductivity patterns shows that many types of resistors may be modelled accurately by a few simple geometric variables. From this theory, a quantitative model of pit-based detector behaviour in local light field $\mathbf{L}(x, y)$ was developed and noted to verify the idea that the full light field vector can be characterised by this type of device. The same was qualitatively argued for tetrahedron-based detectors. It was also predicted that sets of these devices can be used to analyse the spectral composition of incident light by comparing devices of different dimensions. The ideal parameters of the substrates to be used were discussed so that wafers fitting within these ranges might be acquired.

The properties of the acquired wafers and several required cleanroom processing steps were studied through especially designed materials characterisation samples. Conductivity was found to be $\sigma = (5.5 \pm 1.0)10^{-3}\,\frac{1}{\Omega\,\mathrm{m}}$ and bulk excess carrier lifetime was fit to the theoretical model as $\tau = 2.0\,\mathrm{\mu s}$, within the realistic range described by sources.

Detector designs were converted to fabrication process flows. A custom CMOS-compatible detector fabrication process using only furnaces, an evaporator and wet etches was designed. Fabrication was then performed in the MESA+ cleanroom. The combination of thermal oxides and TMAH etched produced the desired detector surface structures. Contact patterning did not result in the desired voltage contacts and mirrors, possibly due to a flaw in the final lithography step, leaving devices not expected to have very good direction sensitivity and with inferior readout capabilities.

An experimental setup for the characterisation of detectors under a wide range of light field vectors $\mathbf{L}(x, y)$ was developed. It was found to perform well on dummy samples.

The fabricated devices were characterised on the setup. Direction sensitivity was found in all measurable devices, with normalised conductance values shifting one standard deviation over an angle $\theta = 120°$. Results are smaller than expected from the model and correspond more closely to an azimuthal angle tens of degrees off than to the angles actually used in experiment. The results do confirm the theoretical prediction that structured detector surfaces may be used to fabricate light field sensors. Detectors with backside mirroring are expected to function much better, but this cannot be concluded from these data.

The next step in this project would be a revision of the fabrication process, as it is very likely that one of the suggestions in chapter 5 leads to backside-mirrored detectors with all the relevant contacts. Other design improvements might include strong doping of the contact areas to produce four photodiodes. This would simplify the analysis of measurements and eliminate any possible interference from contact effects. A fabrication scheme with a single TMAH step might also be interesting from a commercial point of view.

The models used for the prediction of light direction sensistivity are still expected to hold for well-fabricated devices. For the devices measured in this work, models might be improved by taking into account the extra resistance due to contacting. However, producing devices of higher expected performance is deemed more interesting.

This work has not looked into the reproducibility of the processes. For applications this is important. Further research might investigate the degree to which the process may be tuned to obtain detectors with predictable properties.

Appendix A

Electromagnetic waves

Electromagnetic wave propagation is fully described by Maxwell's equations[10]

$$\nabla \cdot \mathbf{E} = \frac{\rho}{\epsilon} \tag{A.1}$$

$$\nabla \cdot \mathbf{B} = 0 \tag{A.2}$$

$$\nabla \times \mathbf{E} = -\frac{\partial \mathbf{B}}{\partial t} \tag{A.3}$$

$$\nabla \times \mathbf{B} = \mu \mathbf{J} + \mu\epsilon \frac{\partial \mathbf{E}}{\partial t} \tag{A.4}$$

In the absence of free charges and currents[1], the equations allow for the existence of electromagnetic waves. Taking the time derivative of the magnetic field's rotation from equation A.4,

$$\begin{aligned}
\frac{\partial}{\partial t}\left(\nabla \times \mathbf{B}\right) &= \frac{\partial}{\partial t}\left(\mu \mathbf{J}\right) + \frac{\partial}{\partial t}\left(\mu\epsilon\frac{\partial \mathbf{E}}{\partial t}\right) \\
\nabla \times \frac{\partial \mathbf{B}}{\partial t} &= 0 + \mu\epsilon\frac{\partial^2}{\partial t^2}\mathbf{E} \\
-\nabla \times \nabla \times \mathbf{E} &= \mu\epsilon\frac{\partial^2}{\partial t^2}\mathbf{E} \\
\nabla^2 \mathbf{E} - \nabla\left(\nabla \cdot \mathbf{E}\right) &= \mu\epsilon\frac{\partial^2}{\partial t^2}\mathbf{E} \\
\nabla^2 \mathbf{E} - \nabla\left(\frac{\rho}{\epsilon}\right) &= \mu\epsilon\frac{\partial^2}{\partial t^2}\mathbf{E} \\
\nabla^2 \mathbf{E} &= \mu\epsilon\frac{\partial^2}{\partial t^2}\mathbf{E}
\end{aligned}$$

which has the form of a wave equation. A magnetic counterpart can be found and has the same wave velocity $v = \frac{1}{\sqrt{\mu\epsilon}} \equiv \frac{c}{n}$. Note that the equations hold equally well under complex μ and ϵ.

The two wave equations are mutually solved by

$$\mathbf{E} = E_0 \;\; \mathrm{e}^{i(kz-\omega t)}\hat{\mathbf{x}} \qquad\qquad \begin{aligned} \mathbf{B} &= B_0 \quad \mathrm{e}^{i(kz-\omega t)}\hat{\mathbf{y}} \\ &= \frac{n}{c}E_0 \;\; \mathrm{e}^{i(kz-\omega t)}\hat{\mathbf{y}} \end{aligned}$$

resulting in a wave travelling in the $\hat{\mathbf{z}}$ direction. Any interaction between the wave and the medium is caught in the wavenumber $k = \frac{n}{c}\omega$.[2] A complex refractive index here means complex

---

[1] It is interesting to wonder if these are one or two assumptions.

[2] This is the velocity obtained by following a single point in the waveform around. Formally, we set $\frac{d(kz)}{d(\omega t)} = 0$

wavenumber, which means the wave changes in intensity. It is thus clear that the imaginary part of $n = \sqrt{\frac{\mu\epsilon}{\mu_0\epsilon_0}}$ corresponds to absorption.

For the interface of two continuous media, we can write, based again on equations A.1 through A.4

$$\begin{aligned} \epsilon_1\mathbf{E}_1^{\perp} - \epsilon_2\mathbf{E}_2^{\perp} &= \sigma_f \\ \mathbf{B}_1^{\perp} - \mathbf{B}_2^{\perp} &= 0 \\ \mathbf{E}_1^{\|} - \mathbf{E}_2^{\|} &= 0 \\ \frac{1}{\mu_1}\mathbf{B}_l^{\|} - \frac{1}{\mu_2}\mathbf{B}_2^{\|} &= K_f \times \hat{\mathbf{z}} \end{aligned}$$

We can consider a wave as considered before arriving perpendicularly at region 2 from region 1. There may be a reflected and a transmitted wave,

$$\mathbf{E} = E_{\mathrm{R}}\ \mathrm{e}^{i(-kz-\omega t)}\hat{\mathbf{x}} \qquad \mathbf{B} = -\frac{n_1}{c}E_{\mathrm{R}}\ \mathrm{e}^{i(-kz-\omega t)}\hat{\mathbf{y}}$$

and

$$\mathbf{E} = E_{\mathrm{T}}\ \mathrm{e}^{i(k_2z-\omega t)}\hat{\mathbf{x}} \qquad \mathbf{B} = \frac{n_2\,n_1}{c}E_{\mathrm{T}}\ \mathrm{e}^{i(k_2z-\omega t)}\hat{\mathbf{y}}$$

If no surface charges or currents exist, the perpendicular fields are null and we are left with

$$E_0 + E_{\mathrm{R}} = E_{\mathrm{T}} \tag{A.5}$$

and

$$\begin{aligned} \frac{1}{\mu_1}(B_0 - B_{\mathrm{R}}) &= \frac{1}{\mu_2}B_{\mathrm{T}} \\ \frac{n_1}{\mu_1 c}(E_0 - E_{\mathrm{R}}) &= \frac{n_2}{\mu_2\,c}E_{\mathrm{T}} \end{aligned}$$

For diamagnetic materials, including air and silicon, μ is within a few parts per million of its vacuum value.[11] Ignoring this difference, we find

$$E_0 - E_{\mathrm{R}} = n\,E_{\mathrm{T}} \tag{A.6}$$

with $n = \frac{n_2}{n_1}$. Combining equations A.5 and A.6 we find

$$E_{\mathrm{R}} = \left(\frac{1-n}{1+n}\right)E_0 \qquad E_{\mathrm{T}} = \left(\frac{2}{1+n}\right)E_0$$

which are specific cases of the Fresnel equations.

Considering also oblique incidence, the same method can be used to find reflectance factors of

$$R^{\perp} = \left|\frac{\cos\theta - n\sqrt{1-\frac{1}{n^2}\sin^2\theta}}{\cos\theta + n\sqrt{1-\frac{1}{n^2}\sin^2\theta}}\right|^2$$

and

$$R^{\|} = \left|\frac{\sqrt{1-\frac{1}{n^2}\sin^2\theta} - n\cos\theta}{\sqrt{1-\frac{1}{n^2}\sin^2\theta} + n\cos\theta}\right|^2$$

for light polarised perpendicular to the plane of incidence, and parallel to it, respectively. Transmission coefficients can be found from $T = 1 - R$.

Appendix B

Semiconductor optics

Colour	λ
Deep violet	$380\,\mathrm{nm}$
Blue	$450\,\mathrm{nm}$
Green	$500\,\mathrm{nm}$
Red	$630\,\mathrm{nm}$
Deep red	$750\,\mathrm{nm}$

The complex refractive index of intrinsic silicon versus wavelength is tabulated in [12]. Its magnitude varies by 80% over the visible spectrum, but mostly in the region from violet to green. The imaginary part of the index, representing absorption, is quite significant at the blue end of the spectrum, but decreases by two orders towards the red end.

$$n = \begin{cases} 6.616 + 0.947\,i & | \quad \lambda = 380\,\mathrm{nm} \\ 4.691 + 0.086\,i & | \quad \lambda = 450\,\mathrm{nm} \\ 4.294 + 0.044\,i & | \quad \lambda = 500\,\mathrm{nm} \\ 3.879 + 0.016\,i & | \quad \lambda = 630\,\mathrm{nm} \\ 3.717 + 0.007\,i & | \quad \lambda = 750\,\mathrm{nm} \end{cases}$$

Reflectance at normal incidence for these wavelengths is

$$R = \begin{cases} 55\%\ ,\ \theta = 4.97^\circ & | \quad \lambda = 380\,\mathrm{nm} \\ 41\%\ ,\ \theta = 2.67^\circ & | \quad \lambda = 450\,\mathrm{nm} \\ 39\%\ ,\ \theta = 0.53^\circ & | \quad \lambda = 500\,\mathrm{nm} \\ 35\%\ ,\ \theta = 0.26^\circ & | \quad \lambda = 630\,\mathrm{nm} \\ 33\%\ ,\ \theta = 0.12^\circ & | \quad \lambda = 750\,\mathrm{nm} \end{cases}$$

where also the extra phase shift is noted. It should be noted that even for the deep violet light, the absorbance does not increase the reflectance by more than one percent.

Absorption itself is more strongly affected. The imaginary part of the index can be rewritten as an absorption length after which the wave retains $\frac{1}{e} = 37\%$ of its intensity through $\frac{1}{\alpha} = \frac{\lambda}{4\pi k}$ with $k = \mathrm{Im}(n)$. Half this distance, the skin depth l_s, is enough to reduce wave energy by the same amount.

$$l_\mathrm{s} = \frac{1}{2\alpha} = \begin{cases} 15.97\ \mathrm{nm} & | \quad \lambda = 380\,\mathrm{nm} \\ 207.5\ \mathrm{nm} & | \quad \lambda = 450\,\mathrm{nm} \\ 450.5\ \mathrm{nm} & | \quad \lambda = 500\,\mathrm{nm} \\ 1\,525\ \mathrm{nm} & | \quad \lambda = 630\,\mathrm{nm} \\ 3\,817\ \mathrm{nm} & | \quad \lambda = 750\,\mathrm{nm} \end{cases}$$

High absorption length means very little light will be absorbed and absorption effects will be of similar magnitude throughout the device. Very small absorption length means free carriers will be lost quickly through surface recombination.

Data from amorphous silicon show that strong doping changes refractive index by up to 10%, with lower index in p-doped silicon and higher index in n-doped material.

Compared to the slope of the skin depth-wavelength relation, the spectrum of a LED light source is quite narrow. This means that LEDs of different colours can be used to sample the skin depth curve. This is illustrated in figure 6.2.

Appendix C

Green's functions for the diffusion equation in three dimensions

In rectangular coordinates, aligning l with z, the equation to be solved is

$$\frac{dc}{dt} = \frac{\eta}{hf}\frac{I_0}{l_\mathrm{s}}\,\mathrm{e}^{-\frac{z}{l_\mathrm{s}}} - \frac{c}{\tau} + D\,\nabla^2 c \tag{C.1}$$

or, in the steady state,

$$\begin{aligned} L\,c + f(z) &= 0 \\ \text{with}\quad L &= \nabla^2 - \frac{1}{l_\mathrm{d}^2} \\ f(z) &= \frac{\eta}{hf}\frac{\tau}{l_\mathrm{d}^2}\frac{I_0}{l_\mathrm{s}}\,\mathrm{e}^{-\frac{z}{l_\mathrm{s}}} \end{aligned}$$

Equations of this form are known as screened Poisson equations and are occasionally encountered in particle physics. For the tetrahedron, we have the boundaries[1]

Laplace:
$\nabla^2 U = 0$
Poisson:
$\nabla^2 U = f$
Helmholtz:
$(\nabla^2 + \lambda^2)\,U = 0$
Screened Poisson:
$(\nabla^2 - \lambda^2)\,U = f$

$$\begin{aligned} c(z = 0) &= 0 \\ c(z = l_\mathrm{w} + 2\sqrt{2}\,y) &= 0 \\ c(z = l_\mathrm{w} - \sqrt{2}\,y + \sqrt{6}\,x) &= 0 \\ c(z = l_\mathrm{w} - \sqrt{2}\,y - \sqrt{6}\,x) &= 0 \end{aligned}$$

For the system at hand we look for a Green's function G as

$$(\nabla^2 - \lambda^2)\,G(\mathbf{r}) = -\delta(\mathbf{r})$$

This equation can be transformed to momentum space as

$$\begin{aligned} \mathcal{F}\big(\,\nabla^2 G(\mathbf{r})\,\big) - \lambda^2 \mathcal{F}(\,G(\mathbf{r})\,) &= -\mathcal{F}(\,\delta(\mathbf{r})\,) \\ -k^2 G(\mathbf{k}) - \lambda^2 G(\mathbf{k}) &= -1 \\ G(\mathbf{k}) &= \frac{1}{k^2 + \lambda^2} \end{aligned}$$

---

[1] We use a coordinate system centred on the middle of the face on which light is incident. Also note that $l_\mathrm{w} = \frac{\sqrt{6}}{3} r$.

Transforming back to real space,

$$\begin{aligned} G(\mathbf{r}) &= \frac{1}{(2\pi)^3} \iiint G(\mathbf{k})\, \mathrm{e}^{i\,\mathbf{k}\cdot\mathbf{r}} d^3\mathbf{k} \\ &= \frac{1}{(2\pi)^3} \iiint \frac{\mathrm{e}^{i\,\mathbf{k}\cdot\mathbf{r}}}{k^2+\lambda^2} d^3\mathbf{k} \end{aligned}$$

This equation is radially symmetric. We solve it in spherical coordinates, aligned along the $\hat{\mathbf{r}}$ vector.

$$\begin{aligned} G(\mathbf{r}) &= \frac{1}{(2\pi)^3} \int_{k=0}^{\infty} \int_{\theta=0}^{\pi} \int_{\phi=0}^{2\pi} \frac{\mathrm{e}^{ikr\cos(\theta)}}{k^2+\lambda^2} k^2 \sin(\theta)\, d\phi\, d\theta\, dk \\ &= \frac{1}{(2\pi)^2} \int_{k=0}^{\infty} \int_{\theta=0}^{\pi} \frac{\mathrm{e}^{ikr\cos(\theta)}}{k^2+\lambda^2} k^2 \sin(\theta)\, d\theta\, dk \\ &= \frac{1}{(2\pi)^2} \int_{k=0}^{\infty} \int_{a=kr}^{-kr} \frac{\mathrm{e}^{ia}}{k^2+\lambda^2} (-\frac{k}{r})\, da\, dk \\ &= \frac{1}{2\pi^2 r} \int_{0}^{\infty} \frac{k}{k^2+\lambda^2} \frac{\mathrm{e}^{ikr} - \mathrm{e}^{-ikr}}{2i}\, dk \\ &= \frac{1}{2\pi^2 r} \int_{0}^{\infty} \frac{\frac{i\tilde{k}}{\lambda}}{\tilde{k}^2+1} \frac{\mathrm{e}^{i\lambda\tilde{k}r} - \mathrm{e}^{-i\lambda\tilde{k}r}}{2i} \lambda\, d\tilde{k} \\ &= \frac{1}{2\pi^2 r} \int_{-\infty}^{\infty} \frac{\tilde{k}}{\tilde{k}^2+1} \frac{\mathrm{e}^{i\lambda\tilde{k}r}}{2i}\, d\tilde{k} \\ &= \frac{1}{4\pi^2 ir} \int_{-\infty}^{\infty} \frac{\tilde{k}\ \mathrm{e}^{i\lambda\tilde{k}r}}{\tilde{k}^2+1}\, d\tilde{k} \\ &= \frac{1}{4\pi^2 ir} \int_{-\infty}^{\infty} h(\tilde{k})\, d\tilde{k} \end{aligned}$$

Using $\tilde{k} = \frac{k}{\lambda}$ and $h(\tilde{k}) = \frac{\tilde{k}\ \mathrm{e}^{i\lambda\tilde{k}r}}{\tilde{k}^2+1}$. The remaining equation can be solved through complex analysis. We consider the contour C composed of the line segment $\tilde{k} = [-a, a]$ and the semicircle $\tilde{k} = \{a\,\mathrm{e}^{i\theta} \mid \theta = [0, \pi]\}$ connecting these ends. With $a > 1$ this contour includes one of two poles of $h(\tilde{k})$, at $k = i$.

If we now increase our contour dimension $a \to \infty$, the contour integral is equivalent to

$$\begin{aligned} \oint_C h(\tilde{k})d\tilde{k} &= \int_{\text{line}} h(\tilde{k})d\tilde{k}\ + \int_{\text{curve}} h(\tilde{k})d\tilde{k} \\ &= \int_{-\infty}^{\infty} h(\tilde{k})d\tilde{k} + \lim_{a\to\infty} \int_0^{\pi} h(a\ \mathrm{e}^{i\theta})d\theta \end{aligned}$$

For complex k, we have

$$h(|\tilde{k}|\,\mathrm{e}^{i\theta}) = \frac{|\tilde{k}|\,\mathrm{e}^{i\theta}\ \mathrm{e}^{i\lambda r|\tilde{k}|\,\mathrm{e}^{i\theta}}}{|\tilde{k}|^2\,\mathrm{e}^{i2\theta}+1} = \frac{|\tilde{k}|\,\mathrm{e}^{i\theta}\ \mathrm{e}^{i\lambda r|\tilde{k}|\cos(\theta)}(1-|\tilde{k}|^2\,\mathrm{e}^{-2i\theta})\,\mathrm{e}^{-\lambda r|\tilde{k}|\sin(\theta)}}{|\tilde{k}|^4+2|\tilde{k}|^2\cos(2\theta)+1}$$

For $0 < \theta < \pi$, the negative exponential term in the numerator reduces $h(\tilde{k})$ faster than any polynomial function. Near the real axis two infinitesimal regions have finite $h(\tilde{k})$ values. Looking back to the integral $\int_{\text{curve}} h(\tilde{k})d\tilde{k}$ we see that for the region $0 < \theta < \pi$ the integrand decreases more quickly than the contour length increases with increasing a. The regions near the real axis have a finite value over negligible length. From this we find that $\lim_{a\to\infty} \int_0^{\pi} h(a\ \mathrm{e}^{i\theta})d\theta = 0$ and

$$\oint_C h(\tilde{k})d\tilde{k} = \int_{-\infty}^{\infty} h(\tilde{k})d\tilde{k}$$

We now consider a circular contour around a point $z = z_0$ on the function $(z - z_0)^n$ with integer n. Using $r = z - z_0$ we can write

$$\oint_C f(z)dz = \int_0^{2\pi} (r^n\,\mathrm{e}^{in\theta})(ir\,\mathrm{e}^{i\theta})d\theta = ir^{n+1}\int_0^{2\pi} \mathrm{e}^{i(n+1)\theta}d\theta$$
$$= \begin{cases} ir^{n+1}\left[\frac{\mathrm{e}^{i(n+1)\theta}}{i(n+1)}\right]_0^{2\pi} & = 0 \quad | \quad n \neq -1 \\ i\int_0^{2\pi} d\theta & = 2\pi i \quad | \quad n = -1 \end{cases}$$

Note that the above result holds for contours of arbitrary shape, as these can be constructed by summing over many smaller circular contours, with those not surrounding a pole evaluating to zero.

With these observations, we consider a contour C around $z = z_0$ on some function $\frac{f(z)}{z - z_0}$, where $f(z)$ is some holomorphic function within C. Note that partial fractional expansion allows all functions with poles to be written in this form.

$$\oint_C \frac{f(z)}{z - z_0}dz = \oint_C \frac{f(z_0)}{z - z_0}dz + \oint_C \frac{f(z) - f(z_0)}{z - z_0}dz$$

As the size of the contour should not matter, we can consider the rightmost term for vanishing $z - z_0$. Since $f(z)$ is continuous, $f(z) - f(z_0)$ reduces to zero and the term must always be null. We can then use our earlier result to write

$$\oint_C \frac{f(z)}{z - z_0}dz = f(z_0)\oint_C \frac{1}{z - z_0}dz$$
$$= 2\pi i\, f(z_0)$$

provided only that z_0 is the sole pole within C. This very powerful result is known as Cauchy's integral formula and allows for the evaluation of many types of contour integrals.[22]

For our present problem, we can now write

$$\begin{aligned} G(\mathbf{r}) &= \frac{1}{4\pi^2 ir}\int_{-\infty}^{\infty} h(\tilde{k})d\tilde{k} = \frac{1}{4\pi^2 ir}\oint_C h(\tilde{k})d\tilde{k} \\ &= \frac{1}{4\pi^2 ir}\oint_C \frac{\tilde{k}\,\mathrm{e}^{i\lambda\tilde{k}r}}{\tilde{k}^2 + 1}d\tilde{k} = \frac{1}{4\pi^2 ir}\left[\frac{1}{2i}\oint_C \frac{\tilde{k}\,\mathrm{e}^{i\lambda\tilde{k}r}}{\tilde{k} - i}d\tilde{k} - \frac{1}{2i}\oint_C \frac{\tilde{k}\,\mathrm{e}^{i\lambda\tilde{k}r}}{\tilde{k} + i}d\tilde{k}\right] \\ &= \frac{1}{4\pi^2 ir}\left[\frac{2\pi i}{2i}\left[\tilde{k}\,\mathrm{e}^{i\lambda\tilde{k}r}\right]_{\tilde{k}=i} - \frac{1}{2i}\,0\right] = \frac{1}{4\pi^2 ir}\pi\, i\,\mathrm{e}^{-\lambda r} = \frac{\mathrm{e}^{-\lambda r}}{4\pi r} \\ &= \frac{\mathrm{e}^{-\frac{r}{l_\mathrm{d}}}}{4\pi r} \end{aligned}$$

Compare the Yukawa potential from meson field theory and the screened Coulomb potential in plasma physics.

Appendix D

Detector fabrication process flow

5 Process parameters

Step		Comment
1		SOI 400-1-10 um handle-oxide-device wafer; 1000-6000 Ohmcm device R.
2 **Cleaning in Ozone Steam (UCL)** (#clean142)	NL-CLR-WB12 Purpose: removal of organic and inorganic traces for UCL processing.	
3 **Etching in HF (1%)** (#etch214)	NL-CLR-WB12 Purpose: to strip the native SiO2 from silicon wafers. Beaker: HF 1% Time = 1 min	The etching of native SiO2 is optional.
4 **Quick Dump Rinse (QDR)** (#rinse119)	NL-CLR-Wetbenches Purpose: removal of traces of cleaning agents. Recipe 1 Quick dump rinsing (QDR) Recipe 2 Cascade rinsing for fragile wafers Rinse until message ´End of rinsing process´ is shown on the touchscreen of the QDR, else repeat the rinsing process.	
5 **Substrate drying** (#dry120)	NL-CLR-WB **Single substrate drying:** 1. Use the single-wafer spinner Settings: 2500 rpm, 60 sec (including 45 sec nitrogen purge) 2. Use the nitrogen gun (fragile wafers or small samples)	
6 **Dry Oxidation of Silicon (UCL)** (#film175)	NL-CLR-Tempress-furnace A2 Standby temperature: 700°C • Temp range.: 800 up to 1100°C • Gas: O_2 • Flow: 4l/min • Ramp: 10°C/min • Cooldown: 7.5 °C/min • Standard programs: UCL-2 950 °C (time variable) UCL-1 1100 °C (time variable)	Dry, 950 degrees Celcius; grows 80 nm in three hours.
7		Mask 1: silicon patterning
8 **Dehydration bake** (#lith102)	NL-CLR-WB21/22 dehydration bake at hotplate	Continue immediately with priming.

	• temp. 120°C • time: 5min
9	
Priming (liquid) (#lith101)	NL-CLR-WB21/22 Primer: HexaMethylDiSilazane (HMDS) use spincoater: • program: 4000 (4000rpm, 30sec)
10	
Coating Olin Oir 907-17 (#lith105)	NL-CLR-WB21 Coating: Primus spinner • olin oir 907-17 • spin Program: 4000 (4000rpm, 30sec) Prebake: hotplate • time 90 sec • temp 95 °C
11	
Alignment & Exposure Olin OiR 907-17 (#lith121)	NL-CLR- EV620 Electronic Vision Group EV620 Mask Aligner • Hg-lamp: 12 mW/cm^{2} • Exposure Time: 4sec
12	
Development Olin OiR resist (#lith111)	NL-CLR-WB21 After exposurebBake : hotplate • time 60sec • temp 120°C development: developer: OPD4262 • time: 30sec in beaker 1 • time: 15-30sec in beaker 2
13	
Quick Dump Rinse (QDR) (#rinse119)	NL-CLR-Wetbenches Purpose: removal of traces of cleaning agents. Recipe 1 Quick dump rinsing (QDR) Recipe 2 Cascade rinsing for fragile wafers Rinse until message ´End of rinsing process´ is shown on the touchscreen of the QDR, else repeat the rinsing process.
14	
Substrate drying (#dry120)	NL-CLR-WB **Single substrate drying:** 1. Use the single-wafer spinner Settings: 2500 rpm, 60 sec (including 45 sec nitrogen purge) 2. Use the nitrogen gun (fragile wafers or small samples)
15	
Postbake Olin OiR resist	NL-CLR-WB21 postbake: Hotplate

(#lith109)	• temp 120°C • time 10min	
16		
Inspection by optical microscope (#metro101)	NL-CLR- Nikon Microscope • dedicated microscope for lithography inspection	
17		Preferably WB12
Etching in BHF (1:7) (#etch124)	NL-CLR-WB06/12 Use dedicated beaker BHF (1:7) • temp.: 20°C. Etchrates: Thermal SiO2:60-80nm/min PECVD SiO2 :125/nm/min TEOS-**old** SiO2 :180/nm/min TEOS **H3 (new)** :242 nm/min Si3N4-H2: 0,64 nm/min	
18		
Quick Dump Rinse (QDR) (#rinse119)	NL-CLR-Wetbenches Purpose: removal of traces of cleaning agents. Recipe 1 Quick dump rinsing (QDR) Recipe 2 Cascade rinsing for fragile wafers Rinse until message ´End of rinsing process´ is shown on the touchscreen of the QDR, else repeat the rinsing process.	
19		
Substrate drying (#dry120)	NL-CLR-WB **Single substrate drying:** 1. Use the single-wafer spinner Settings: 2500 rpm, 60 sec (including 45 sec nitrogen purge) 2. Use the nitrogen gun (fragile wafers or small samples)	
20		
Stripping polymers and resists in HNO_3 (99%) (#strip207)	NL-CLR-WB13-UCL Purpose: stripping of polymers and resists. • Beaker 0: HNO_3 (99%) • Time: continue until complete removal of resist	
21		
Quick Dump Rinse (QDR) (#rinse119)	NL-CLR-Wetbenches Purpose: removal of traces of cleaning agents. Recipe 1 Quick dump rinsing (QDR) Recipe 2 Cascade rinsing for fragile wafers Rinse until message ´End of rinsing process´ is shown on the touchscreen of the QDR, else repeat the rinsing process.	
22		

Substrate drying (WB13)
(#dry158)

NL-CLR-WB13

Single substrate drying:
1. Use the single-wafer spinner
Settings: 2500 rpm, 60 sec (including 45 sec nitrogen purge)
2. Use the nitrogen gun (fragile wafers or small samples)

Batch drying of substrates:
The Semitool uses the following standard procedure:
- Rinse: 30 sec (600 rpm)
- Q-rinse: 10.0 MΩ (600 rpm)
- Purge: 10 sec (600 rpm)
- Drying: 280 sec (1600 rpm)

Note: it is obligatory to apply a single rinsing step in the QDR before using the Semitool!

23

Etching 1% HF
(#etch210)

NL-CLR-WB06
use Beaker HF with 1%
- time variable
- native oxide strip 1 min or hydrofobic surface

Etchrate for:
TEOS H3 = 28 nm/min
Si_3N_4 H2 = .33 nm/min

24

Quick Dump Rinse (QDR)
(#rinse119)

NL-CLR-Wetbenches
Purpose: removal of traces of cleaning agents.

Recipe 1 Quick dump rinsing (QDR)
Recipe 2 Cascade rinsing for fragile wafers

Rinse until message ´End of rinsing process´ is shown on the touchscreen of the QDR, else repeat the rinsing process.

25

Etching in TMAH (25wt%)
(#etch147)

NL-CLR-WB07/10
Use beaker with TMAH (25%) standard
- temp.: 40°C
- use stirrer

Etchrate poly-si 590: 60nm/min

26

Quick Dump Rinse (QDR)
(#rinse119)

NL-CLR-Wetbenches
Purpose: removal of traces of cleaning agents.

Recipe 1 Quick dump rinsing (QDR)
Recipe 2 Cascade rinsing for fragile wafers

Rinse until message ´End of rinsing process´ is shown on the touchscreen of the QDR, else repeat the rinsing process.

27		
Substrate drying (#dry120)	NL-CLR-WB **Single substrate drying:** 1. Use the single-wafer spinner Settings: 2500 rpm, 60 sec (including 45 sec nitrogen purge) 2. Use the nitrogen gun (fragile wafers or small samples)	
28		Preferably WB12
Etching in BHF (1:7) (#etch124)	NL-CLR-WB06/12 Use dedicated beaker BHF (1:7) • temp.: 20°C. Etchrates: Thermal SiO2:60-80nm/min PECVD SiO2 :125/nm/min TEOS-**old** SiO2 :180/nm/min TEOS **H3 (new)** :242 nm/min Si3N4-H2: 0,64 nm/min	
29		
Quick Dump Rinse (QDR) (#rinse119)	NL-CLR-Wetbenches Purpose: removal of traces of cleaning agents. Recipe 1 Quick dump rinsing (QDR) Recipe 2 Cascade rinsing for fragile wafers Rinse until message ´End of rinsing process´ is shown on the touchscreen of the QDR, else repeat the rinsing process.	
30		
Substrate drying (#dry120)	NL-CLR-WB **Single substrate drying:** 1. Use the single-wafer spinner Settings: 2500 rpm, 60 sec (including 45 sec nitrogen purge) 2. Use the nitrogen gun (fragile wafers or small samples)	
31		
Cleaning in Ozone Steam (UCL) (#clean142)	NL-CLR-WB12 Purpose: removal of organic and inorganic traces for UCL processing.	
32		The etching of native SiO2 is optional.
Etching in HF (1%) (#etch214)	NL-CLR-WB12 Purpose: to strip the native SiO2 from silicon wafers. Beaker: HF 1% Time = 1 min	
33		
Quick Dump Rinse	NL-CLR-Wetbenches	

(QDR) (#rinse119)	Purpose: removal of traces of cleaning agents. Recipe 1 Quick dump rinsing (QDR) Recipe 2 Cascade rinsing for fragile wafers Rinse until message ´End of rinsing process´ is shown on the touchscreen of the QDR, else repeat the rinsing process.	
34 **Substrate drying** (#dry120)	NL-CLR-WB **Single substrate drying:** 1. Use the single-wafer spinner Settings: 2500 rpm, 60 sec (including 45 sec nitrogen purge) 2. Use the nitrogen gun (fragile wafers or small samples)	
35 **Dry Oxidation of Silicon (UCL)** (#film175)	NL-CLR-Tempress-furnace A2 Standby temperature: 700°C • Temp range.: 800 up to 1100°C • Gas: O_2 • Flow: 4l/min • Ramp: 10°C/min • Cooldown: 7.5 °C/min • Standard programs: UCL-2 950 °C (time variable) UCL-1 1100 °C (time variable)	Dry, 950 degrees Celcius; grows 30 nm in one hour.
36		Mask 2: oxide patterning
37 **Dehydration bake** (#lith102)	NL-CLR-WB21/22 dehydration bake at hotplate • temp. 120°C • time: 5min	Continue immedialy with priming the step!
38		(lith1100) Lithography AZ4999 by spray coating for perfect step coverage
39		Alignment & exposure of AZ4999 (EV620)
40		Development AZ4999 Resist
41 **Quick Dump Rinse (QDR)** (#rinse119)	NL-CLR-Wetbenches Purpose: removal of traces of cleaning agents. Recipe 1 Quick dump rinsing (QDR) Recipe 2 Cascade rinsing for fragile wafers Rinse until message ´End of rinsing process´ is shown on the touchscreen of the QDR, else repeat the rinsing process.	
42 **Substrate drying** (#dry120)	NL-CLR-WB	

	Single substrate drying: 1. Use the single-wafer spinner Settings: 2500 rpm, 60 sec (including 45 sec nitrogen purge) 2. Use the nitrogen gun (fragile wafers or small samples)	
43		Postbake AZ4999 Resist 120 degrees 10 minutes
44 **Inspection by optical microscope** (#metro101)	NL-CLR- Nikon Microscope • dedicated microscope for lithography inspection	
45 **Etching in BHF (1:7)** (#etch124)	NL-CLR-WB06/12 Use dedicated beaker BHF (1:7) • temp.: 20°C. Etchrates: Thermal SiO2:60-80nm/min PECVD SiO2 :125/nm/min TEOS-**old** SiO2 :180/nm/min TEOS **H3 (new)** :242 nm/min Si3N4-H2: 0,64 nm/min	
46 **Quick Dump Rinse (QDR)** (#rinse119)	NL-CLR-Wetbenches Purpose: removal of traces of cleaning agents. Recipe 1 Quick dump rinsing (QDR) Recipe 2 Cascade rinsing for fragile wafers Rinse until message ´End of rinsing process´ is shown on the touchscreen of the QDR, else repeat the rinsing process.	
47 **Substrate drying** (#dry120)	NL-CLR-WB **Single substrate drying:** 1. Use the single-wafer spinner Settings: 2500 rpm, 60 sec (including 45 sec nitrogen purge) 2. Use the nitrogen gun (fragile wafers or small samples)	
48 **Stripping polymers and resists in HNO_3 (99%)** (#strip207)	NL-CLR-WB13-UCL Purpose: stripping of polymers and resists. • Beaker 0: HNO_3 (99%) • Time: continue until complete removal of resist	
49 **Quick Dump Rinse (QDR)** (#rinse119)	NL-CLR-Wetbenches Purpose: removal of traces of cleaning agents. Recipe 1 Quick dump rinsing (QDR)	

Recipe 2 Cascade rinsing for fragile wafers

Rinse until message ´End of rinsing process´ is shown on the touchscreen of the QDR, else repeat the rinsing process.

50

Substrate drying (WB13)
(#dry158)

NL-CLR-WB13

Single substrate drying:
1. Use the single-wafer spinner
Settings: 2500 rpm, 60 sec (including 45 sec nitrogen purge)
2. Use the nitrogen gun (fragile wafers or small samples)

Batch drying of substrates:
The Semitool uses the following standard procedure:
- Rinse: 30 sec (600 rpm)
- Q-rinse: 10.0 MΩ (600 rpm)
- Purge: 10 sec (600 rpm)
- Drying: 280 sec (1600 rpm)

Note: it is obligatory to apply a single rinsing step in the QDR before using the Semitool!

51

Etching 1% HF
(#etch210)

NL-CLR-WB06
use Beaker HF with 1%
- time variable
- native oxide strip 1 min or hydrofobic surface

Etchrate for:
TEOS H3 = 28 nm/min
Si3N4 H2 = .33 nm/min

52

Quick Dump Rinse (QDR)
(#rinse119)

NL-CLR-Wetbenches
Purpose: removal of traces of cleaning agents.

Recipe 1 Quick dump rinsing (QDR)
Recipe 2 Cascade rinsing for fragile wafers

Rinse until message ´End of rinsing process´ is shown on the touchscreen of the QDR, else repeat the rinsing process.

53

Etching in TMAH (25wt%)
(#etch147)

NL-CLR-WB07/10
Use beaker with TMAH (25%) standard
- temp.: 40°C
- use stirrer

Etchrate poly-si 590: 60nm/min

54

Quick Dump Rinse (QDR)
(#rinse119)

NL-CLR-Wetbenches
Purpose: removal of traces of cleaning agents.

Recipe 1 Quick dump rinsing (QDR)
Recipe 2 Cascade rinsing for fragile wafers

Rinse until message ´End of rinsing process´ is shown on the touchscreen of the QDR, else repeat the rinsing process.

55

Substrate drying
(#dry120)

NL-CLR-WB

Single substrate drying:
1. Use the single-wafer spinner
   Settings: 2500 rpm, 60 sec (including 45 sec nitrogen purge)
2. Use the nitrogen gun (fragile wafers or small samples)

56

Cleaning in HNO_3 (99%)
(#clean102)

NL-CLR-WB14
Purpose: removal of organic traces.

- Beaker 1: HNO_3 (99%)
- Time = 5 min

57

Cleaning in HNO_3 (99%)
(#clean138)

NL-CLR-WB14
Purpose: removal of organic traces.

- Beaker 2: HNO_3 (99%)
- Time = 5 min

58

Quick Dump Rinse (QDR)
(#rinse119)

NL-CLR-Wetbenches
Purpose: removal of traces of cleaning agents.

Recipe 1 Quick dump rinsing (QDR)
Recipe 2 Cascade rinsing for fragile wafers

Rinse until message ´End of rinsing process´ is shown on the touchscreen of the QDR, else repeat the rinsing process.

59

Cleaning in HNO_3 (69%, 95 °C)
(#clean 118)

NL-CR-WB14
Purpose: removal of metallic traces.

- Beaker 3a or beaker 3b: HNO_3 (69%)
- Temp 95°C
- Time = 10min

60

Quick Dump Rinse (QDR)
(#rinse119)

NL-CLR-Wetbenches
Purpose: removal of traces of cleaning agents.

Recipe 1 Quick dump rinsing (QDR)

Recipe 2 Cascade rinsing for fragile wafers

Rinse until message ´End of rinsing process´ is shown on the touchscreen of the QDR, else repeat the rinsing process.

61

Substrate drying (WB14)
(#dry159)

NL-CLR-WB14

Single substrate drying:
1. Use the single-wafer spinner
   Settings: 2500 rpm, 60 sec (including 45 sec nitrogen purge)
2. Use the nitrogen gun (fragile wafers or small samples)

Batch drying of substrates:
The Semitool uses the following standard procedure:
- Rinse: 30 sec (600 rpm)
- Q-rinse: 10.0 MΩ (600 rpm)
- Purge: 10 sec (600 rpm)
- Drying: 280 sec (1600 rpm)

Note: it is obligatory to apply a single rinsing step in the QDR before using the Semitool!

62

Etching in HF (1%)
(#etch127)

NL-CLR-WB15
Purpose: to remove the native SiO2 from silicon wafers.

Beaker: HF 1%
Time = 1 min

Note: Continue using the quartz wafer carrier of WB14, since this step is part of the pre-furnace processing. Return the quartz wafer carrier back to WB14.

63

Quick Dump Rinse (QDR)
(#rinse119)

NL-CLR-Wetbenches
Purpose: removal of traces of cleaning agents.

Recipe 1 Quick dump rinsing (QDR)
Recipe 2 Cascade rinsing for fragile wafers

Rinse until message ´End of rinsing process´ is shown on the touchscreen of the QDR, else repeat the rinsing process.

64

Substrate drying (WB15)
(#dry160)

NL-CLR-WB15

Single substrate drying:
1. Use the single-wafer spinner
   Settings: 2500 rpm, 60 sec (including 45 sec nitrogen purge)

	2. Use the nitrogen gun (fragile wafers or small samples) **Batch drying of substrates:** The Semitool uses the following standard procedure: • Rinse: 30 sec (600 rpm) • Q-rinse: 10.0 MΩ (600 rpm) • Purge: 10 sec (600 rpm) • Drying: 280 sec (1600 rpm) <u>Note</u>: it is obligatory to apply a single rinsing step in the QDR before using the Semitool!	
65 **Sputtering of Al** (#film122)	NL-CLR-Oxford PL400 • Program: 3000nm Al pos 1 • Pressure: 10mTorr Depositionrate (100mm wafer) = 820nm/min	
66		Mask 3: Aluminium patterning
67 **Dehydration bake** (#lith102)	NL-CLR-WB21/22 dehydration bake at hotplate • temp. 120°C • time: 5min	Continue immediately with priming.
68		(lith1100) Lithography AZ4999 by spray coating for perfect step coverage
69		Alignment & exposure of AZ4999 (EV620)
70		Development AZ4999 Resist
71 **Quick Dump Rinse (QDR)** (#rinse119)	NL-CLR-Wetbenches Purpose: removal of traces of cleaning agents. Recipe 1 Quick dump rinsing (QDR) Recipe 2 Cascade rinsing for fragile wafers Rinse until message ´End of rinsing process´ is shown on the touchscreen of the QDR, else repeat the rinsing process.	
72 **Substrate drying** (#dry120)	NL-CLR-WB **Single substrate drying:** 1. Use the single-wafer spinner Settings: 2500 rpm, 60 sec (including 45 sec nitrogen purge) 2. Use the nitrogen gun (fragile wafers or small samples)	
73		Postbake AZ4999 Resist 120 degrees 10 minutes
74 **Inspection by**	NL-CLR- Nikon Microscope	

optical microscope
(#metro101)

- dedicated microscope for lithography inspection

75

Etching of aluminium
(#etch135)

NL-CLR-WB13
Use dedicated beaker with aluminium etchant (standard)
- temp.: 55°C

Etchrates = 1µm/min

76

Quick Dump Rinse (QDR)
(#rinse119)

NL-CLR-Wetbenches
Purpose: removal of traces of cleaning agents.

Recipe 1 Quick dump rinsing (QDR)
Recipe 2 Cascade rinsing for fragile wafers

Rinse until message ´End of rinsing process´ is shown on the touchscreen of the QDR, else repeat the rinsing process.

77

Freckle etch (Al-Si 1%)
(#etch215)

NL-CLR-WB13-UCL
Use Freckle etchant
Chemicals: phosphoric acid, acetic acid, nitric acid and tetrafluoroboric acid
Time: 7-8 min
Temperature: 21-25 ^{o}C

Purpose: remove residuel nodules (´freckles´) left after etching
of aluminium-silicon films.

78

Quick Dump Rinse (QDR)
(#rinse119)

NL-CLR-Wetbenches
Purpose: removal of traces of cleaning agents.

Recipe 1 Quick dump rinsing (QDR)
Recipe 2 Cascade rinsing for fragile wafers

Rinse until message ´End of rinsing process´ is shown on the touchscreen of the QDR, else repeat the rinsing process.

79

Substrate drying
(#dry120)

NL-CLR-WB

Single substrate drying:
1. Use the single-wafer spinner
   Settings: 2500 rpm, 60 sec (including 45 sec nitrogen purge)
2. Use the nitrogen gun (fragile wafers or small samples)

80

Stripping polymers

NL-CLR-WB13-UCL

and resists in HNO_3 (99%) (#strip207)	Purpose: stripping of polymers and resists. • Beaker 0: HNO_3 (99%) • Time: continue until complete removal of resist	
81 **Quick Dump Rinse (QDR)** (#rinse119)	NL-CLR-Wetbenches Purpose: removal of traces of cleaning agents. Recipe 1 Quick dump rinsing (QDR) Recipe 2 Cascade rinsing for fragile wafers Rinse until message ´End of rinsing process´ is shown on the touchscreen of the QDR, else repeat the rinsing process.	
82 **Substrate drying (WB13)** (#dry158)	NL-CLR-WB13 **Single substrate drying:** 1. Use the single-wafer spinner Settings: 2500 rpm, 60 sec (including 45 sec nitrogen purge) 2. Use the nitrogen gun (fragile wafers or small samples) **Batch drying of substrates:** The Semitool uses the following standard procedure: • Rinse: 30 sec (600 rpm) • Q-rinse: 10.0 MΩ (600 rpm) • Purge: 10 sec (600 rpm) • Drying: 280 sec (1600 rpm) Note: it is obligatory to apply a single rinsing step in the QDR before using the Semitool!	
83 **Sintering of Si-Al interface** (#therm137)	NL-CLR-Furnace B4 Improving electrical contact Al-Si • Standby temperature: xxx • Program: xxx • Temperature: 400°C • Gas: N_2 • Flow: xx l/min • Ramp: xxx °C/min • Cooldown: xxx°C/min	Annealing: 30 min, 450 degrees Celcius

Bibliography

[1] J. Nakamura, *Image Sensors and Signal Processing for Digital Still Cameras*, CRC Press / Taylor & Francis Group, 2006

[2] M. Faraday, *Thoughts on Ray Vibrations*, Philosophical Magazine, S.3, Vol XXVIII, N188, 1846.

[3] G. Lippmann, *Épreuves réversibles. Photographies intégrales.*, Comptes Rendus, Académie des Sciences, 146:446-451, 1908

[4] Raytrix GmbH, *Raytrix Lightfield Camera*, available on http://www.raytrix.de/tl_files/downloads/Raytrix_Slides.pdf

[5] Lytro Incorporated, *Lytro*, available on https://www.lytro.com/

[6] D.J. Hegyi, *System for determining the direction of incident optical radiation*, US Patent 5264691 / European Patent 0596982, 1991

[7] H. Wang, T. Luo, H. Song, J. Blain Christen, *On-chip sensor for light direction detection*, Optics Letters, 38:4554-4557, 2013

[8] A. Wang, P. Gill, A. Molnar, *Light field image sensors based on the Talbot effect*, Applied Optics, 48:5897-5905, 2009

[9] O. Tabata, R. Asahi, H. Funabashi, K. Shimaoka, S. Sugiyama, *Anisotropic etching of silicon in TMAH solutions*, Sensors and Actuators A34, 51:57, 1992

[10] D.J. Griffiths, *Introduction to Electrodynamics*, 3rd edition, Pearson Education Ltd., 2008

[11] Landolt-Börnstein, *Numerical Data and Functional Relationships in Science and Technology*, New Series, II/16, *Diamagnetic Susceptibility*, Springer-Verlag, Heidelberg, 1986

[12] M.A. Green, *Self-consistent optical parameters of intrinsic silicon at 300K including temperature coefficients*, Solar Energy Materials & Solar Cells 92, pp. 1305-1310, 2008

[13] M.J. Cooke, *Semiconductor Devices*, Prentice Hall International (UK) Ltd., 1990

[14] O. Christensen, *Quantum efficiency of the internal photoelectric effect in silicon and germanium*, J. Appl. Phys. 47:689-695, 1976

[15] N.D. Arora, J.R. Hauser, D.J. Roulston, *Electron and Hole Mobilities in Silicon as a Function of Concentration and Temperature*, IEEE Transactions on Electron Devices, 29:292, 1982

[16] M. S. Tyagi, R. Van Overstraeten, *Minority carrier recombination in heavily-doped silicon*, Solid State Electronics 26, 6:577-598, 1983

[17] A. Cuevas, R.A. Sinton, *Measuring and interpreting the lifetime of silicon wafers*, Solar Energy, 76:255-262, 2004

[18] J. Vedde, *Float-zone silicon for high volume production of solar cells*, presented at the 3rd World Conference on Photovoltaic Energy Conversion, Osaka, Japan May 11-18, 2003

[19] A. Cuevas, R.A. Sinton, *Prediction of the Open-circuit Voltage of Solar Cells from the Steady-state Photoconductance*, Prog. Photovoltaics, 5:79-90, 1997

[20] A.B. Sproul, *Dimensionless solution of the equation describing the effect of surface recombination on carrier decay in semiconductors*, J. Applied Physics, 76:2851-2854, 1994

[21] M. Stone P. Goldbart, *Mathematics for Physics I*, Pimander-Casaubon, 2008

[22] D. Mitronivić, J. Kečkić, *The Cauchy method of residues: Theory and applications*, D. Reidel Publishing Company, 1984

[23] R.T. Tung, *Barrier Height Systematics*, http://academic.brooklyn.cuny.edu/physics/tung/Schottky/systematics.htm

[24] B. Van Zeghbroeck, *Principles of Semiconductor Devices*, http://ecee.colorado.edu/∼bart/book/

[25] A. Javey, *Section 8: Metallization*, lecture sheets EE143

[26] D. Voltmer, *Fundamentals of Electromagnetics 1: Internal Behavior of Lumped Elements*, Morgan & Claypool 2007

[27] H. Topsoe, *Geometric factors in four point resistivity measurement*, available from http://four-point-probes.com/haldor.html, 1966

[28] A. Kalavagunta, R.A. Weller, *Accurate Geometry Factor Estimation for the Four Point Probe Method using COMSOL Multiphysics*, Proceedings of the COMSOL Multiphysics User's Conference, Boston, 2005

[29] Keithley Instruments Inc., *Low Level Measurements*, Keithley Instruments Inc., 5th edition, 1998

[30] B.E. Bayer, *Color imaging array*, US patent 3971065

[31] Digital Photography Review, *Kodak DCS620x Review*, http://www.dpreview.com/reviews/kodakdcs620x

[32] Foveon, Inc., *Direct image sensors*, http://www.foveon.com/article.php?a=67

[33] J.S. Steinhart, S.R. Hart, *Calibration curves for thermistors*, Deep-Sea Research, 15:497-503, 1968

[34] E. Hecht, *Optics*, 4th edition, Addison Wesley, 2002